An Active Magnetic Bearing Test Rig for High Speed Rotating Machinery: Design and Application

---

A

Thesis

Presented to

the faculty of the School of Engineering and Applied Science

University of Virginia

---

in partial fulfillment

of the requirements for the degree

Master of Science

by

William Arcand

May 2022

APPROVAL SHEET

This

Thesis

is submitted in partial fulfillment of the requirements
for the degree of

Master of Science

Author: William Arcand

This Thesis has been read and approved by the examing committee:

Advisor: Roger Fittro

Advisor:

Committee Member: Robert Rockwell

Committee Member: Gang Tao

Committee Member:

Committee Member:

Committee Member:

Committee Member:

Accepted for the School of Engineering and Applied Science:

Jennifer L. West, School of Engineering and Applied Science

May 2022

Abstract

Modern industrial high-speed machinery often operates above multiple shaft critical speeds and requires in-depth rotordynamic modeling and analysis. Active Magnetic Bearings (AMBs) have proven to be a compelling alternative to traditional bearings for many such high-speed, high-performance applications. AMBs apply attractive magnetic forces to support and center a rotor shaft within the machine clearance. They can maintain contactless operation and handle the varying dynamic unbalance forces that are generated throughout the machine's operating range. However, the practical implementation of AMBs is more complex than for traditional bearings because AMBs are inherently open-loop unstable and require stabilizing feedback.

This research presents the design and practical construction of the *Honeywell Magnetic Bearing Test Rig* (HMBTR), a scaled version of an industrial high-speed vertical shaft spin test rig that is supported by magnetic bearings. State-space models for the rotor and supporting electromagnetic hardware are developed and experimentally validated. Two control designs are implemented: independent-axis SISO PID control and Modal PID control. Ultimately, the main goal of this project is to predict and successfully demonstrate the capability of AMBs for use in high-speed machinery applications. The HMBTR itself is delivered as a general platform for future learning and experimentation with AMBs.

Acknowledgments

To start, I would like to thank my advisors, Roger Fittro and Bob Rockwell, for giving me the opportunity to work on this project and for all the weeks of guidance and technical insight. Thank you to the Department of Mechanical and Aerospace Engineering at UVA and thank you to ROMAC for the resources provided to make this project a reality. I am also very grateful for the project funding provided by Honeywell Federal Manufacturing and Technologies, LLC as a ROMAC partner.

And a special thank you to my parents for always cheering me on.

Contents

1 Introduction **1**

1.1 Literature Review 2

1.2 Scope of Thesis 4

2 System Design and Analysis **5**

2.1 Rotor Design 5

2.2 Motor Drive System 8

2.3 Magnetic Bearing Control System 9

2.3.1 Amplifiers 11

2.3.2 Sensors 11

2.3.3 Digital Controller 12

2.4 Structure Design 12

3 System Modeling and Validation **14**

3.1 Rotor Dynamics Model 14

3.1.1 Finite Element Model 16

3.1.2 State Space Model 18

3.2 Rotor Model Validation 19

3.3 Amplifier-Actuator Model 27

3.3.1 Amplifier Dynamics 30

3.4 Sensor Model 32

3.5 Digital Controller 33

3.6 Closed Loop System Model 34

3.7 Closed Loop System Model Validation 35

4 HMBTR - Control Design **40**

4.1 Performance Goal 40

4.2 Thrust Bearing PID Control Design 42

4.3 Radial Bearing PID Control Design 43

4.4 Modal PID Control Design 45

4.4.1 Closed Loop System Stabilization 49

4.4.2 Rotor Asymmetry Kx Compensation 51

4.5 Theoretical Comparisons 51

4.5.1 Thrust Bearing Control Designs 51

4.5.2 Radial Bearing Control Designs 52

4.6 Experimental Results 56

4.6.1 Thrust Bearing Experimental Compliance 58

4.6.2 Radial Bearing Experimental Compliance 60

5 Conclusions and Future Work **63**

5.1 Conclusions 63

5.2 Future Work 64

A Test Rig Physical Design Parameters **68**

B Rotor Model Matrices **72**

C Rotor Identification Plots **74**

C.1 Bare Rotor 74

C.2 Full Rotor - Soft Tip Impact Hammer 78

D Simulink Models **82**

E Hardware Datasheets 86

F Mechanical Assembly Details 93

List of Figures

1 Magnetic Suspension Example, from Larsonneur [11] 1

2 Industrial Overhung Spin Test Rig, from Honeywell FM&T . . 2

3 Rotor Solid Model, from Robert Rockwell 7

4 Honeywell High-Speed Magnetic Bearing Test Rig 13

5 Rigid Rotor Free Body Diagram, from [6] 14

6 Finite Element Rotor Model 17

7 Finite Element 17

8 Rotor Free-Free Mode Shapes 20

9 Experimental Impact Testing Input-Output Locations 21

10 Input A to Output B: Experimental Data (Red) vs. Model (Blue) 22

11 Bare Rotor: DE AMB to Test Article FRF 23

12 Input A to Output C: Experimental Data (Red) vs. Model (Blue) 24

13 Input A to Output B: Experimental Data (Red) vs. Model (Blue) 24

14 Input B to Output A: Experimental Data (Red) vs. Model (Blue) 25

15 Input B to Output C: Experimental Data (Red) vs. Model (Blue) 25

16 Input C to Output A: Experimental Data (Red) vs. Model (Blue) 26

17 Input C to Output B: Experimental Data (Red) vs. Model (Blue) 26
18 Linearized Actuator, from [15] 27
19 Amplifier-Actuator System Block Diagram 30
20 Radial Amplifier Frequency Response: Experimental Data (Red) vs. Model (Blue) 31
21 Thrust Amplifier Frequency Response: Experimental Data (Red) vs. Model (Blue) 32
22 Digital Controller: Experimental Data (Red) vs. Model (Blue) 34
23 Radial System Block Diagram 34
24 Axial System Block Diagram 35
25 Thrust AMB Input to Thrust Sensor Output: Experimental Data (Red) vs. Model (Blue) 36
26 DE-AMB Input to DE-Sensor Output: Experimental Data (Red) vs. Model (Blue) 37
27 DE-AMB Input to NDE-Sensor Output: Experimental Data (Red) vs. Model (Blue) 37
28 NDE-AMB Input to DE-Sensor Output: Experimental Data (Red) vs. Model (Blue) 38
29 NDE-AMB Input to NDE-Sensor Output: Experimental Data (Red) vs. Model (Blue) 38
30 Test Rig Structure Frequency Response 39
31 Simplified Closed Loop System Block Diagram 40
32 Thrust Axis PID Controller Transfer Functions 43
33 Radial Axis PID Controller Transfer Function 45

34 Modal Transformation System Diagram 46
35 Frequency Response: $G_{PM}(1,1)$ (Blue) vs. $G_P(1,1)$ (Red) . . 47
36 Frequency Response: $G_{PM}(2,2)$ (Blue) vs. $G_P(2,2)$ (Red) . . 47
37 Frequency Response: $G_{PM}(2,1)$ (Blue) vs. $G_P(2,1)$ (Red) . . 48
38 Frequency Response: $G_{PM}(1,2)$ (Blue) vs. $G_P(1,2)$ (Red) . . 48
39 Nyquist Plot: Translational DOF 50
40 Nyquist Plot: Rotational DOF 50
41 Modal Controller Frequency Response 52
42 Thrust Controller Compliance: Low Bandwidth (Blue), High Bandwidth (Red) 53
43 Thrust Controller Sensitivity: Low Bandwidth (Blue), High Bandwidth (Red) 53
44 System Compliance Comparison 54
45 Unbalance Displacement: PID Controller 55
46 Unbalance Displacement: Modal Controller 55
47 Closed Loop Sensitivity, PID Control 56
48 Closed Loop Sensitivity, Modal Control 57
49 Load Capacity: PID Controller 57
50 Load Capacity: Modal Controller 58
51 Thrust Axis Compliance Low Bandwidth PID: Experimental Data (Red) vs. Model (Blue) 59
52 Thrust Axis Compliance High Bandwidth PID: Experimental Data (Red) vs. Model (Blue) 59
53 Radial Axis SISO PID Compliance DE: Experimental Data (Red) vs. Model (Blue) 60

54 Radial Axis SISO PID Compliance NDE: Experimental Data (Red) vs. Model (Blue) 61
55 Radial Axis Modal PID Compliance DE: (Red) vs. Model (Blue) 61
56 Radial Axis Modal PID Compliance NDE: (Red) vs. Model (Blue) 62
57 Rotor Mechanical Design, 2D View 68
58 Thrust Actuator, from Baun [3] 69
59 Radial Actuator Cross-Section, from Baun [3] 70
60 Radial Actuator Side View, from Baun [3] 71
61 Input A to Output C: Experimental Data (Red) vs. Model (Blue) 74
62 Input A to Output B: Experimental Data (Red) vs. Model (Blue) 75
63 Input B to Output A: Experimental Data (Red) vs. Model (Blue) 75
64 Input B to Output C: Experimental Data (Red) vs. Model (Blue) 76
65 Input C to Output A: Experimental Data (Red) vs. Model (Blue) 76
66 Input C to Output B: Experimental Data (Red) vs. Model (Blue) 77
67 Input A to Output C: Experimental Data (Red) vs. Model (Blue) 78
68 Input A to Output B: Experimental Data (Red) vs. Model (Blue) 79

69 Input B to Output A: Experimental Data (Red) vs. Model (Blue) . . . 79
70 Input B to Output C: Experimental Data (Red) vs. Model (Blue) . . . 80
71 Input C to Output A: Experimental Data (Red) vs. Model (Blue) . . . 80
72 Input C to Output B: Experimental Data (Red) vs. Model (Blue) . . . 81
73 Top-Level Model . . . 82
74 Radial Subsystem . . . 83
75 Controller Subsystem . . . 84
76 Amplifier Subsystem . . . 85
77 Motor: MOOG BN34HS, Derived Parameters . . . 86
78 Motor: Moog BN34HS, Physical Parameters . . . 87
79 Amplifier: Copley Controls JSP-090-10 . . . 88
80 Controller: dSpace MicroLabBox . . . 89
81 Motor Controller: MOOG Silencer Series . . . 90
82 Displacement Sensor: Lion Precision U5 . . . 91
83 Coupling, R+W BKL-10 . . . 92
84 NDE Backup Bearing Assembly . . . 93
85 Assembly Drawing, Rotor . . . 94
86 Assembly Drawing, Motor . . . 95
87 Radial AMB / Exciter Assembly . . . 95
88 Sensor Assembly . . . 96
89 Thrust AMB / DE Backup Bearing Assembly . . . 96

90 DE Backup Bearings: Double Row Deep Groove Ball Bearings (2x 6001) 97
91 NDE Backup Bearings: Double Row Angular Contact Ball Bearings, Face-to-Face Arrangement, (2 x S 61903 C TA) . . . 98

List of Tables

1 Rotor Mode Speeds, from RotorSol 6

2 Physical Parameters, Shaft Attachments 7

3 Motor Drive System Specifications 9

4 Radial Actuator Design Parameters 10

5 Thrust Actuator Design Parameters 10

6 Rotor Eigenvalues 20

7 AMB Design Changes 29

8 k_i and k_x, Thrust and Radial Actuators 30

9 Rotor Model IO 35

10 Initial Thrust Controller Parameters 43

11 Higher-Bandwidth Thrust Controller Parameters 43

12 Radial Controller Parameters 44

13 Rotor Section Length and Diameter Parameters 68

14 Windage Calculations 69

15 Thrust Actuator Dimensions 70

16 Radial Actuator Dimensions 71

Nomenclature

μ_0	Permeability of Free Space	$1.256 \times 10^{-6}\,\mathrm{N\,A^{-2}}$
ρ	Density of Air at 25 ℃	$1.562 \times 10^{-5}\,\mathrm{m^2\,s^{-1}}$
υ	Kinematic Viscosity of Air at 25 ℃	$1.1839\,\mathrm{kg\,m^{-3}}$
μ_r	Relative Permeability	
Ω	Shaft Rotating Speed	
A_g	Actuator Pole Face Area	
C_d	Windage Calculation Shape Coefficient	
F	Actuator Force	
g	Air Gap	
g_0	Nominal Air Gap	
G_P	Open Loop Plant Model	
i	Actuator Current	
i_b	Bias Current	
i_p	Perturbation Current	
k_a	Amplifier Gain	
K_i	Actuator Open Loop Gain TFM	

k_i Actuator Current Gain

K_s Sensor Gain TFM

K_x Actuator Open Loop Stiffness TFM

k_x Actuator Open Loop Stiffness

L Rotor Axial Length

l Magnetic Path Length

N Number of Coil Windings

r_0 Outer Shaft Radius

Re Real Part of a Complex Number

T_s Sampling Rate

$T_{amp}(s)$ Amplifier Transfer Function

Acronyms

AMB Active Magnetic Bearing

$BLDC$ Brushless DC Electric Motor

DE Drive End

DOF Degree of Freedom

DSA Dynamic Signal Analyzer

FFT Fast Fourier Transform

FRF Frequency Response Function

$HMBTR$ Honeywell Magnetic Bearing Test Rig

NDE Non Drive End

PID Proportional-Integral-Derivative

$ROMAC$ Rotating Machinery and Controls Laboratory

TFM Transfer Function Matrix

1 Introduction

Higher operating speeds and power densities are continually sought after in the rotating machinery industry. As operating speed is increased, additional vibrational resonances of the shaft are excited and will cause a variety of performance and stability issues. Active Magnetic Bearings (AMBs) enable efficient, high-speed, non contact rotor operation and are a compelling solution to this problem. However, AMB's intrinsically introduce additional system complexity when compared to standard mechanical bearings because they are inherently unstable and require implementation of a feedback controller.

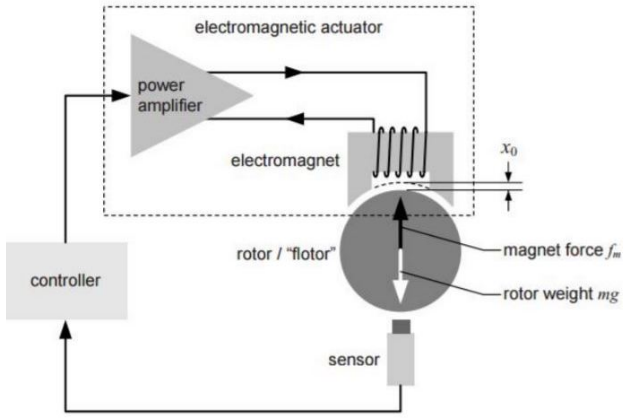

Figure 1: Magnetic Suspension Example, from Larsonneur [11]

In its most simple configuration, a magnetic bearing system relies on a position sensor, power amplifier, controller, and an electromagnet. As shown in Figure 1, a feedback loop is formed where the controller produces a command voltage based on the position of the rotor. In turn, the power amplifier supplies a controlled current to the electromagnet, generating a force that levitates the rotor within the air gap.

The choice of algorithm that is implemented on the controller will determine the full system's stability and performance. PID control is often utilized, but can struggle to deliver robust performance on systems with complex dynamics [1]. The overhung disc systems utilized in modern high-speed machinery often operate above multiple shaft critical speeds that can induce instability. A model-based control design that takes these dynamics into account is required for full-speed operation.

This thesis presents the development of the Honeywell High-Speed Magnetic Bearing Test Rig (HMBTR) - a reduced scale vertical shaft spin test rig based on the industrial rig shown in Figure 2. The HMBTR enables exploration of AMB control algorithms that solve some of the common challenges seen in modern high-speed machinery.

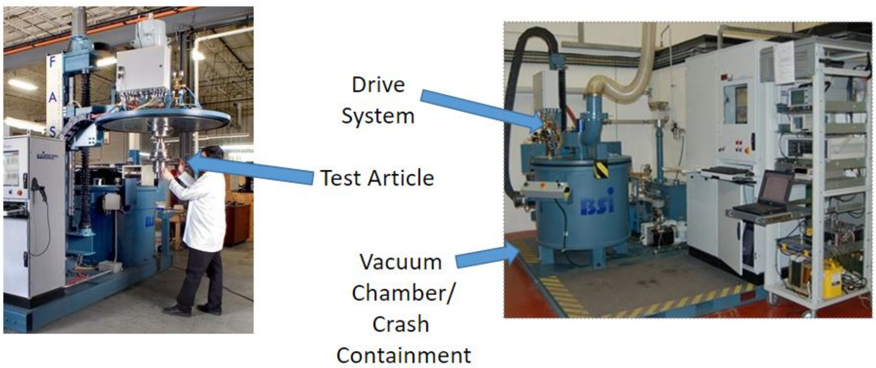

Figure 2: Industrial Overhung Spin Test Rig, from Honeywell FM&T

1.1 Literature Review

In-depth rotordynamic modeling and analysis is required to enable development of a high-performance control algorithm for the HMBTR. Rotordynamic theory began with the introduction of the Jeffcott rotor in 1919 that introduced a simple flexible rotor model and gave a framework for understanding basic rotordynamic principles [9]. Afterwards, the development of computers allowed for more complexity in analysis and a number of rotordynamic modeling techniques were established, most notably the finite element method (FEM). As early as 1970, Ruhl applied the FEM in a basic capacity to a rotor system [17]. With higher system speeds and the introduction of gyroscopic effects, higher order models became necessary to capture the full system dynamics containing multiple flexible modes. D.F. Li et al. implemented the transfer matrix method for construction of a flexible rotor-bearing system model [14].

Furthermore, the Rotating Machinery and Controls Laboratory (ROMAC) at the University of Virginia has contributed a base of prior work that is specifically applicable to this project. The HMBTR is a high-speed overhung disk system that exhibits the gyroscopic behavior associated with a large disc and thin shaft. Benson and Gunter developed an early model for a high-speed overhung rotor system that accounts for gyroscopic effects on system dynamics [4]. Wilson showed that the stiffness and damping of the distal bearing has the greatest impact on the overall rotor damping characteristic in these types of systems [20].

Control is required in both the axial and radial directions. Progress in control of axial shaft vibrations through use of magnetic bearings was documented by Lewis et al. in 1987 [18]. For the radial directions, Kelm et al. details the development of a magnetic bearing control system for a flexible rotor [10]. Dimond, et al. achieved higher performance control of a similar system using a Modal Tilt/Translate control method [6].

1.2 Scope of Thesis

This work is focused on the development of the HMBTR. Chapter 2 introduces the requirements on the rig and the design choices that were made to satisfy them. Chapter 3 covers the development of a mathematical model of the HMBTR and its validation on the hardware. Chapter 4 details the development of both a standard PID control design and a 'modal' design for the HMBTR's radial axis. A high-bandwidth and a low-bandwidth PID controller are designed for the thrust axis as well. Theoretical comparisons of all control designs are made and experimental results obtained for each controller are compared with the corresponding theoretical predictions. Finally, Chapter 5 gives some overall conclusions and makes suggestions for future work.

2 System Design and Analysis

System design choices were made based on the set of system requirements provided by Honeywell. Most importantly, these requirements specify that the rotor shall operate above the first flexural critical speed. Furthermore, the shaft shall be in the vertical position and will carry an operating load from 5 lbf to 10 lbf. The rotor system shall be an overhung rotor design that includes a large disc at the distal end of the shaft. There shall be an additional AMB located at the shaft midspan which can be used to apply arbitrary external loads to the system. Finally, the system is to have a motor, bearing controls, and the instrumentation for basic rotor operation characterization.

2.1 Rotor Design

The requirement with the largest impact on system design was that the rig must operate through the first flexural critical speed. To ensure this requirement was met, an iterative rotor design process was followed where the dynamic characteristics of a potential rotor design were estimated using the ROMAC RotorLab software. Major design parameters such as rotor length and diameter were varied and the resulting modes compared until a satisfactory design emerged.

The system critical speeds for the final rotor design are included in Table 1. The detailed design parameters necessary for this critical speed calculation are included in Appendix-A. These were computed with a 'low' AMB stiffness value of 1000 lb/in as well as with a 'high' stiffness value of 5000 lb/in. A nominal stiffness for the motor-rotor coupling of 1827 lb/in was factored in as well. The relevant manufacturer specifications for the coupling are included in Appendix-E.

Mode Type	Low AMB Stiffness	High AMB Stiffness
Test Article	1730 rpm	2920 rpm
Coupling End	5550 rpm	8650 rpm
Rotor Midspan	10 760 rpm	12 320 rpm

Table 1: Rotor Mode Speeds, from RotorSol

Three distinct modes are produced from 1730 rpm to 12 470 rpm for either AMB stiffness. The first two modes are essentially extensions of the rotor's rigid body modes. The third mode is a vibration about the rotor's mid-span and corresponds to the first flexural mode. This places the first flexural critical speed well within the motor's capability of 15 000 rpm (See Section 2.3).

This conceptual rotor design satisfies rig requirements and was refined and developed into a detailed system model for manufacture. The resulting system model is shown in Figure 3 with the important sub-components labeled.

When fully assembled, the rotor is 19.125 in long and weighs 9.3 lbm. The shaft is nominally 0.5 in in diameter. Three laminated rotor stacks are mounted by interference fit onto the drive-end (DE), non-drive-end (NDE), and middle of the shaft to match radial support AMBs and an exciter AMB. The test article is attached at the non-drive end of the shaft. The thrust disk is attached at the drive end of the shaft and will allow for control of axial loads. Ball bearings are mounted at both the DE and NDE ends of the shaft to serve as backup bearings. The rotor is connected to the drive shaft with a flexible coupling.

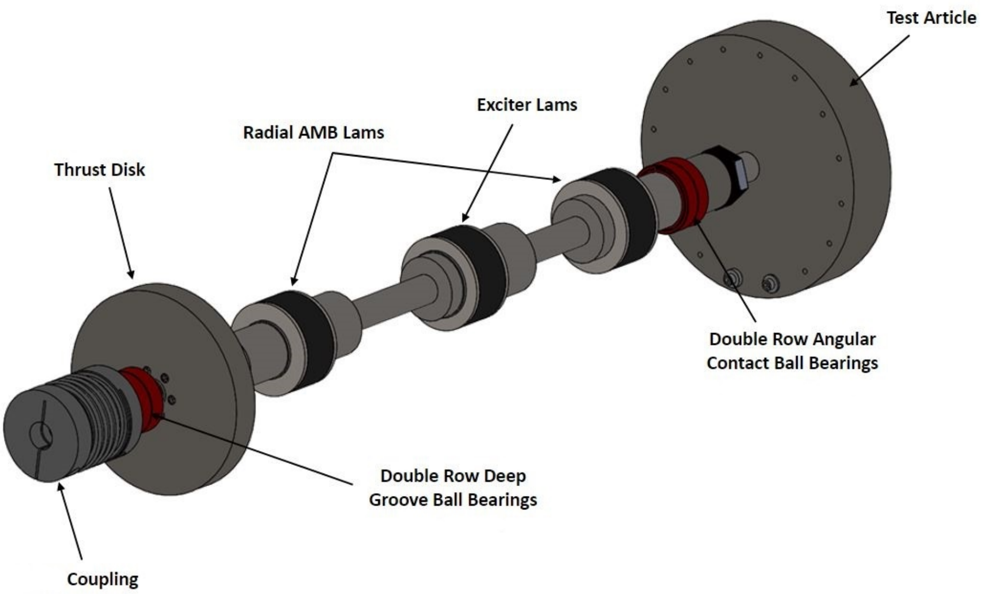

Figure 3: Rotor Solid Model, from Robert Rockwell

Item	Length in	OD in	Mass lbf
BKL-10 Coupling	1.575	0.13	0.512
Thrust Disk	3.5	1.33	0.5
Test Article	4.5	1.0	4.45

Table 2: Physical Parameters, Shaft Attachments

2.2 Motor Drive System

The Motor Drive System consists of a DC motor with an associated motor controller and dedicated power supply. The motor is connected directly to the shaft with a flexible coupling. Both speed and torque requirements inform the choice of motor. The motor must reach a maximum speed that is high enough to excite three rotor bending modes (15 000 rpm). In tandem, motor torque needs to exceed the windage loss at that speed and with the attached load.

Windage loss is calculated separately for each rotor component. The Thrust Disk, Test Article, and Coupling are modeled as disks. The Bearings and Shaft are modeled as annuli. Windage losses are based on a drag coefficient (C_d), shaft rotating speed (Ω), outer shaft radius (r_0), and axial length (L):

$$WindageLoss(Annulus) = \pi C_d \rho {r_0}^4 \Omega^3 L \tag{1}$$

$$WindageLoss(Disk) = \pi C_d \rho {r_0}^5 \Omega^3 \tag{2}$$

$$Re = \frac{r_0 g_0 \Omega}{\upsilon} \tag{3}$$

$$\frac{1}{\sqrt{C_d}} = 2.04 + 1.768 \ln(Re\sqrt{(C_d)}) \tag{4}$$

Windage calculations by component are recorded in Appendix-A. In total, windage loss is 4.37 in-oz at an operating speed of 15 000 rpm. The MOOG BN-34HS Brushless DC electric motor (BLDC) is specified to have a Rated

Torque of 34.0 in-oz and is more than up to the task. This motor is paired with the MOOG BDO-Q2-50-40 Silencer Series Motor Drive. The motor drive allows speed control by voltage command signal. This subsystem is powered by a PowerVolt 24 V DC Power Supply. Further specifications are recorded in Table 3.

No Load Speed	16 707 rpm
Rated Speed	14 011 rpm
Maximum Continuous Stall Torque	48.0 in-oz
Rated Torque	34.0 in-oz
Operating Voltage	24 V

Table 3: Motor Drive System Specifications

2.3 Magnetic Bearing Control System

A magnetic bearing system is used to support the rotor in both its radial and axial (thrust) directions. This system includes position sensors, amplifiers, actuators, and a controller that work together to perform feedback control for the AMB system. Datasheets for each hardware item are in Appendix-E.

Three radial and two thrust actuators were acquired from a test rig that was previously built in the ROMAC lab by Daniel Baun [3]. Baun recorded the design and experimental characterization of these actuators in his PhD dissertation. Design parameters of the radial actuators are recorded in Table 4 and for the thrust actuators in Table 5. The radial actuators were designed to have an RMS load capacity of 8 lbf and the thrust actuator to have a maximum thrust load of 42 lbf. This puts both actuators well within this project's requirement that it must carry an operating load from 5 lbf to 10 lbf.

Bias Current, i_b	1.2 A
Peak Current, i_p	3.75 A
Coil Winding, N	218
Wire Gage	24 AWG
Laminate Thickness	0.014 in
Saturation Flux Density, B_s	20 600 G
Relative Permeability, μ_r	1000
Coercive Force, H_c	0.7 Oe
RMS Load Capacity	8 lbf
Peak Load Capacity	20 lbf

Table 4: Radial Actuator Design Parameters

Bias Current, i_b	1.75 A
Peak Current, i_p	2.55 A
Coil Winding, N	300
Wire Gage	22 AWG
Relative Permeability, μ_r	139
Coercive Force, H_c	4.94 Oe
Peak Load Capacity	42 lbf

Table 5: Thrust Actuator Design Parameters

2.3.1 Amplifiers

The amplifiers used for this test rig are Copley Controls JSP-090-10. They deliver a desired current to the AMB coils based on a control voltage input. Power is supplied by the PST-075-10 DC Power Supply that is also made by Copley Controls. In total, there are 14 DC servo amplifiers that are each rated for 10 A of peak power or 5 A of continuous power at 90 V. This exceeds the current requirements of both the radial and thrust actuators.

2.3.2 Sensors

System requirements dictate that the sensors must be non-contacting, high bandwidth, and linear. Satisfying this, Lion Precision U5B eddy current sensors are used for rotor position sensing. Sensor pairs are located near the DE and NDE actuator locations. Another pair is located near the exciter AMB that is used for monitoring purposes only. A final sensor pair is located between the DE AMB and the Exciter AMB that provides an alternate sensor location for control of the DE AMB. This sensor pair is only used for monitoring purposes throughout this work, but its location does enable future experimentation with sensor-AMB non-collocation issues. A final sensor measures the axial movement of the test article. The sensors arrived pre-calibrated by the manufacturer. The Lion Precision ECL 150 electronics system manages the set of eddy current sensors and delivers feedback sensor signals to the digital controller.

2.3.3 Digital Controller

Control algorithms are implemented on the dSpace MicroLabBox. The MicroLabBox runs on a 2 GHz Dual-Core Real-Time processor. It has built-in analog I/O channels with A/D and D/A converters and an Ethernet interface. Conveniently, it is programmed using a Matlab-Simulink interface which allows for quick control design development with code generation and download to processor.

2.4 Structure Design

To finish, a square tower support structure was designed to house the assembled system. The fully assembled rig is pictured in Figure 4. The rig has a height of 25.55 in and a base of 6 in by 6 in.

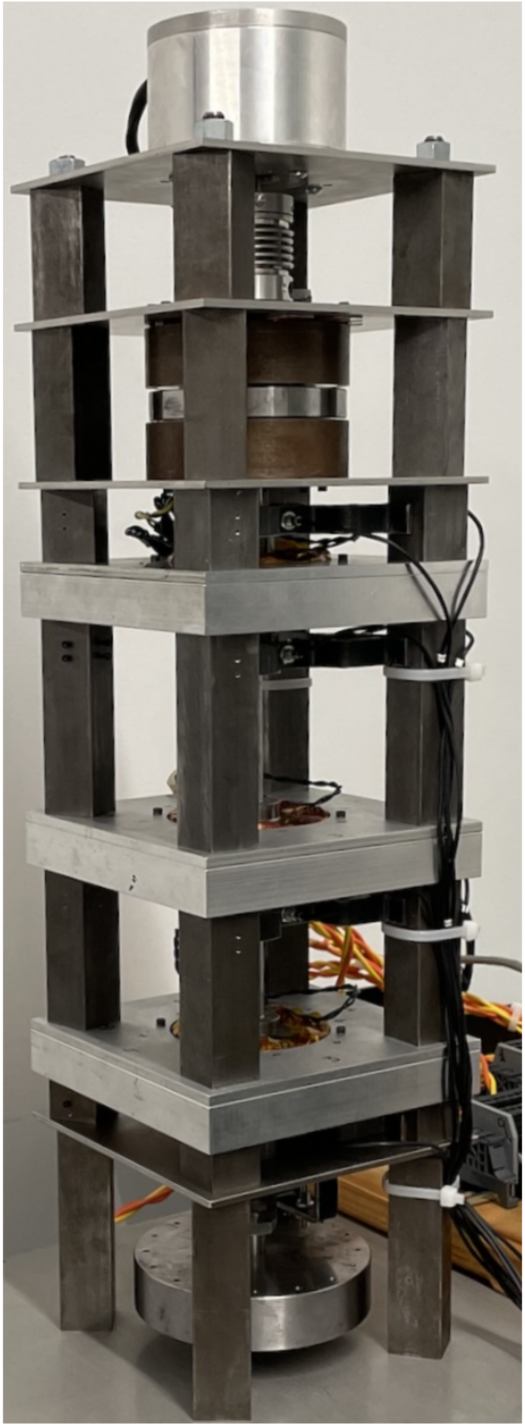

Figure 4: Honeywell High-Speed Magnetic Bearing Test Rig

3 System Modeling and Validation

An accurate mathematical model of the HMBTR is required to enable development of a high performance control design. Models for each of the individual components were developed from theory and validated with experimental data.

3.1 Rotor Dynamics Model

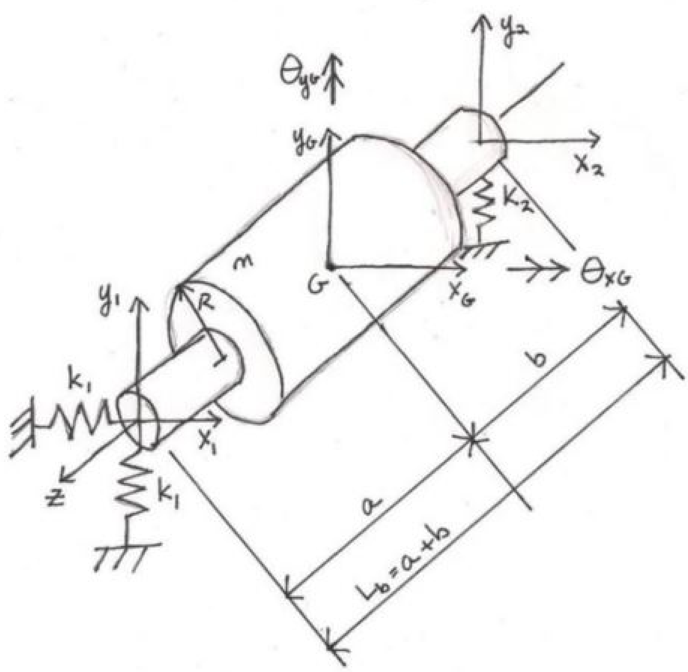

Figure 5: Rigid Rotor Free Body Diagram, from [6]

The free body diagram for a rigid rotor is shown in Figure 5. State variables are taken to be the lateral and angular displacements of the mass center in the horizontal (x) and vertical (y) directions: $[x_G, y_G, \theta_{xG}, \theta_{yG}]$. This amounts to 4 total physical degrees of freedom. It can move laterally in the x or y direction, or it can rotate about either the x-axis or the y-axis. J_p and J_t represent the polar and transverse moments of inertia. With this, the summations of forces and torques generated on the rotor about the mass center point are written:

$$
\begin{aligned}
m\ddot{x_G} + (k_1 + k_2)x_G + (-k_1 a + k_2 b)\theta_{yG} &= 0 \\
m\ddot{y_G} + (k_1 + k_2)y_G + (-k_1 a + k_2 b)\theta_{xG} &= 0 \\
J_t\ddot{\theta}_{xG} + J_p\Omega\dot{\theta}_{yG} + (-k_1 a + k_2 b)y_G + (k_1 a^2 + k_2 b^2)\theta_{xG} &= 0 \\
J_t\ddot{\theta}_{yG} - J_p\Omega\dot{\theta}_{xG} + (-k_1 a + k_2 b)x_G + (k_1 a^2 + k_2 b^2)\theta_{yG} &= 0
\end{aligned} \tag{5}
$$

These equations are combined and rewritten into matrix form to establish a general equation of motion for a rigid rotor:

$$M\ddot{q} + \Omega G\dot{q} + Kq = 0 \tag{6}$$

M is the rotor mass matrix and K is the bearing stiffness matrix. q is the state vector of displacements about the mass center point. G is the gyroscopic matrix that describes how the system dynamics change with rotating speed. This approximation is valid when the rotor is operated well below its first bending speed.

$$M = \begin{bmatrix} m & 0 & 0 & 0 \\ 0 & m & 0 & 0 \\ 0 & 0 & J_t & 0 \\ 0 & 0 & 0 & J_t \end{bmatrix} \tag{7}$$

$$K = \begin{bmatrix} k_1 + k_2 & 0 & 0 & -k_1 a + k_2 b \\ 0 & k_1 + k_2 & -k_1 a + k_2 b & 0 \\ 0 & -k_1 a + k_2 b & k_1 a^2 + k_2 b^2 & 0 \\ -k_1 a + k_2 b & 0 & 0 & k_1 a^2 + k_2 b^2 \end{bmatrix} \tag{8}$$

$$G = \begin{bmatrix} m & 0 & 0 & 0 \\ 0 & m & 0 & 0 \\ 0 & 0 & 0 & J_p \\ 0 & 0 & -J_p & 0 \end{bmatrix} \tag{9}$$

$$q = \begin{bmatrix} x_G \\ y_G \\ \theta_{xG} \\ \theta_{yG} \end{bmatrix} \tag{10}$$

3.1.1 Finite Element Model

The rotor system is more complicated when the driving speed approaches the first shaft bending speed, and the rotor must be regarded as flexible. In this case, a more detailed model is required in order to capture the shaft's flexibility and multiple vibrational natural frequencies. It is standard practice to employ the finite element modeling approach to define this model.

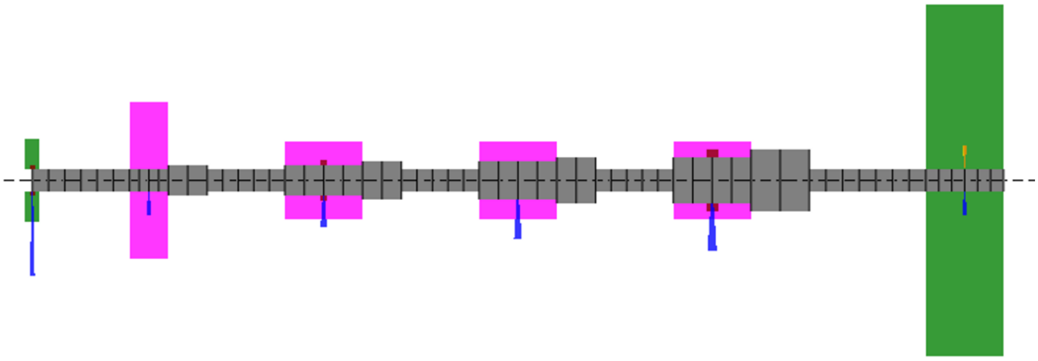

Figure 6: Finite Element Rotor Model

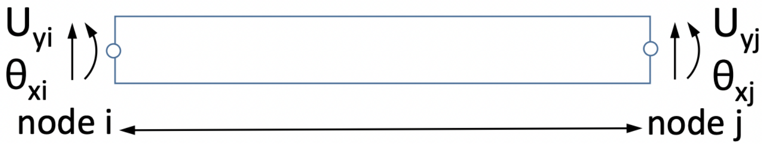

Figure 7: Finite Element

In this approach, the rotor is partitioned along its z axis into a set of segments. Each segment, or element, is modeled as a flexible beam having specific mass and elastic properties. The connection points between elements, or nodes, have 4 degrees of freedom: translations in the x and y directions and rotations about the x and y axes. Figure 6 shows the finite element model of the HMBTR and an example beam element is shown in Figure 7.

Conservation of energy is used to define equations of motion for each finite element. Define T as the total kinetic energy, V as the total potential energy, ζ_i as the generalized coordinates, and Ξ as the external forces. In its most general form, Lagrange's equation is written:

$$\frac{d}{dt}\left(\frac{\partial T}{\partial \dot{\zeta}}\right) - \frac{\partial T}{\partial \zeta} + \frac{\partial V}{\partial \zeta} = \Xi \tag{11}$$

Solving the coupled Lagrange equations yields lateral equations of motion for each beam element that are rewritten into the matrix form:

$$M_e \ddot{q}_e + \Omega G_e \dot{q}_e + K_e q_e = F_e \tag{12}$$

Where K_e is the element stiffness matrix, M_e is the element mass matrix, G_e is the element gyroscopic matrix, q_e is the element state vector, and F_e is the force on that element.

These element matrices are combined to form global matrices (M_f, G_f, K_f) that capture the dynamics of the full flexible rotor. Complete details of this process are discussed by Chaudhry [5]. The new system state vector q_f contains the lateral translations and rotations at every node. With this, a new equation of motion is formed:

$$M_f \ddot{q}_f + \Omega G_f \dot{q}_f + K_f q_f = 0 \tag{13}$$

3.1.2 State Space Model

The finite element model of the HMBTR was analyzed with the custom software package MODAL [16]. MODAL applies the transfer-matrix method to generate a standard state-space model that is defined by (14) and (15). The details on this process are well documented by Gunter [13].

$$\frac{d}{dt}\begin{Bmatrix} \underline{\omega}_x \\ \underline{\omega}_y \end{Bmatrix} = \begin{bmatrix} A & -\Omega G \\ \Omega G & A \end{bmatrix} \begin{Bmatrix} \underline{\omega}_x \\ \underline{\omega}_y \end{Bmatrix} + \begin{bmatrix} B & 0 \\ 0 & B \end{bmatrix} \begin{Bmatrix} \underline{f}_x \\ \underline{f}_y \end{Bmatrix} \tag{14}$$

$$\begin{Bmatrix} \underline{r}_x \\ \underline{r}_y \end{Bmatrix} = \begin{bmatrix} C & 0 \\ 0 & C \end{bmatrix} \begin{Bmatrix} \underline{\omega}_x \\ \underline{\omega}_y \end{Bmatrix} \tag{15}$$

The system inputs are forces applied at specific locations on the rotor $(\underline{f}_x, \underline{f}_y)$. System outputs are similarly designated displacements $(\underline{r}_x, \underline{r}_y)$. The system state vector $(\underline{\omega}_x, \underline{\omega}_y)$ is a modally reduced representation of the rotor state that retains 2 rigid body modes and multiple flexible modes (3 flexible modes in this example) for each radial direction (x, y).

When simplified to a single radial direction, inputs to the rotor are forces applied the rotor at the AMB locations (F_{DE}, F_{NDE}). The outputs are rotor displacements at the sensor locations ($X_{S,DE}$, $X_{S,NDE}$) and at AMB locations (X_{DE}, X_{NDE}). The generated A, B, C, and G matrices related to this simplified rotor model are reported in Appendix-B.

Analysis of the A matrix from 14 yields a set of eigenvalues and eigenvectors that characterize the rotor dynamics at stand-still. This calculation was completed with the built-in Matlab tool *eig*. The eigenvalues are the critical operating speeds that must be taken into account when determining a control design. They are listed in Table 6. Note that all of the free-free eigenvalues have negative real components, indicating that vibrations will always die out over time, as expected. The eigenvectors are the characteristic free-free mode shapes and are shown in Figure 8.

3.2 Rotor Model Validation

Experimental impact testing was performed in order to confirm that the frequency response of the rotor model matches the actual rotor. Frequency

$-7.0 \pm 703.0i$
$-30.0 \pm 3002.5i$
$-15.4 \pm 1537.4i$
$0 \pm 0i$
$0 \pm 0i$

Table 6: Rotor Eigenvalues

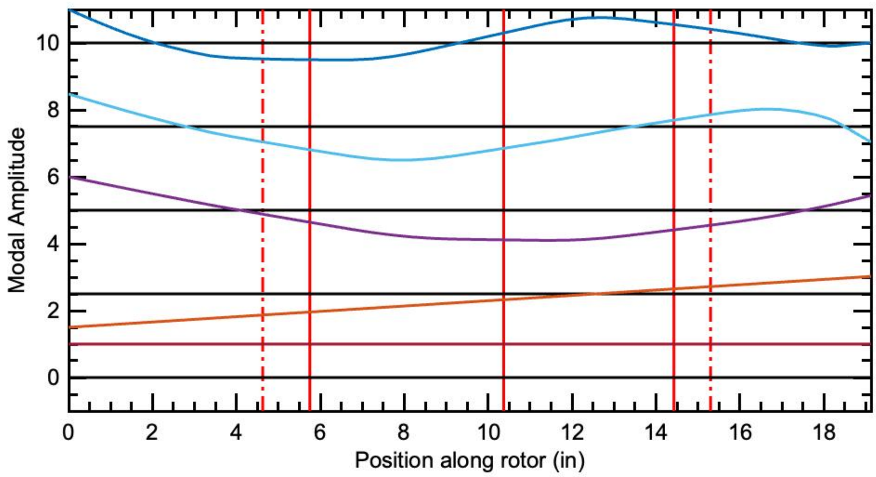

Figure 8: Rotor Free-Free Mode Shapes

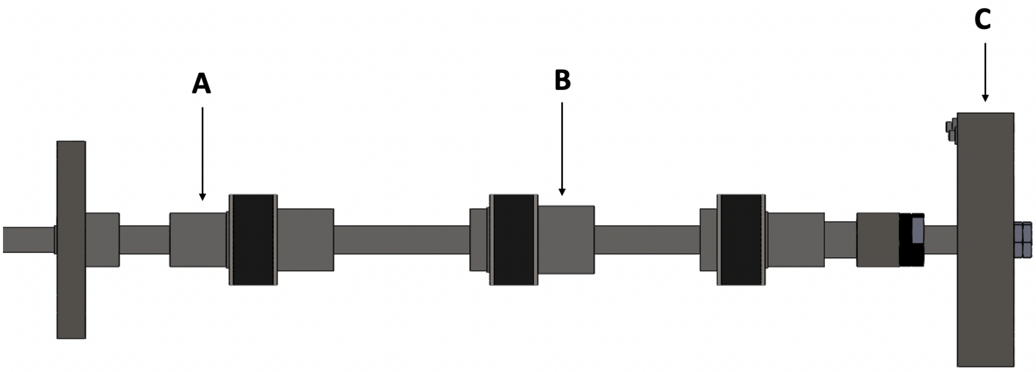

Figure 9: Experimental Impact Testing Input-Output Locations

response functions (FRF) were computed for the set of I/O locations: (Drive-End AMB, Exciter, Test Article). To generate each FRF, an instrumented modal impact hammer (PCB Piezotronics model 086A05) was used to deliver force and the corresponding rotor response was measured with an accelerometer (PCB Piezotronics model 321A). This was performed at the set of locations given in Figure 9. FRFs were generated using a Stanford Research Systems SR-785 dual-channel dynamic signal analyzer (DSA) and five averages were taken per calculation.

First, the rotor model frequency response was compared to experimental impact test data for the bare machined rotor. The DE AMB to Exciter (Input A to Output B) result is shown in Figure 10 and all other FRFs are included in Appendix-C.

Mode frequency locations and their associated peaks are well captured for most FRFs. However, each FRF with its displacement measured at the Test Article shows lower natural frequencies than predicted by the model. Because the test article end of the rotor is very thin and some modes generate a lot of motion at that location, these FRFs are more sensitive to differences between

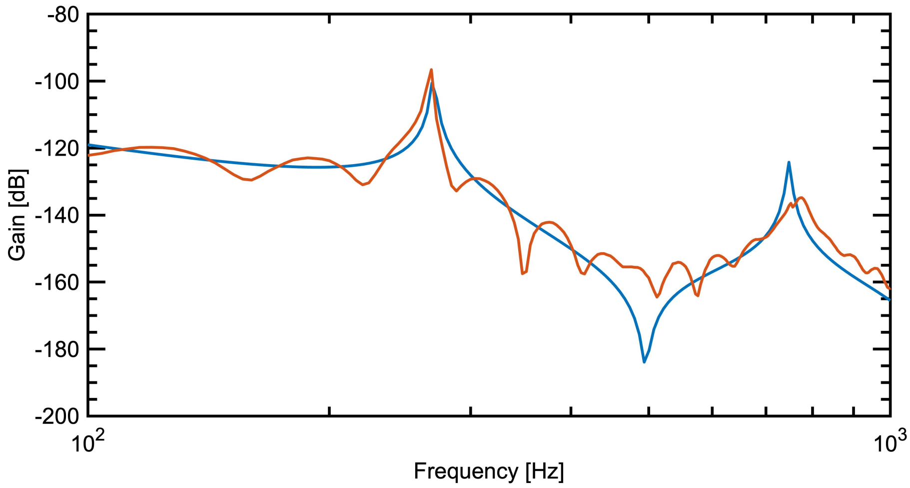

Figure 10: Input A to Output B: Experimental Data (Red) vs. Model (Blue)

the model and the actual system. Therefore, the weight of the accelerometer can not be considered negligible and will influence the system response when measured at the test article location. This additional mass shifts the natural frequency to the lower value shown by the experimental data.

For comparison, the mass of the accelerometer was included in the rotor model and this modified model was compared with experimental data for the DE AMB to Test Article FRF (Figure 11). Clearly any discrepancy can be attributed to accelerometer mass and otherwise each FRF matches the model up to 1 kHz. It was concluded that no changes to the bare rotor model were necessary.

With the bare rotor verified, the test article and thrust disc were installed and the rotor model was modified correspondingly. The same set of impact tests was conducted on the fully assembled rotor twice: once with the same nylon impact hammer tip as used for the bare rotor, and then a second

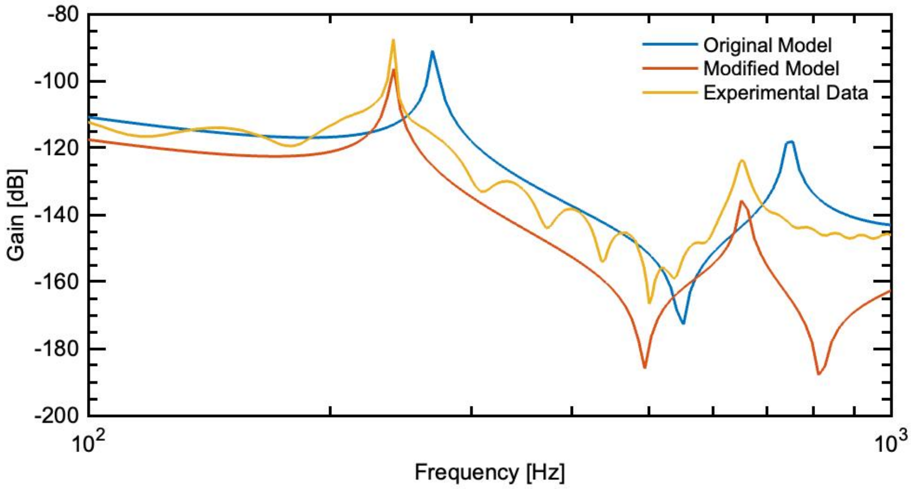

Figure 11: Bare Rotor: DE AMB to Test Article FRF

time with a harder tip. The softer impact hammer tip helped to isolate low frequency data, but a harder tip better resolved higher frequency modes. Data from the soft tip hammer is included in Appendix-C, and data from the hard tip is included in figs. 12 to 17.

Again, mode frequency locations and their associated peaks were well captured for most FRFs. The impact tests using the soft tip impact hammer are able to resolve them to around 600 Hz, and the hard tip to around 2000 Hz. However, some FRFs show a local minima at the second mode natural frequency. This can be explained by uncertainty in the effective stiffness of the AMB lamination stacks and the fact that the second mode has a node near the sensor location.

Many system zeros are not well matched, however these are known to be very sensitive to experimental error so these differences can be overlooked and should not impact the control design and overall behavior and performance of

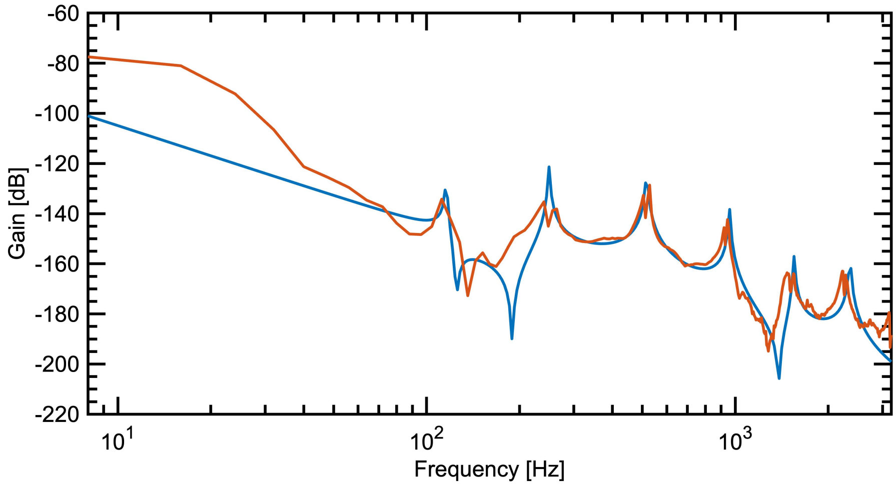

Figure 12: Input A to Output C: Experimental Data (Red) vs. Model (Blue)

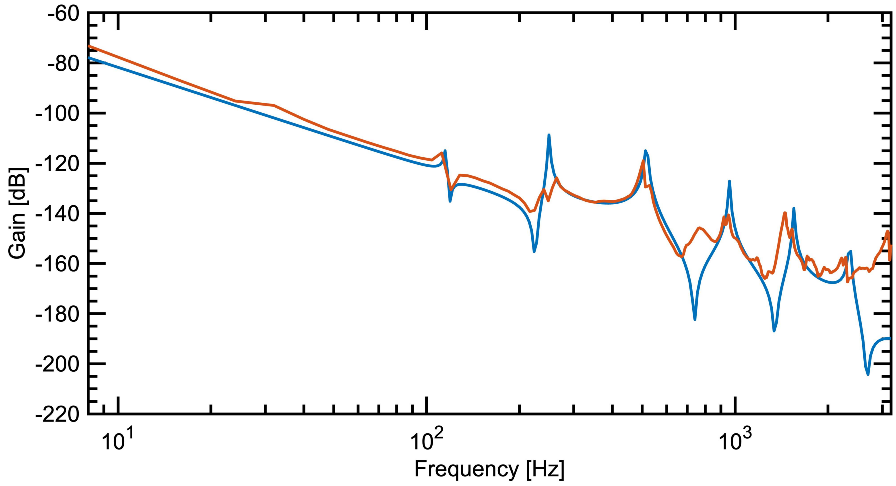

Figure 13: Input A to Output B: Experimental Data (Red) vs. Model (Blue)

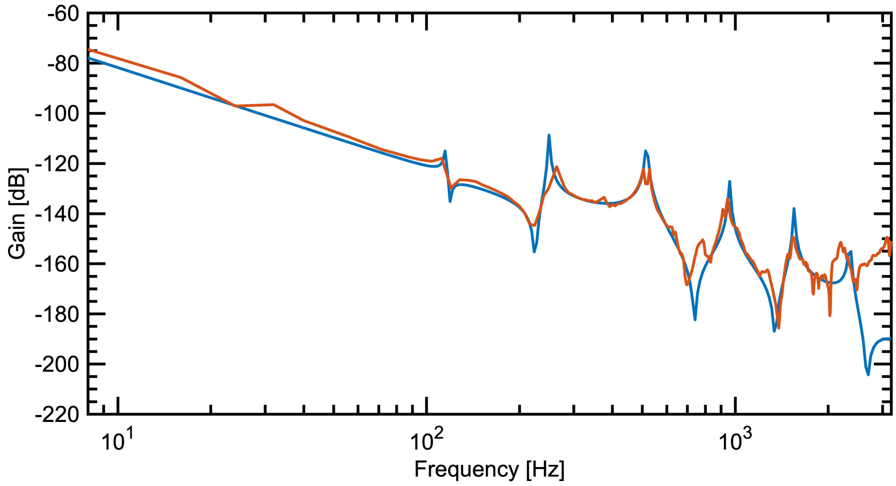

Figure 14: Input B to Output A: Experimental Data (Red) vs. Model (Blue)

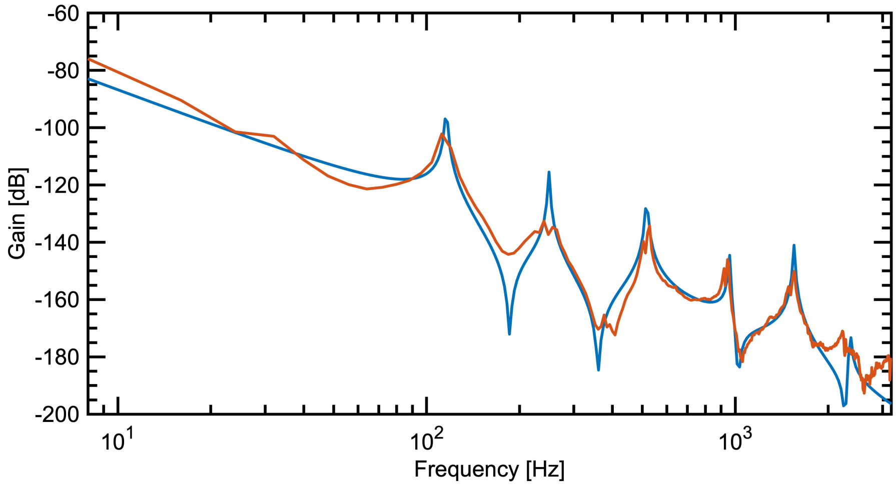

Figure 15: Input B to Output C: Experimental Data (Red) vs. Model (Blue)

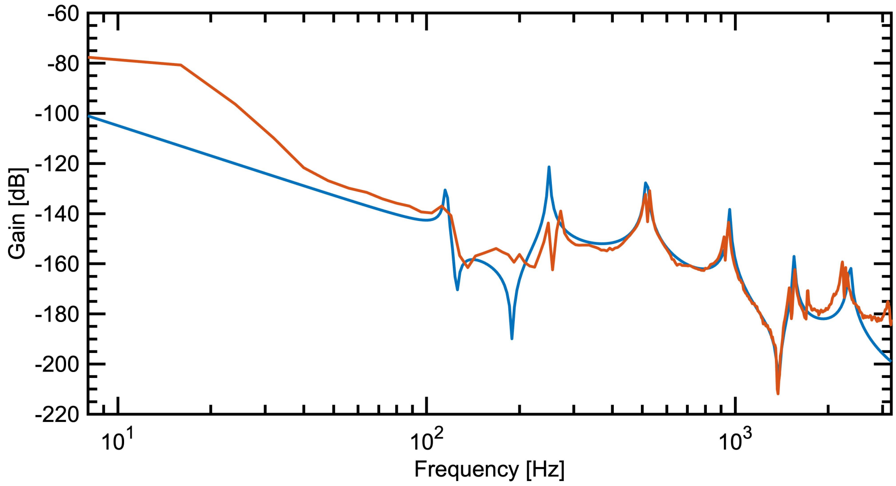

Figure 16: Input C to Output A: Experimental Data (Red) vs. Model (Blue)

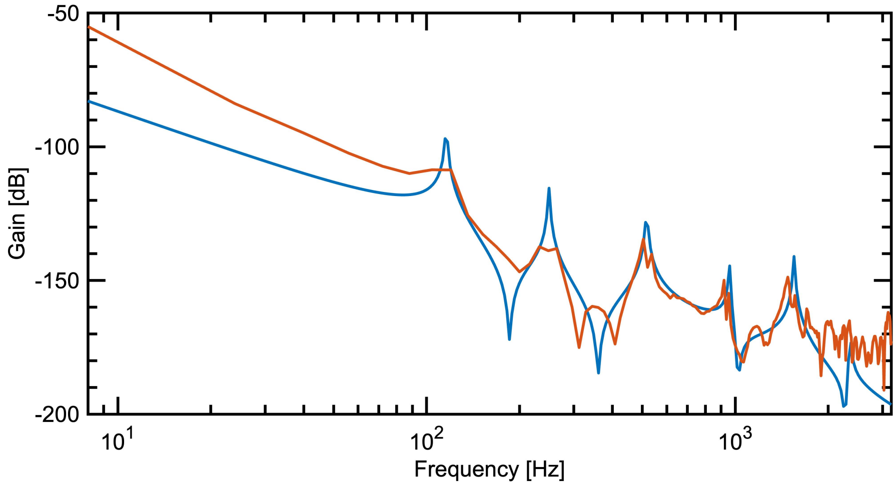

Figure 17: Input C to Output B: Experimental Data (Red) vs. Model (Blue)

the actual system. Finally, similar errors in low frequency gain are often seen in this type of impact testing with a hard-tip impact hammer. This effect is not observed in the soft-tip impact hammer results. With these validation steps complete, the rotor model was deemed to be accurate for the purposes of this work.

3.3 Amplifier-Actuator Model

A magnetic bearing can be abstracted on a basic level as a simple horseshoe shaped actuator that applies electromagnetic force directly to the rotor when an electrical current moves through its wire coils. Figure 18 shows a diagram of this type of simplified actuator.

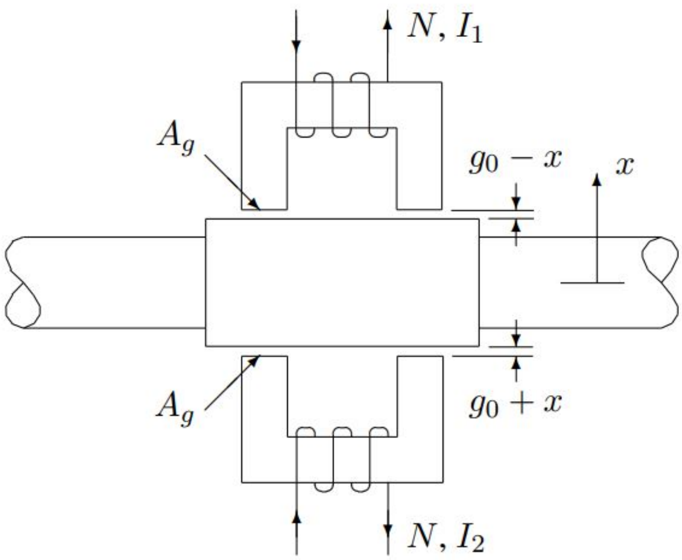

Figure 18: Linearized Actuator, from [15]

The single-sided force output of this actuator is written as a function of its physical parameters: number of coil windings (N), pole face area (A_g), air gap (g), relative permeability (μ_r), and mean magnetic path length (l). Also relevant are the actuator current (i), and the Permeability of Free Space (μ_0). This force equation is written:

$$F = \frac{\mu_0 N^2 i^2 A_g}{(2g + \frac{l}{\mu_r})^2} \tag{16}$$

Because electromagnets can only apply attractive forces, these actuators are often paired together to enable bi-directional control. The actuators used for the HMBTR are constructed in this way. The currents applied to each actuator pair (i_1, i_2) are characterized by a bias (i_b) and a perturbation amount (i_p). Similarly, the air gaps as measured from each actuator (g_1, g_2) are written using a nominal gap (g_0) and a rotor displacement (x):

$$i_1 = i_b + i_p$$

$$i_2 = i_b - i_p$$

$$g_1 = g_0 - x$$

$$g_2 = g_0 + x$$

With this construction, a two-sided force equation is written:

$$F = \mu_0 N^2 A_g \left(\frac{i_b + 2i_b i_p + {i_p}^2}{(2g_1 + \frac{l}{\mu_r})^2} - \frac{i_b - 2i_b i_p + {i_p}^2}{(2g_2 + \frac{l}{\mu_r})^2}\right) \tag{17}$$

This equation is simplified for controls analysis by linearizing around the nominal gap (g_0). Then, actuator force is only dependent on its input current and the rotor position. (18) is formed by defining the Actuator

Current Gain (k_i) and the Actuator Open Loop Stiffness (k_x). Of course, there are some system inefficiencies such as fringing and magnetic leakage losses. These losses are typically accounted for with a correction coefficient η. Baun experimentally determined k_i and k_x values for these actuators and they perform as expected when accounting for a standard η coefficients of 0.9 for the thrust bearing and 0.8 for the radial bearing.

$$F = k_i i_p - k_x x \tag{18}$$

$$k_i = \frac{4\mu_0 N^2 A i_b}{(2g_0 + \frac{l}{\mu_r})^2} \tag{19}$$

$$k_x = -\frac{8\mu_0 N^2 A {i_b}^2}{(2g_0 + \frac{l}{\mu_r})^3} \tag{20}$$

Lower AMB bias currents were used for the initial control designs that were developed and used for system identification. Also, a much larger gap size was implemented on the thrust axis. These parameter changes are documented in Table 7. The k_i and k_x values that were predicted and experimentally determined previously were scaled based on these parameter changes and recorded in Table 8.

	$i_{b-radial}$ A	$i_{b-thrust}$ A	$g_{0-thrust}$ in
Specified:	1.2	1.75	0.03
Implemented:	0.5	1.0	0.06

Table 7: AMB Design Changes

	k_{i-th} lbf/A	k_{x-th} lbf/in	k_{i-exp} lbf/A	k_{x-exp} lbf/in
Radial:	0.57	-9.03	0.59	-2.6
Thrust:	0.53	-1.31	0.39	-0.85

Table 8: k_i and k_x, Thrust and Radial Actuators

3.3.1 Amplifier Dynamics

The amplifier is inherently coupled to the actuator. The actuator requires a driving electrical power source and the amplifier cannot function without a load. This system is described by the block diagram shown in Figure 19.

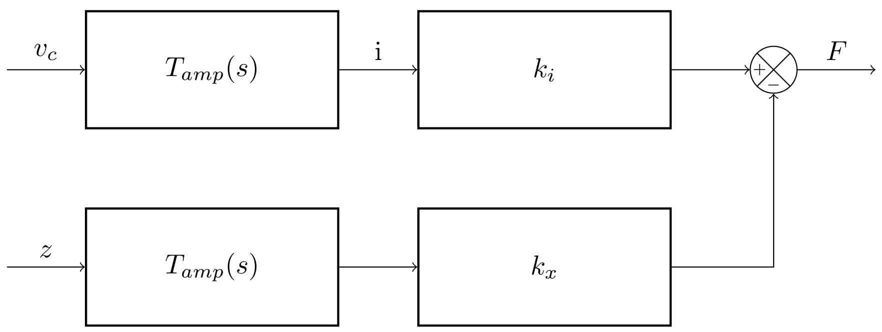

Figure 19: Amplifier-Actuator System Block Diagram

An experimental procedure was conducted to make an estimate of the amplifier dynamics ($T_{amp}(s)$). A swept sine wave control voltage signal was applied to the amplifier and the resulting current through the actuator was recorded, giving the frequency response shown in Figure 20 for the radial bearing and Figure 21 for the thrust bearing. First order transfer functions were chosen for both amplifiers to best match the experimental data:

$$T_{amp-radial}(s) = \frac{1.0}{\frac{1}{(2\pi)1350}s + 1} \tag{21}$$

$$T_{amp-thrust}(s) = \frac{1.0}{\frac{1}{(2\pi)850}s + 1} \tag{22}$$

The thrust bearing has a lower bandwidth than the radial bearing, but there is a much smaller bandwidth difference between the two than is usually expected. This indicates that eddy current effects minimally affect the bandwidth of the thrust bearing in this case. Thrust bearings are often un-laminated due to their geometry, and as a result significant eddy currents are generated during their operation. The effect is to counteract magnetic flux induction at high frequencies and therefore effectively limit controller bandwidth. A detailed discussion of eddy current dynamics is found in [19]. This thrust bearing was manufactured using an innovative powder metal manufacturing method intended to minimize eddy current losses (See [3]), resulting in improved performance.

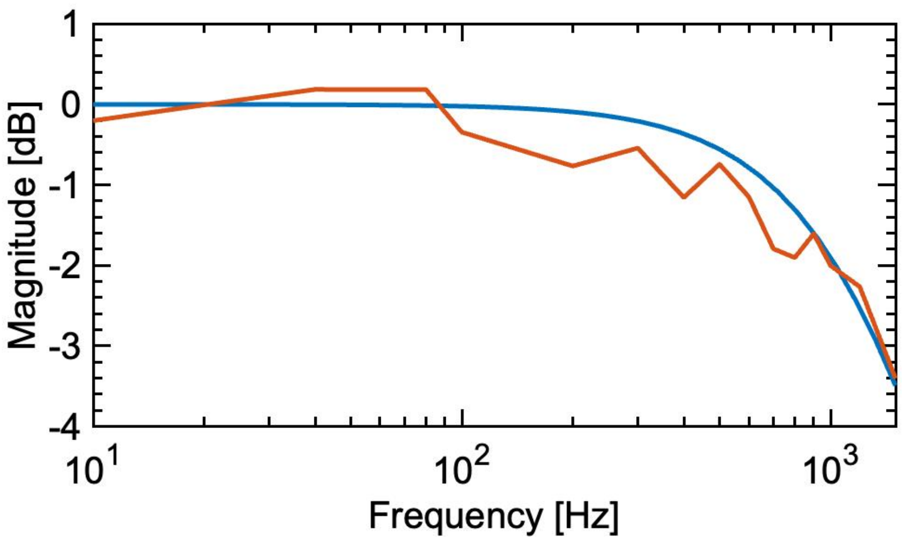

Figure 20: Radial Amplifier Frequency Response: Experimental Data (Red) vs. Model (Blue)

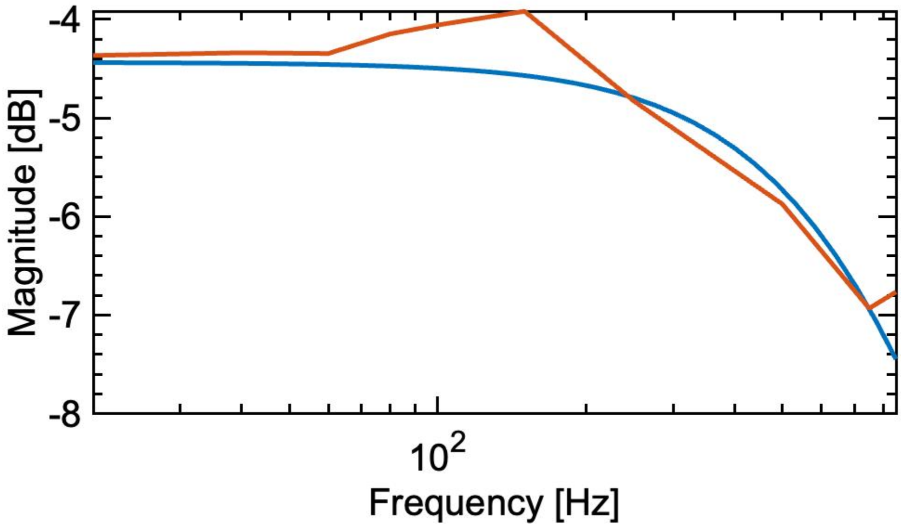

Figure 21: Thrust Amplifier Frequency Response: Experimental Data (Red) vs. Model (Blue)

The amplifiers that were used for the HMBTR allowed choice of gain (k_a) and a value of $0.6\,\mathrm{A\,V^{-1}}$ was implemented. With these parameters established, the amplifier-actuator dynamics of the MIMO radial AMB system are given by the transfer function matrices (TFMs):

$$K_i = \begin{bmatrix} k_a k_i T_{amp}(s) & 0 \\ 0 & k_a k_i T_{amp}(s) \end{bmatrix} \tag{23}$$

$$K_x = \begin{bmatrix} k_x T_{amp}(s) & 0 \\ 0 & k_x T_{amp}(s) \end{bmatrix} \tag{24}$$

3.4 Sensor Model

The position sensor was modeled as an $8000\,\mathrm{V\,m^{-1}}$ simple gain as defined by its supplier documentation. The sensor bandwidth is $10\,\mathrm{kHz}$ and is well over the system bandwidth. So, sensor dynamics will not meaningfully affect the system and they can be neglected in the model. This gives the transfer function matrix:

$$K_s = \begin{bmatrix} 8000 & 0 \\ 0 & 8000 \end{bmatrix} \tag{25}$$

3.5 Digital Controller

Digital control systems operate on a per-sample basis, meaning that system outputs are only updated at discrete timesteps that are dictated by the sampling rate (T_s). Problems with signal aliasing will emerge if the sampling rate is not far above the frequency of operation. Per the Nyquist Sampling Theorem, there will be data lost for all frequencies greater than 1/2 of the sampling frequency. In practical use, the sampling rate should be at least 5 times that highest frequency of interest. However, the DSP must also be fast enough to execute the control algorithm within the sampling time. Balancing these constraints, a sampling rate of 5 kHz was implemented.

This sampling process will physically present as a delay or phase lag. However, in this case, the controllers that were implemented roll off at a much lower frequency than the sampling frequency. Therefore, sampling delay can be ignored in the system model. To confirm this, the frequency response of this transfer function approximation and the experimental response for a PID control algorithm are shown in Figure 22. There is an excellent match through the relevant frequency range.

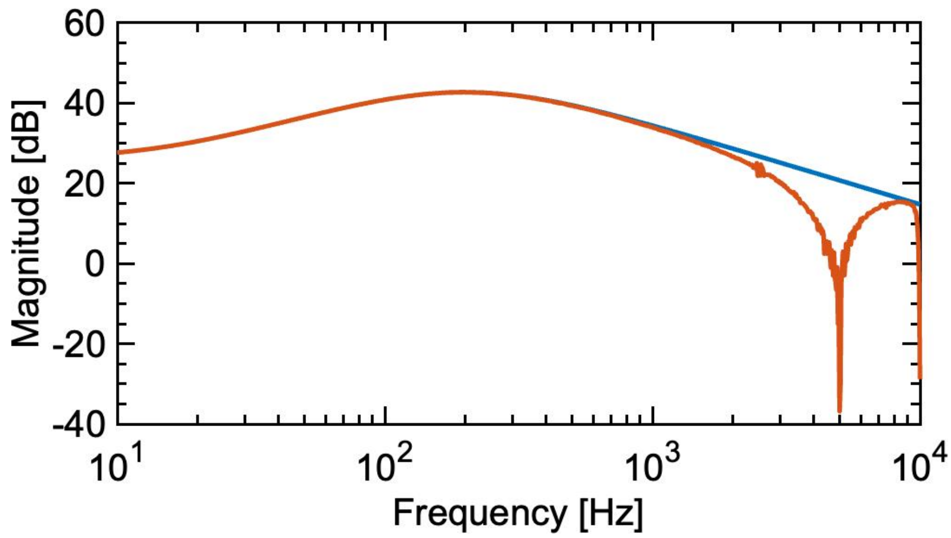

Figure 22: Digital Controller: Experimental Data (Red) vs. Model (Blue)

3.6 Closed Loop System Model

Finally, the full closed loop model for the radial direction is formed as shown in Figure 23 where G_{cntr} models the implemented control design. Rotor model input-output relations are defined in Table 9.

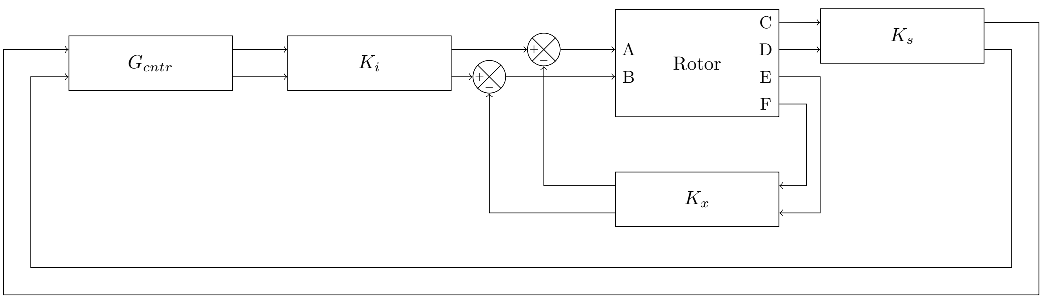

Figure 23: Radial System Block Diagram

The axial system is described by the block diagram given in Figure 24. In this case, the rotor is modeled as just a simple mass (m) with the transfer function given by (26) and controller G_{Th}.

A	F_{DE}
B	F_{NDE}
C	$X_{S,DE}$
D	$X_{S,NDE}$
E	X_{DE}
F	X_{NDE}

Table 9: Rotor Model IO

$$Rotor = \frac{1}{ms^2} \tag{26}$$

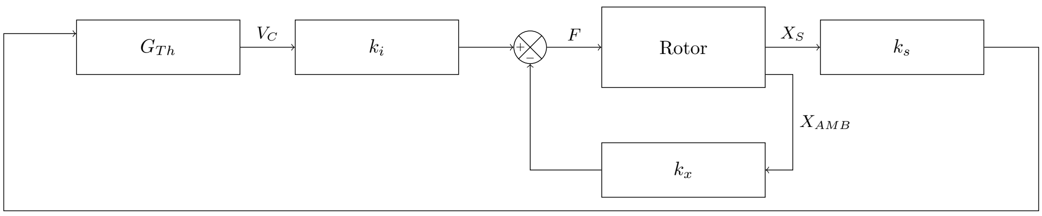

Figure 24: Axial System Block Diagram

3.7 Closed Loop System Model Validation

Gahler et. al. defined an on-line MIMO system identification approach that was particularly useful for validation of this plant model [7]. After levitating the rotor with a nominal PID control scheme, precise perturbation signals were applied to each AMB and the responses at each sensor were recorded. As such, a 'Sine Sweep' system identification method was performed. In this, the system was excited at a single frequency at a time, and the response was measured at each individual frequency to form a frequency response plot. Notably, this procedure results in much smoother response plots compared to the impact hammer method. Experimental data is compared to the corresponding model frequency responses in figs. 25 to 29.

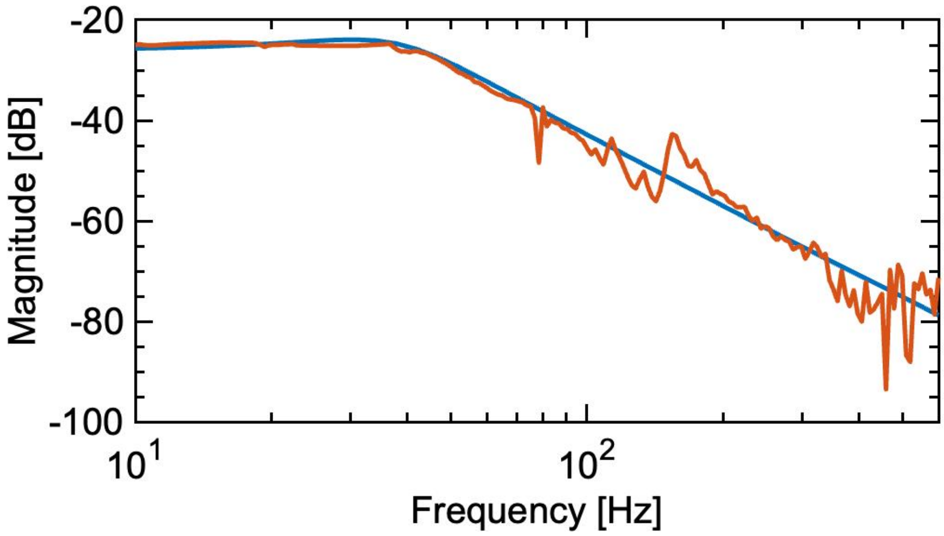

Figure 25: Thrust AMB Input to Thrust Sensor Output: Experimental Data (Red) vs. Model (Blue)

Starting with the axial direction, the system model matches the experimental data quite well up to approximately 500 Hz (well beyond the closed-loop system bandwidth). However, there is an unmodeled mode at around 150 Hz that will require additional investigation.

System level validation testing was also performed for the closed loop lateral system using a preliminary PID control design and a similar testing method to that used for the thrust axis. The radial experimental results demonstrate the importance of accurate system modeling and present some important takeaways. First, resonance peak mismatches are observed throughout the data and can be attributed to modeling errors in K_i and K_x as there is relatively high uncertainty in those parameters.

An additional resonance is observed in all datasets at around 30 Hz and

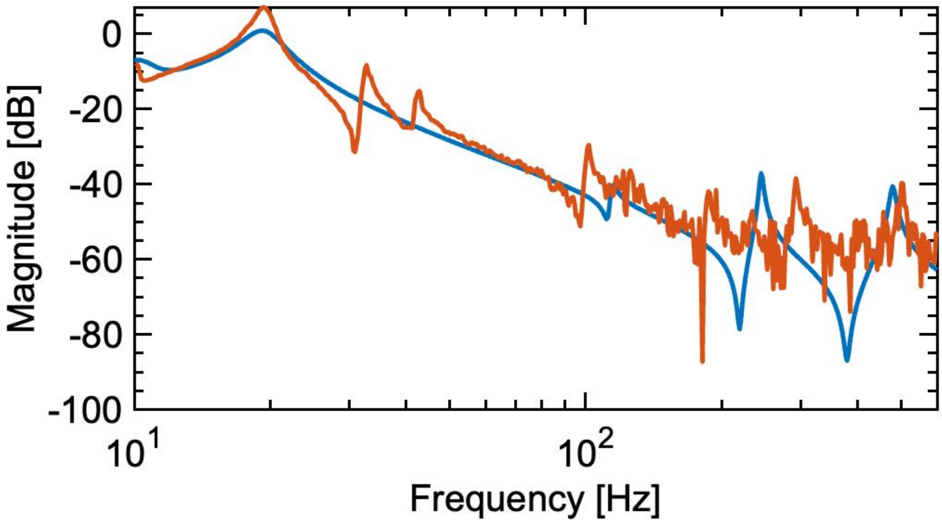

Figure 26: DE-AMB Input to DE-Sensor Output: Experimental Data (Red) vs. Model (Blue)

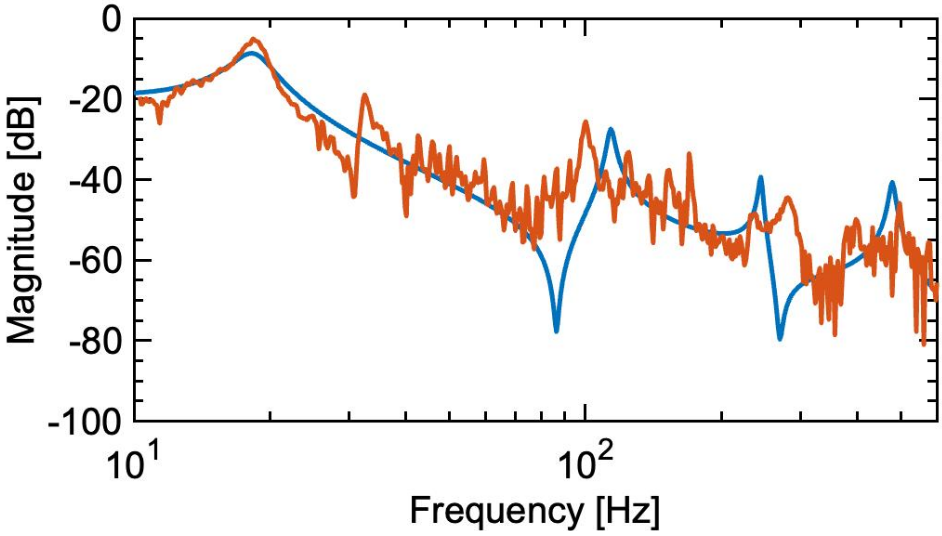

Figure 27: DE-AMB Input to NDE-Sensor Output: Experimental Data (Red) vs. Model (Blue)

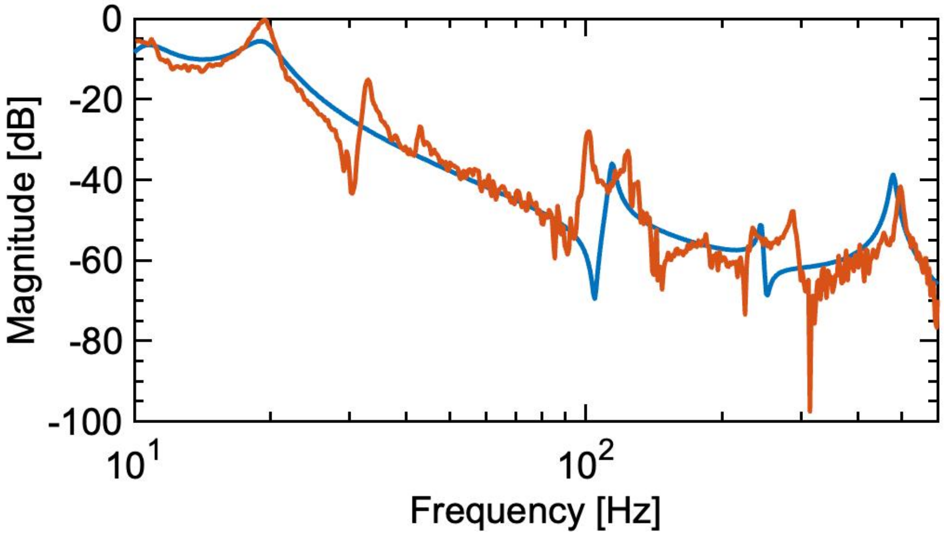

Figure 28: NDE-AMB Input to DE-Sensor Output: Experimental Data (Red) vs. Model (Blue)

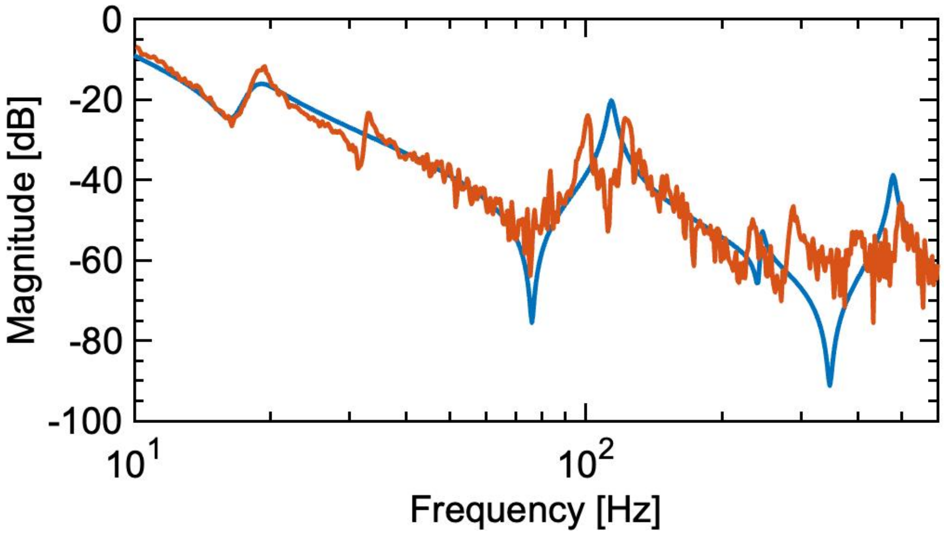

Figure 29: NDE-AMB Input to NDE-Sensor Output: Experimental Data (Red) vs. Model (Blue)

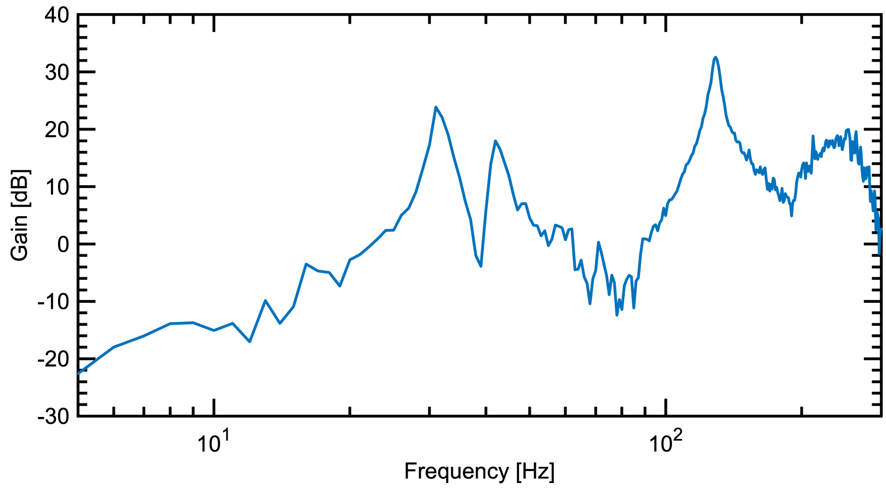

Figure 30: Test Rig Structure Frequency Response

the resonance that is predicted at approximately 100 Hz exhibits a double peak instead of the predicted single peak. To investigate this, an impact hammer test was performed on the test rig housing in the lateral direction (Figure 30). These results indicate that there are substructure modes at approximately 30 Hz and 150 Hz. Thus, substructure dynamics can explain the un-modeled low-frequency resonance and double resonant peak observed in the closed loop frequency response data.

Despite these discrepancies, the closed loop model was deemed satisfactory through 500 Hz such that a more detailed controller synthesis and analysis could begin.

4 HMBTR - Control Design

With a suitably accurate closed loop system model validated, attention turned to controller design. The high expected operational speed combined with the flexibility of the rotor established constraints on stability and performance. The rig passes through the first rotor bending mode in normal operation, causing the potential for excessive vibrations and instability. With this in mind, minimization of displacement due to unbalance force and robustness to variation in system properties were established as performance objectives. Both of these performance objectives were evaluated and compared to the standards established in ISO-14839 [8].

4.1 Performance Goal

Performance measures for the closed loop system were defined with respect to the simplified block diagram given in Figure 31. The effects of input disturbance (F_d) and sensor noise (n) on the measured output rotor position (x_{sense}) was considered.

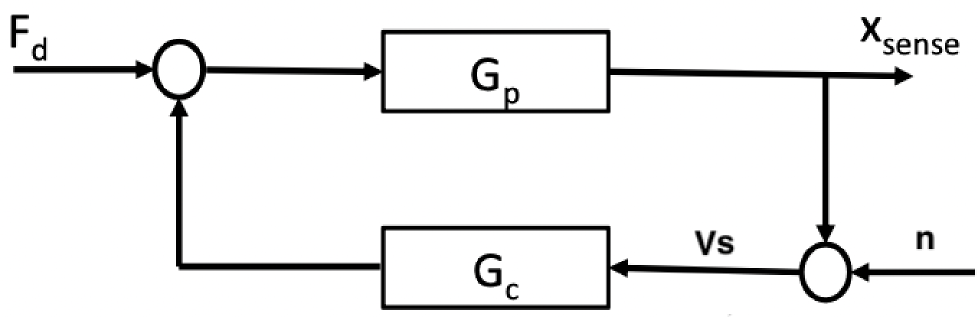

Figure 31: Simplified Closed Loop System Block Diagram

Compliance is defined as the response of the closed loop system to external disturbance. The primary control objective is to minimize the displacement measured at each AMB location (x_{sense}) that results from an input force applied at the test article (F_d). Furthermore, the main driver of this input force is rotordynamic unbalance. A standard unbalance of $0.03\,\mathrm{oz}-\mathrm{in}$ results in a frequency-dependent unbalance force:

$$F_{unb} = 0.03\omega^2 \tag{27}$$

The maximum vibration level in response to unbalance is required to be less than 30% of the minimum clearance (C_{min}) between the rotor and stator:

$$x_{max} < 0.3C_{min} \tag{28}$$

For the HMBTR, C_{min} is the clearance at the mechanical back-up bearings (Nominally 0.015 in).

Additionally, limitations on AMB load capacity were considered. Magnetic saturation constrains actuator performance to a Peak Load Capacity of 20 lbf (From Table 4). Unbalance force (F_{unb}) must not exceed the load capacity for any frequency in the operating range.

The other key metric for this system is its robustness to variation in system properties. The goal is for the system output to be minimally sensitive to process variation. This is quantified by the Sensitivity Function (M_s): the closed loop system response between a disturbance input at the sensor output and the associated control output signal:

$$M_s = \frac{V_s}{n} \tag{29}$$

If M_s is greater than 1 at a certain frequency, then the disturbance signal will be amplified. The goal is to minimize the peak M_s value. Lower overall sensitivity indicates that the system is more robust to disturbances and modeling errors. For more information on the sensitivity functions, see [2].

The ISO-14839 Standard specifies a set of Stability Zones of AMB supported machines. New machines are expected to conform to Stability Zone A. Zone B is acceptable for long term operation. Zone C indicates that the machine needs attention soon. A maximum peak M_s value is specified for each Stability Zone.

4.2 Thrust Bearing PID Control Design

Two different PID controllers were designed for the thrust bearing and tuned experimentally. First, a low gain, low bandwidth controller was implemented. The controller is expressed by:

$$G_{PID} = K_p + \frac{K_i}{s} + \frac{K_d s}{T_f s + 1} \tag{30}$$

The controller parameters are given in Table 10. A first-order low pass filter with a 200 Hz cutoff frequency was added in-series in order to help with noise attenuation for initial system levitation and operation.

A second, higher-bandwidth PID controller was implemented as well (See Table 11). In this case, a third-order low pass filter with 500 Hz cutoff frequency was included.

Proportional Gain	K_p	20
Derivative Gain	K_d	0.1
Integral Gain	K_i	5
Time Constant	T_f	7.96×10^{-4}

Table 10: Initial Thrust Controller Parameters

Proportional Gain	K_p	20
Derivative Gain	K_d	0.005
Integral Gain	K_i	5
Time Constant	T_f	3.18×10^{-4}

Table 11: Higher-Bandwidth Thrust Controller Parameters

The frequency responses of both control designs are shown in Figure 32.

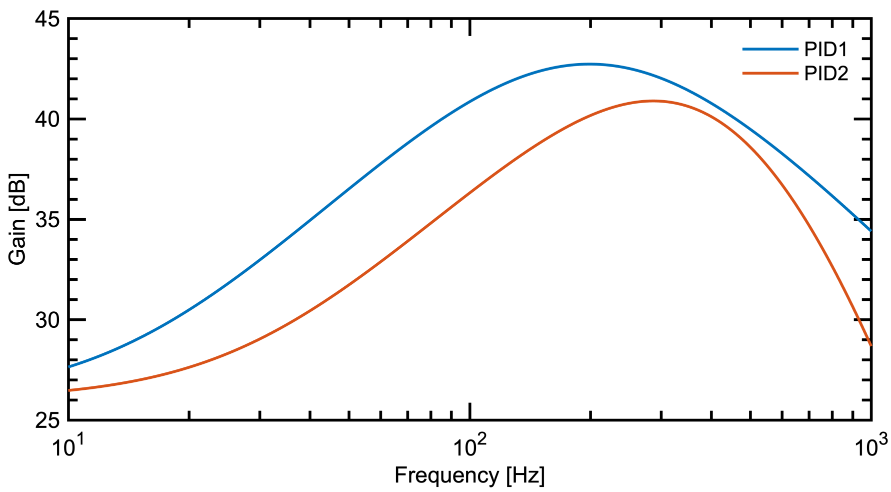

Figure 32: Thrust Axis PID Controller Transfer Functions

4.3 Radial Bearing PID Control Design

Radial control was performed by two independent SISO PID controllers for the DE and NDE AMBs with the controller terms given in Table 12.

An integrator was applied to just the NDE controller in order to improve low frequency performance and remove steady state error. A second-order low pass filter with a 600 Hz cutoff frequency was added in-series with each controller input in order to help attenuate noise for initial system levitation and operation.

DE Proportional Gain	K_p	5
DE Derivative Gain	K_d	0.06
DE Integral Gain	K_i	0.0
DE Time Constant	T_f	2.65×10^{-4}
NDE Proportional Gain	K_p	5
NDE Derivative Gain	K_d	0.06
NDE Integral Gain	K_i	0.5
NDE Time Constant	T_f	2.65×10^{-4}

Table 12: Radial Controller Parameters

The flexible nature of the rotor with multiple relatively low frequency bending modes required further gain stabilization just to achieve nominal stability. Specifically, during initial testing it was discovered that both the first and third bending modes required additional attenuation. A Notch filter applies gain compensation to a narrow band of frequencies and can be used to attenuate particularly problematic modes. The transfer function for a notch filter is given by 31. Notch frequency (ω_n) and notch depth (ζ_1) parameters determine the shape of the notch. For this, the notch filter frequencies (112 and 480) were chosen by placing the notch directly on the bending modes to be stabilized. The frequency response for the resulting control design is shown in Figure 33.

$$G_n = \frac{s^2 + 2\zeta_1 \omega_n s + {\omega_n}^2}{s^2 + 2\zeta_2 \omega_n s + {\omega_n}^2} \tag{31}$$

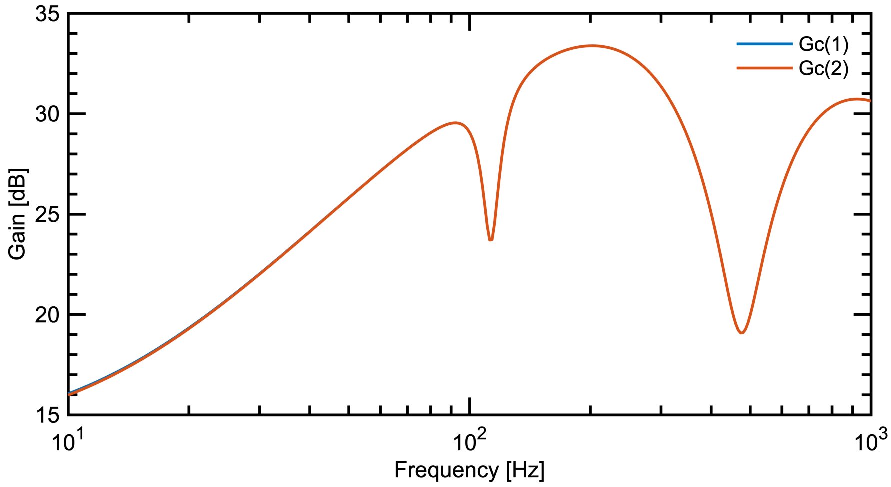

Figure 33: Radial Axis PID Controller Transfer Function

4.4 Modal PID Control Design

The PID controllers that have been developed so far are entirely SISO: displacements at the DE sensor do not affect the control commands that are sent to the NDE AMB and vice-versa. It has been shown [6] that improved performance of lateral AMB supported rotors can be achieved using a Modal Multi-Input Multi-Output control design technique. With this in mind, the T and T_s transformation matrices are defined from rotor dimensions given by Figure 34. These transformation matrices convert the I/O of the original plant model from physical coordinates to the rotation and translation of the rotor's center of mass (θ, x_c). This transformation is given by (34) where G_P is the original plant model and G_{PM} is the new modal coordinate model.

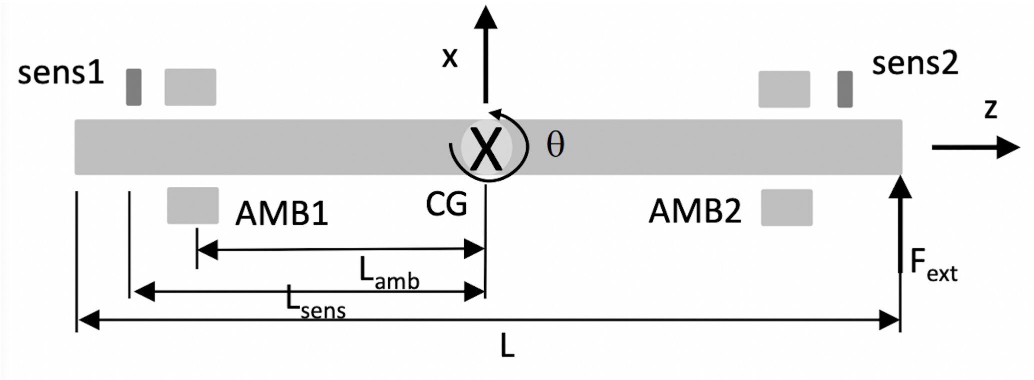

Figure 34: Modal Transformation System Diagram

$$T = \begin{bmatrix} 1 & -L_{AMB-DE} \\ 1 & L_{AMB-NDE} \end{bmatrix} \tag{32}$$

$$T_s = \begin{bmatrix} 1 & -L_{Sens-DE} \\ 1 & L_{Sens-NDE} \end{bmatrix} \tag{33}$$

$$G_{PM}(s) = T^{-T} G_P T_S^{-1} \tag{34}$$

This transformation results in new plant dynamics and a decoupling of the system. To show this, the frequency responses of the modal coordinate model are compared with the physical coordinate model in figs. 35 to 38. At least at low frequencies, the magnitudes of the off-diagonal transfer functions have decreased by a significant factor, indicating that the control of each degree of freedom (DOF) is now largely independent of the other.

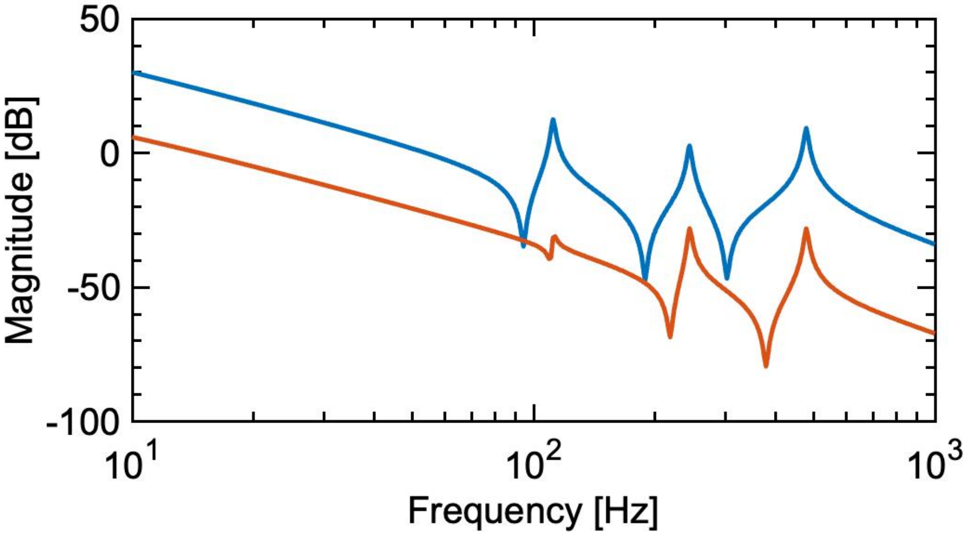

Figure 35: Frequency Response: $G_{PM}(1,1)$ (Blue) vs. $G_P(1,1)$ (Red)

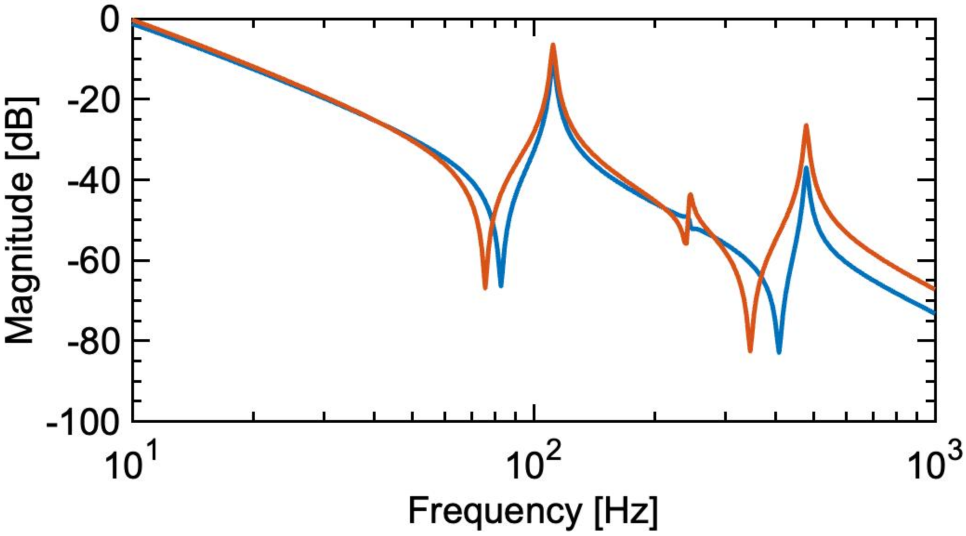

Figure 36: Frequency Response: $G_{PM}(2,2)$ (Blue) vs. $G_P(2,2)$ (Red)

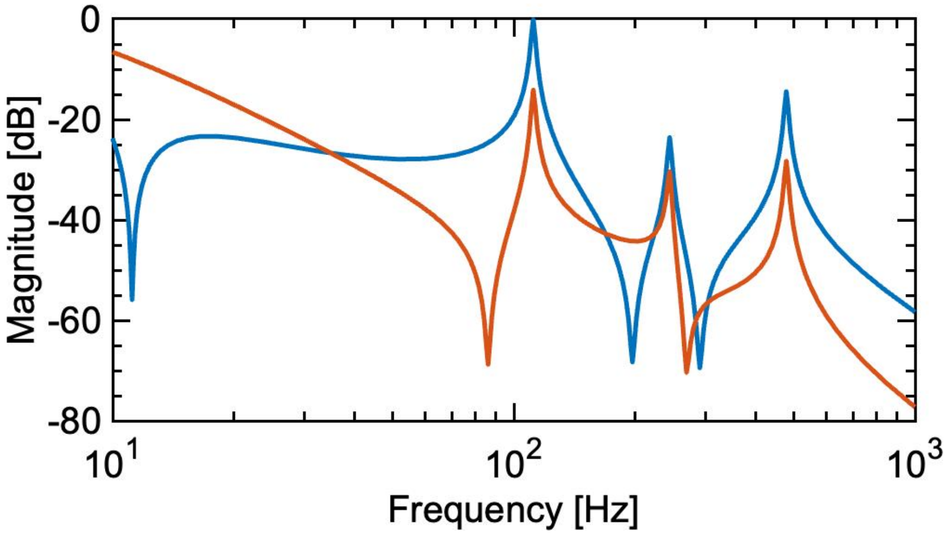

Figure 37: Frequency Response: $G_{PM}(2,1)$ (Blue) vs. $G_P(2,1)$ (Red)

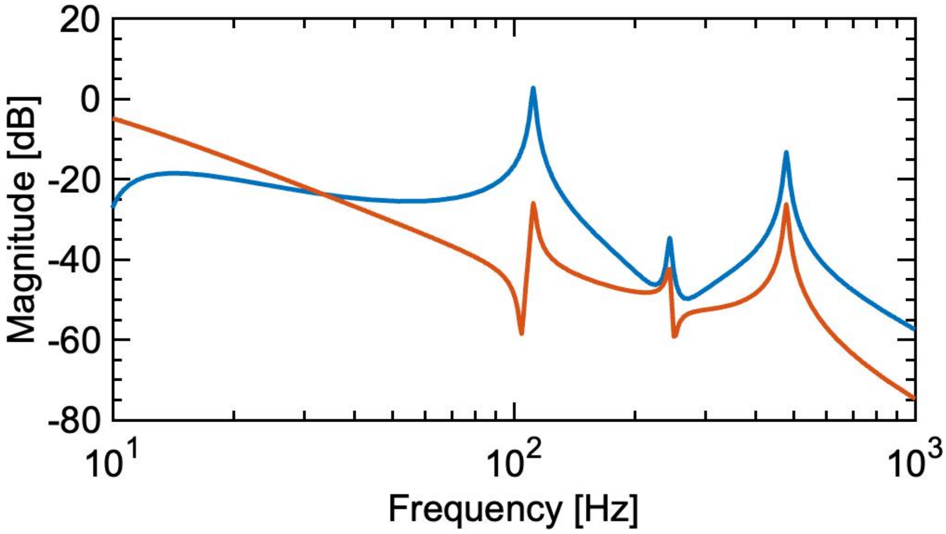

Figure 38: Frequency Response: $G_{PM}(1,2)$ (Blue) vs. $G_P(1,2)$ (Red)

4.4.1 Closed Loop System Stabilization

Next, lead-lag compensators were designed separately for each decoupled DOF:

$$G_\theta = 0.5 \frac{\frac{1}{80}s + 1}{\frac{1}{2\pi 600}s + 1} \tag{35}$$

$$G_{xc} = 5 \frac{\frac{1}{80}s + 1}{\frac{1}{2\pi 500}s + 1} \tag{36}$$

$$G_M = \begin{pmatrix} G_\theta & 0 \\ 0 & G_{xc} \end{pmatrix} \tag{37}$$

The system response at the rotor's bending frequencies must also be attenuated to ensure closed loop stability. The Nyquist Plot is used to help determine a filter design that will attenuate these modes without disturbing the lower frequency phase lead compensation. By the Nyquist Stability Criterion, the CL system is stable if the number of encirclements of the -1 point on the Nyquist plot is equal to the number of unstable poles of the OL transfer function. The transfer functions corresponding to each DOF each have one pole in the RH plane. Therefore, each Nyquist plot must have one CCW encirclement to ensure closed-loop stability. With this in mind, a 478 Hz notch filter at the third bending frequency was added to both controllers. Nyquist plots for the resulting system are shown in Figure 39 and Figure 40 and they indicate that the system as designed meets the Nyquist Stability Criterion and is therefore nominally stable. Note that an arrowed plot-line indicates that the encirclement completes outside of the plotted area.

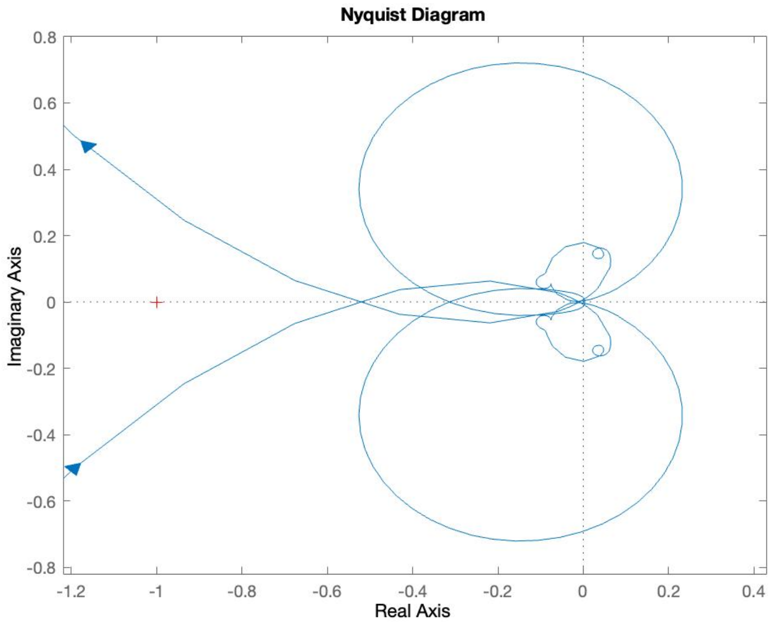

Figure 39: Nyquist Plot: Translational DOF

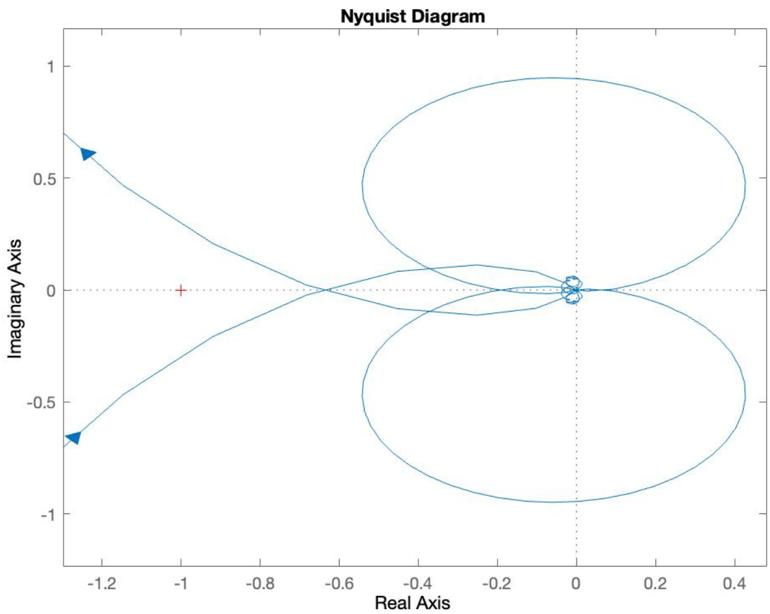

Figure 40: Nyquist Plot: Rotational DOF

4.4.2 Rotor Asymmetry Kx Compensation

This modal transformation works well for symmetric rotors, but there is additional complication for the HMBTR (discussed in detail in [12]). The rotor is asymmetric and the mass center does not sit at its geometric center. Therefore, the distance from the center of gravity to each radial bearing is different. Each bearing will exert a different torque about the COG for the same force input, resulting in a different effective negative stiffness (K_{sx}).

$$K_{sx} = k_x \begin{bmatrix} L^2_{AMB-DE} + L^2_{AMB-NDE} & -L_{AMB-DE} + L_{AMB-NDE} \\ -L_{AMB-DE} + L_{AMB-NDE} & k_x \end{bmatrix} \tag{38}$$

This negative stiffness term and the modal controller are converted back to physical coordinates and together form a physical-coordinate controller that can be implemented on the hardware:

$$G_C = T_S^{-1} G_M T^{-T} - \frac{1}{k_s} T_s K_{sx} T \frac{1}{k_a k_i} \tag{39}$$

The set of frequency responses for this controller are plotted in Figure 41.

4.5 Theoretical Comparisons

4.5.1 Thrust Bearing Control Designs

The theoretically predicted performance of the two thrust controllers was compared. Figure 42 depicts the compliance of both controllers. As expected, the higher bandwidth controller predicts a higher compliance peak and higher

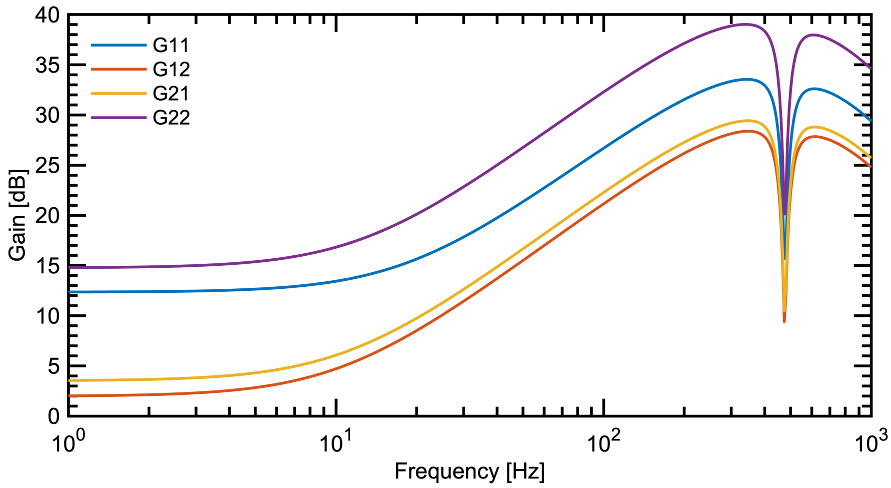

Figure 41: Modal Controller Frequency Response

frequency roll-off.

The sensitivity functions for both controllers were computed and are plotted in Figure 43. Both control designs achieve ISO Zone A stability. The lower bandwidth controller exhibits a 33% reduction in peak sensitivity.

4.5.2 Radial Bearing Control Designs

The predicted performance of the modal control design was compared to the original SISO PID controller. The theoretical compliance of each system was evaluated as the displacement measured at the DE AMB and the NDE AMB to a force applied at the test article. These results are given in Figure 44.

As expected, there is greater compliance at the NDE bearing for both controllers. The modal controller shows a 60% reduction in peak compliance compared to the SISO controller. Peak DE compliance is greater for the

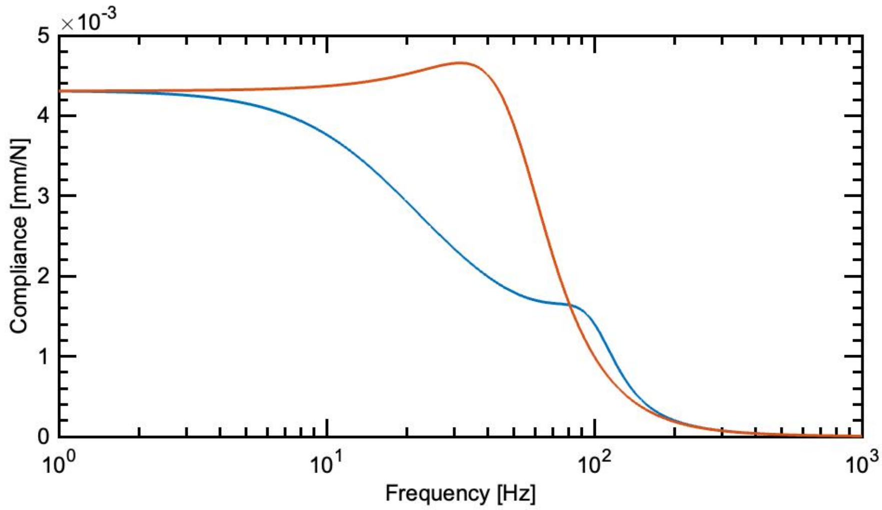

Figure 42: Thrust Controller Compliance: Low Bandwidth (Blue), High Bandwidth (Red)

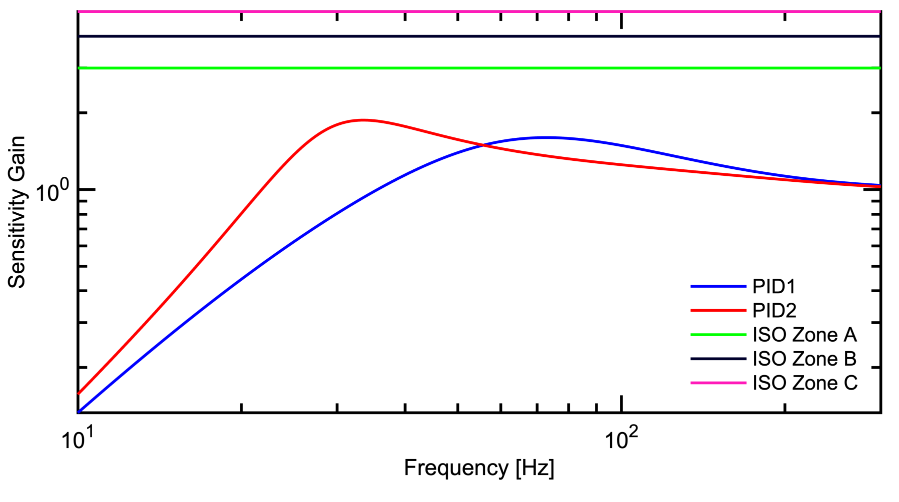

Figure 43: Thrust Controller Sensitivity: Low Bandwidth (Blue), High Bandwidth (Red)

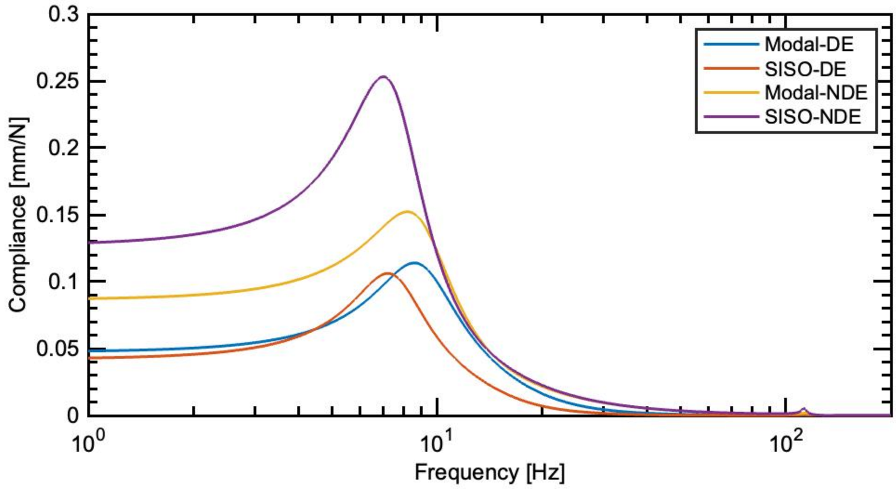

Figure 44: System Compliance Comparison

modal controller than the SISO controller. Above 100 Hz, the two designs predict very similar results.

Displacement due to unbalance force as a function of frequency was computed over the intended operating range and is plotted in Figure 45 for the SISO system and Figure 46 for modal. The maximum specified vibration level and operating frequency are included as well. Both controllers satisfy this requirement, but the modal controller predicts a significant improvement over siso control in this measure: it shows a 43% reduction in displacement at the first bending frequency.

The frequency response of the sensitivity function for the closed loop system with SISO control is depicted in Figure 47 and for modal control in Figure 48. A peak sensitivity value of 4.06 is predicted for the SISO controller, and 1.65 for modal control. The SISO controller exceeds the Zone B sensitivity limit, but the modal controller remains within specification for

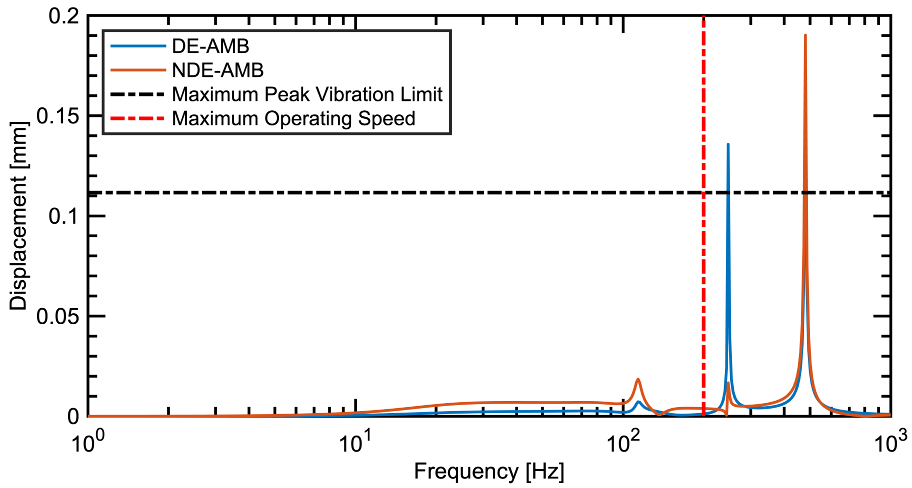

Figure 45: Unbalance Displacement: PID Controller

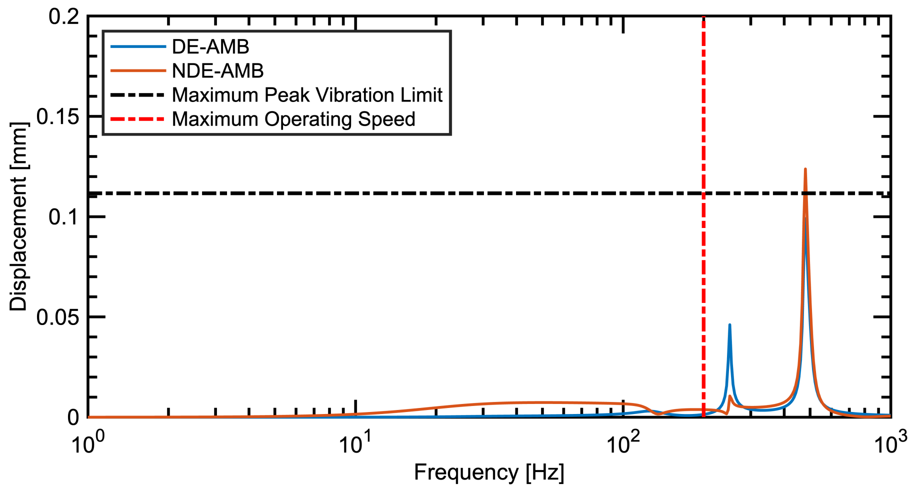

Figure 46: Unbalance Displacement: Modal Controller

all frequencies. Clearly significant stability improvements are possible with modal control.

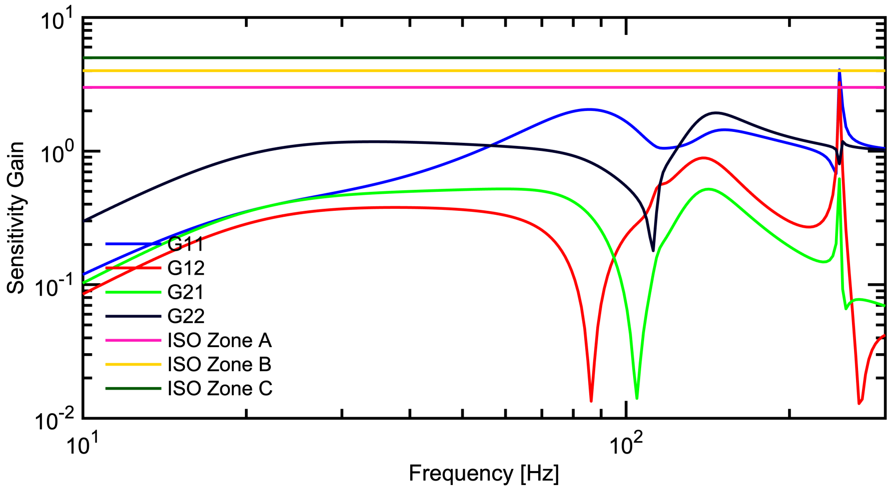

Figure 47: Closed Loop Sensitivity, PID Control

Actuator load capacity was computed over the intended operating range and is plotted in Figure 49 for the SISO system and Figure 50 for modal. The speed-dependent unbalance force is included as well for comparison. Both controllers have load capacities exceeding the unbalance force, but the modal controller shows a slight improvement over PID at the second bending frequency (10%).

4.6 Experimental Results

The control designs for both the thrust and radial axis controllers were implemented on the MicroLabBox hardware. The relevant Simulink block diagrams are reported in Appendix-D. System data was viewed in real-time with the dSpace ControlDesk software. With this set up, experimental impact

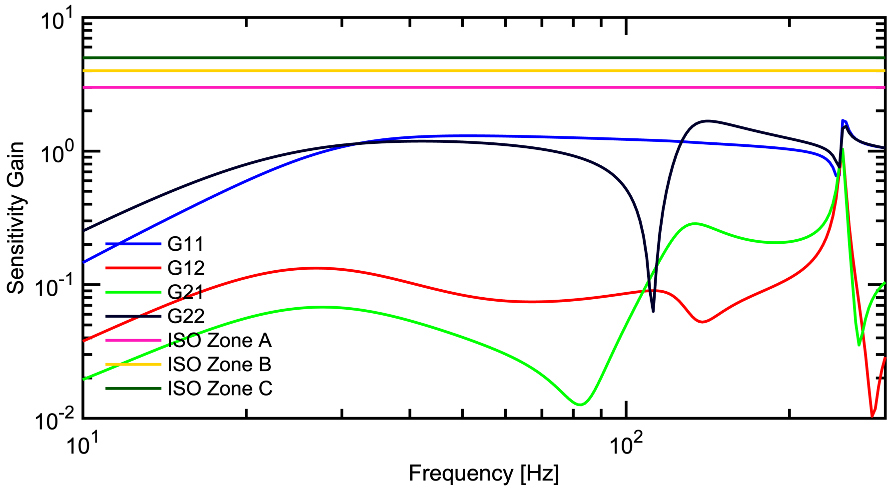

Figure 48: Closed Loop Sensitivity, Modal Control

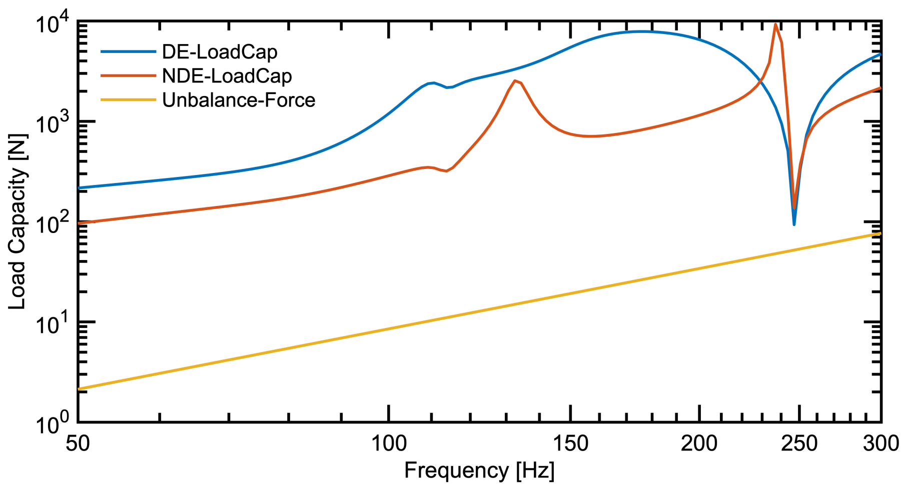

Figure 49: Load Capacity: PID Controller

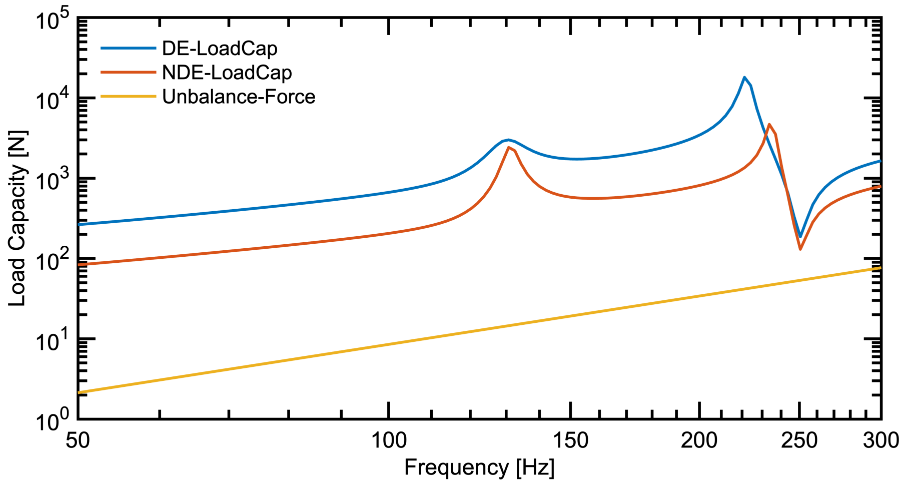

Figure 50: Load Capacity: Modal Controller

tests were conducted on the HMBTR and the results compared with the predicted compliances.

4.6.1 Thrust Bearing Experimental Compliance

Beginning with the thrust axis, the experimental compliance is plotted in figs. 51 and 52. For both controllers, the experimental compliance exceeds theoretical predictions for frequencies below 10 Hz. At higher frequencies (Above 100 Hz) the experimental compliance matches the theoretical prediction well. Between these frequencies, the experimental data matches the bandwidth roll-off predicted by theory, however there are sections where the theory over-predicts and under-predicts the experimental results.

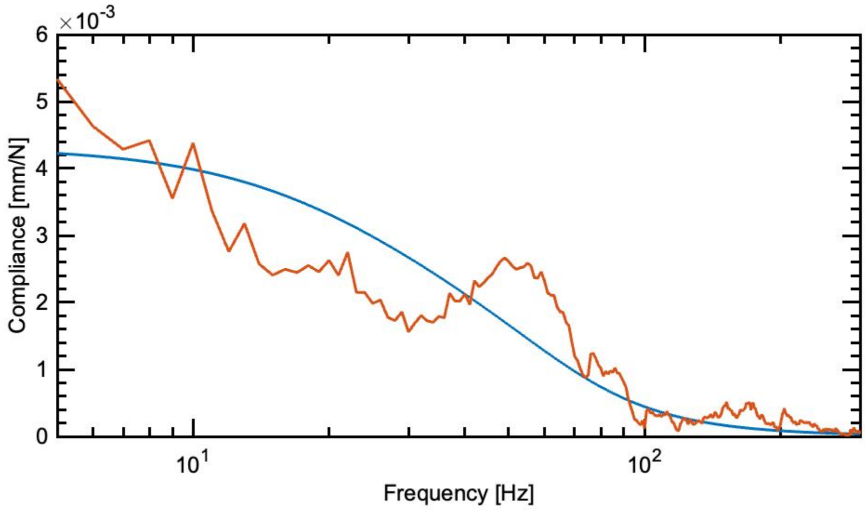

Figure 51: Thrust Axis Compliance Low Bandwidth PID: Experimental Data (Red) vs. Model (Blue)

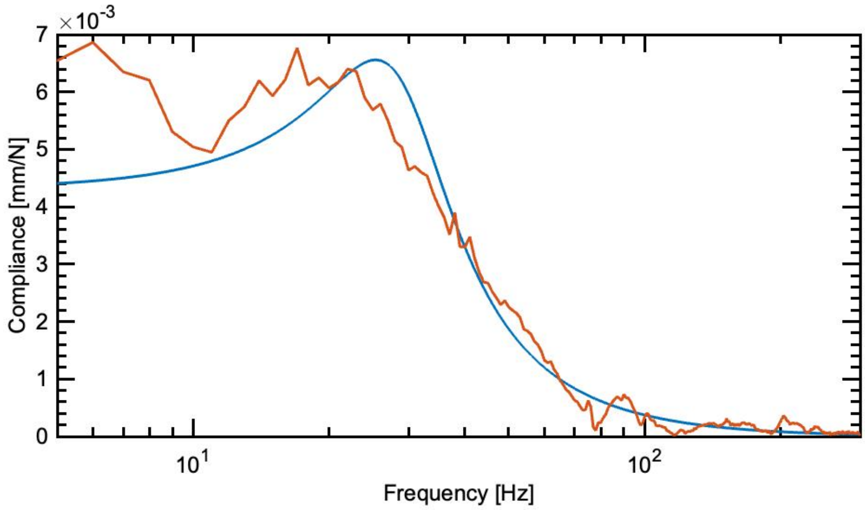

Figure 52: Thrust Axis Compliance High Bandwidth PID: Experimental Data (Red) vs. Model (Blue)

4.6.2 Radial Bearing Experimental Compliance

The experimental compliance obtained for the radial axis controllers was compared to its predicted values. The results for the SISO controller are depicted in figs. 53 and 54 and the modal controller results are depicted in figs. 55 and 56. Although there are certainly mismatches, the experimental data tracks the theory fairly well. Most importantly, the experimental results demonstrate the compliance improvements that were predicted for the modal controller over the SISO controller - a 65% decrease.

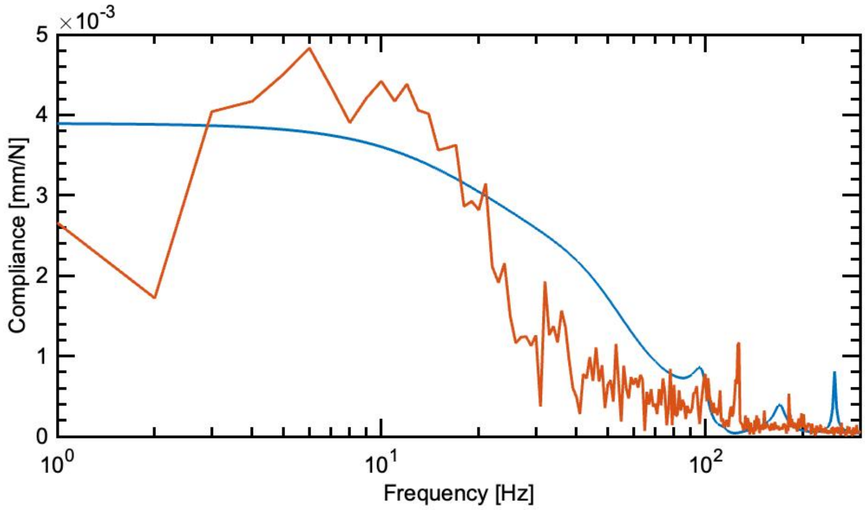

Figure 53: Radial Axis SISO PID Compliance DE: Experimental Data (Red) vs. Model (Blue)

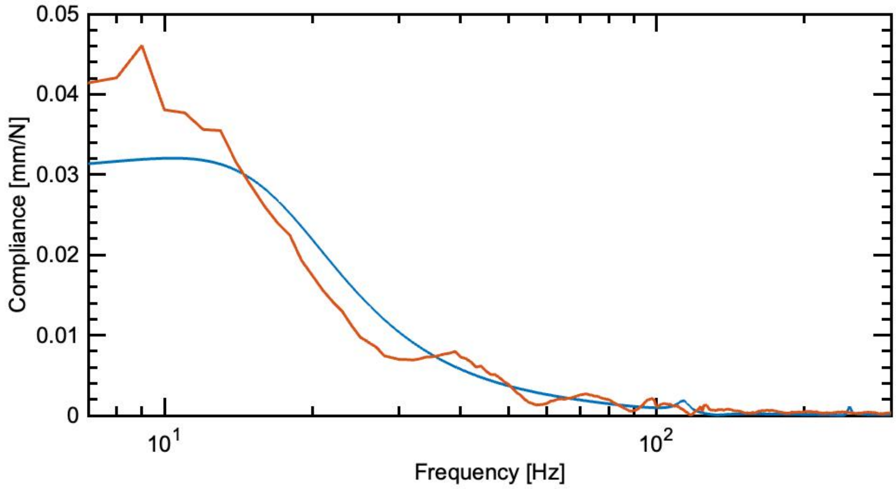

Figure 54: Radial Axis SISO PID Compliance NDE: Experimental Data (Red) vs. Model (Blue)

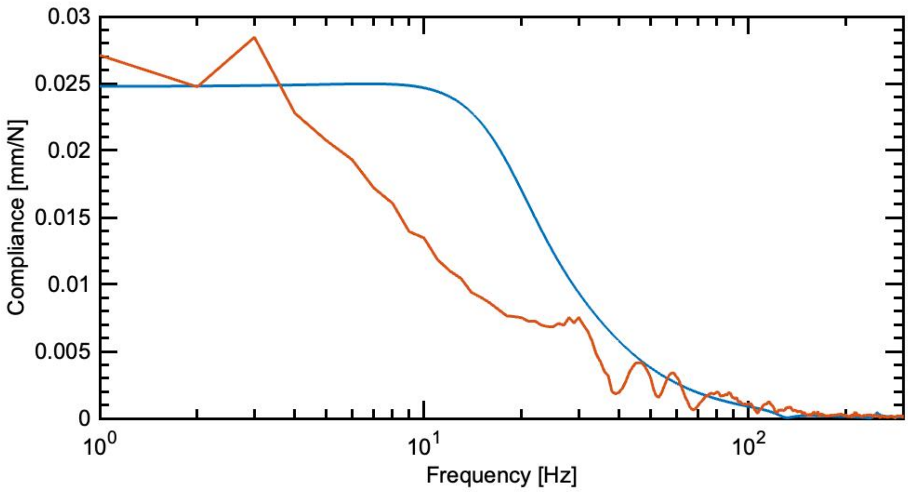

Figure 55: Radial Axis Modal PID Compliance DE: (Red) vs. Model (Blue)

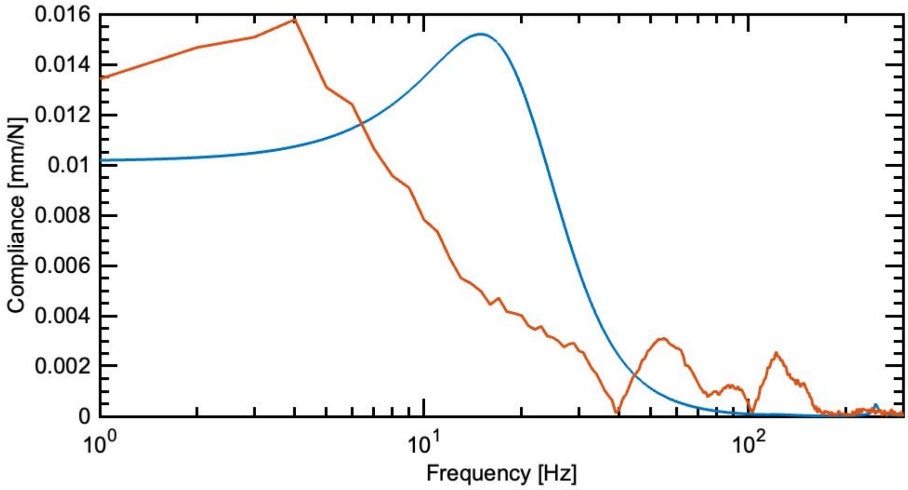

Figure 56: Radial Axis Modal PID Compliance NDE: (Red) vs. Model (Blue)

5 Conclusions and Future Work

5.1 Conclusions

This thesis has presented the mechanical design work undertaken for the buildup of the HMBTR. System requirements were given and a design was developed to meet these requirements. The test rig was assembled and the rotor levitated. A mathematical model for the system was constructed and validated experimentally. Two control designs were synthesized and implemented on the hardware: independent-axis SISO PID control and Modal PID control. The performance of these controllers was predicted and measured experimentally. Several general conclusions can be drawn:

- Experimental data correlated well enough with the theoretical prediction to complete an initial control design. However, additional examination will be necessary to identify a low-frequency substructure resonance observed in the frequency response data.

- Significant performance and stability gains were predicted and realized with modal control. A 70% reduction in unbalance response at the first critical frequency was predicted. 30% low frequency and 15% first bending mode compliance improvements were measured.

- Further controller stability and performance optimization is certainly possible, but a few difficulties hindered the control design process. Increased sampling rates and higher anti-aliasing filter cut-off frequencies would allow for higher control gains and performance improvements. However, cut-off frequencies and derivative gains had to be set fairly low in order to fully attenuate electrical noise. The relatively low frequency first bending mode constrained the control effort as well. An accurate system model certainly helps in choosing controller parameters to optimally balance these constraints.

5.2 Future Work

This thesis documents the design and modeling of the HMBTR. However, just the beginnings of its development were presented. A major next step is the installation and alignment of the drive coupling and spin-up to operating speed. The unbalance analysis and experimental compliance measurements conducted for the modal control design indicate that it can support the rig through the first critical speed. Closed-loop frequency response data can then be taken with the coupling attached and used to establish a coupling model with stiffness and damping values such that the closed loop model matches the experimental data. Then, a new control design can be implemented and at-speed testing conducted.

References

[1] Parinya Anantachaisilp. Pid tuning methods for active magnetic bearing systems. Master's thesis, UVA, 2011.

[2] Karl Astrom. *Control System Design*, chapter 5, pages 177–215. 2002.

[3] Daniel Baun. *Hydrodynamic Forces in Centrifugal Pump and Compressor Impellers in Volute Casings: Measurements using Magnetic Bearings and CFD Simulations*. PhD thesis, University of Virginia, 2002.

[4] Richard Carter Benson. The dynamical response of an overhung, unbalance, skewed rotor on two flexible supports. Master's thesis, University of Virginia, 1974.

[5] Jawad Chaudhry. Rotor dynamic analysis in matlab framework. Master's thesis, UVA, September 2008.

[6] T. Dimond, P. Allaire, S. Mushi, Z. Lin, and S. Yoon. Modal tilt/translate control and stability of a rigid rotor on active magnetic bearings. *International Journal of Rotating Machinery*, 2012.

[7] Conrad GAHLER, Manuel MOHLER, and Raoul HERZOG. Multivariable identification of active magnetic bearing systems. *JSME INTERNATIONAL JOURNAL SERIES*, 40(4):583–584, 1997.

[8] Mechanical Vibration – Vibration of rotating machinery equipped with active magnetic bearings. Standard, International Organization for Standardization, Geneva, CH, March 2012.

[9] H. H. Jeffcott. The Lateral Vibration Loaded Shafts in the Neighborhood of a Whirling Speed. - The Effect of Want of Balance. *Philosophical Magazine*, 1919.

[10] R.D. Kelm. *Analysis and Testing of a Magnetic Bearing for Flexible Rotors*. PhD thesis, University of Virginia, 1986.

[11] René Larsonneur. *Magnetic Bearings: Theory, Design, and Application to Rotating Machinery*, chapter 2, pages 27–68. Springer-Verlag Berlin Heidelberg, 2009.

[12] René Larsonneur. *Magnetic Bearings: Theory, Design, and Application to Rotating Machinery*, chapter 8, pages 191–224. Springer-Verlag Berlin Heidelberg, 2009.

[13] D.F. Li and E.J. Gunter. Undamped critical speed analysis of dual-level rotors including lateral, axial and torsional vibration coordinates - a manual for computer programs crtsp2a and crtsp2t. Report 103, UVA ROMAC, June 1979.

[14] D.F. Li, E.J. Gunter, L.E. Barrett, and P.E. Allaire. The dynamic analysis of multi-level flexible rotor-bearing systems using transfer matrices and component mode synthesis. Report 149, UVA ROMAC, February 1981.

[15] Eric Maslen. Magnetic Bearings. Technical report, James Madison University Department of Integrated Science and Technology, September 2014.

[16] Eric Maslen, Christopher Sortore, and David Meeker. Analysis software for magnetic bearing audits. Report 406, UVA ROMAC, November 2000.

[17] R. Ruhl. *Dynamics of Distributed Parameter Rotor Systems: Transfer Matrix and Finite Element Tech- niques*. PhD thesis, Cornell University, 1970.

[18] Peter W Thomas. *Active Magnetic Control of Axial Shaft Vibrations*. PhD thesis, University of Virginia, 1986.

[19] Zackary W. Whitlow. Modeling and control of non-laminated active magnetic thrust bearings. Master's thesis, UVA, December 2014.

[20] Walter Lawren Wilson. *Optimum Bearing Characteristics for an Overhung Rotor System*. PhD thesis, University of Virginia, 1982.

A Test Rig Physical Design Parameters

Credit goes to Robert Rockwell for completing the majority of the mechanical design work for the HMBTR. He drafted CAD models of the complete rig, giving a full picture of its geometric properties as well as facilitating assembly planning.

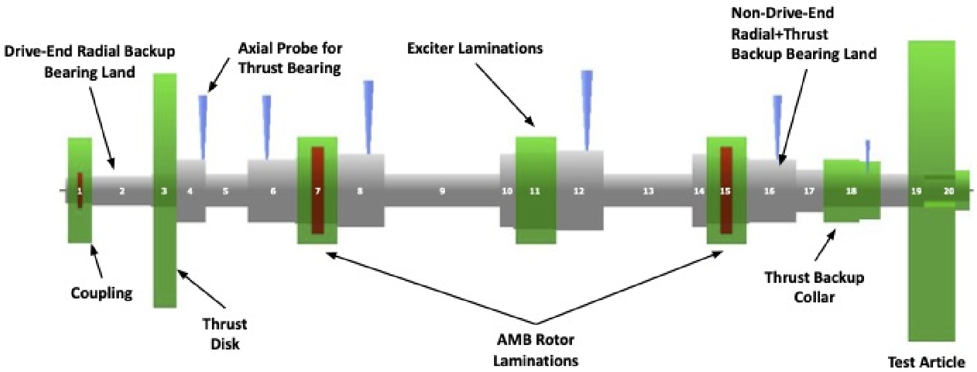

Figure 57: Rotor Mechanical Design, 2D View

Section	Length in	OD in	Section	Length in	OD in
1	0.55	0.3937	11	0.9	1.15
2	1.25	0.444	12	1	1.2
3	0.55	0.5	13	1.88	0.5
4	0.6	0.95	14	0.3	1.1
5	0.9	0.5	15	0.9	1
6	1	0.95	16	1	0.95
7	0.9	1	17	0.580	0.64
8	1	1.1	18	1.78	0.5
9	2.42	0.5	19	0.35	0.4724
10	0.3	1.1	20	0.965	0.3149

Table 13: Rotor Section Length and Diameter Parameters

	Gap Size in	Total Length in	Power Loss W	ft-lb/s	Hp	Torque Nm	oz-in
Laminations	radial: 0.03	3 x 0.070	1.1162	0.8232	0.0015	0.0007	0.1006
Shaft (0.5 in. OD)	radial: 1.0	6.572	0.0187	0.0138	0.0000	0.0000	0.0017
Shaft (0.75 in. OD)	radial: 1.0	2.108	0.0279	0.0206	0.0000	0.0000	0.0025
Shaft (1.05 in. OD)	radial: 1.0	5.208	0.2468	0.1820	0.0003	0.0002	0.0223
Coupling	axial: 0.05	0.512	1.6961	1.2509	0.0023	0.0011	0.1529
Thrust Disk	axial: 0.03	0.500	17.3044	12.7631	0.0232	0.0110	1.5600
Test Article	axial: 0.85	1.000	28.0636	20.6986	0.0376	0.0179	2.5300
Total		18.000	48.4737	35.7523	0.0650	0.0309	4.3700

Table 14: Windage Calculations

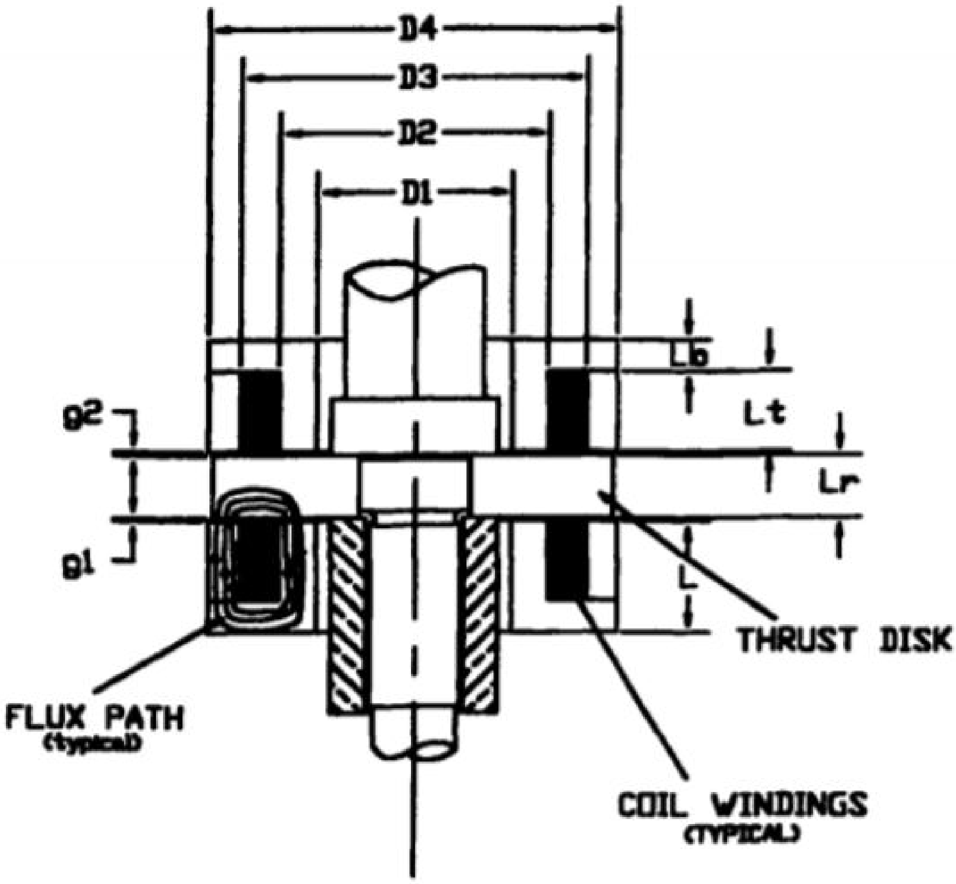

Figure 58: Thrust Actuator, from Baun [3]

Air Gap	g_0	0.03 in
Rotor Inner Diameter	D_1	1.75 in
Coil Inner Diameter	D_2	2.4 in
Coil Outer Diameter	D_3	3.09 in
Actuator Outer Diameter	D_4	3.5 in
Back Iron Length	L_b	0.28 in
Stator Length	L_t	0.76 in
Thrust Collar Length	L_r	0.56 in
Mean Magnetic Path Length	L_m	3.3 in

Table 15: Thrust Actuator Dimensions

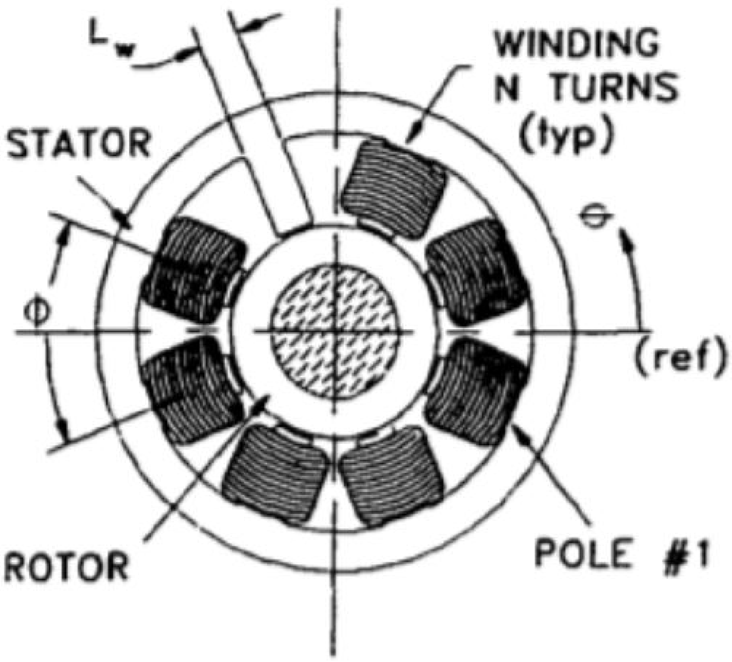

Figure 59: Radial Actuator Cross-Section, from Baun [3]

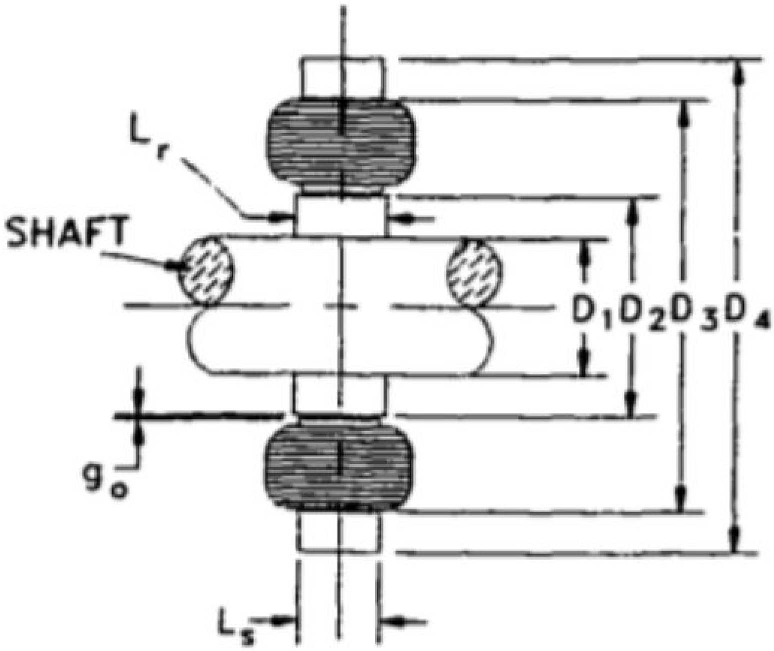

Figure 60: Radial Actuator Side View, from Baun [3]

Radial Air Gap	g_0	0.03 in
Rotor Inner Diameter	D_1	1.0 in
Rotor Outer Diameter	D_2	1.599 in
Stator Back Iron Inner Diameter	D_3	2.993 in
Stator Back Iron Outer Diameter	D_4	3.595 in
Stator Length	L_s	0.616 in
Rotor Length	L_r	0.70 in
Leg Width	L_w	0.30 in

Table 16: Radial Actuator Dimensions

B Rotor Model Matrices

$$A = \begin{bmatrix} 0.0 & 0.0 & 0.0 & 0.0 & 0.0 & 1.0 & 0.0 & 0.0 & 0.0 & 0.0 \\ 0.0 & 0.0 & 0.0 & 0.0 & 0.0 & 0.0 & 1.0 & 0.0 & 0.0 & 0.0 \\ 0.0 & 0.0 & 0.0 & 0.0 & 0.0 & 0.0 & 0.0 & 1.0 & 0.0 & 0.0 \\ 0.0 & 0.0 & 0.0 & 0.0 & 0.0 & 0.0 & 0.0 & 0.0 & 1.0 & 0.0 \\ 0.0 & 0.0 & 0.0 & 0.0 & 0.0 & 0.0 & 0.0 & 0.0 & 0.0 & 1.0 \\ 0.0 & 0.0 & 0.0 & 0.0 & 0.0 & 0.0 & 0.0 & 0.0 & 0.0 & 0.0 \\ 0.0 & 0.0 & 0.0 & 0.0 & 0.0 & 0.0 & 0.0 & 0.0 & 0.0 & 0.0 \\ 0.0 & 0.0 & -4.9e5 & 0.0 & 0.0 & 0.0 & 0.0 & -14.1 & 0.0 & 0.0 \\ 0.0 & 0.0 & 0.0 & -2.4e6 & 0.0 & 0.0 & 0.0 & 0.0 & -30.7 & 0.0 \\ 0.0 & 0.0 & 0.0 & 0.0 & -9.0e6 & 0.0 & 0.0 & 0.0 & 0.0 & -60.1 \end{bmatrix}.$$

$$B = \begin{bmatrix} 0.0 & 0.0 \\ 0.0 & 0.0 \\ 0.0 & 0.0 \\ 0.0 & 0.0 \\ 0.0 & 0.0 \\ 6.4 & 6.4 \\ -6.9 & 1.4 \\ -3.3 & -8.0 \\ -5.4 & 1.0 \\ -9.0 & 11.2 \end{bmatrix}.$$

$$C = \begin{bmatrix} 6.4 & -7.9 & -0.6 & -3.5 & -8.5 & 0.0 & 0.0 & 0.0 & 0.0 & 0.0 \\ 6.4 & -6.9 & -3.3 & -5.4 & -9.0 & 0.0 & 0.0 & 0.0 & 0.0 & 0.0 \\ 6.4 & 1.4 & -8.0 & 1.0 & 11.2 & 0.0 & 0.0 & 0.0 & 0.0 & 0.0 \\ 6.4 & 2.3 & -6.1 & 2.7 & 8.3 & 0.0 & 0.0 & 0.0 & 0.0 & 0.0 \end{bmatrix}.$$

$$G = \begin{bmatrix} 0.0 & 0.0 & 0.0 & 0.0 & 0.0 & 0.0 & 0.0 & 0.0 & 0.0 & 0.0 \\ 0.0 & 0.0 & 0.0 & 0.0 & 0.0 & 0.0 & 0.0 & 0.0 & 0.0 & 0.0 \\ 0.0 & 0.0 & 0.0 & 0.0 & 0.0 & 0.0 & 0.0 & 0.0 & 0.0 & 0.0 \\ 0.0 & 0.0 & 0.0 & 0.0 & 0.0 & 0.0 & 0.0 & 0.0 & 0.0 & 0.0 \\ 0.0 & 0.0 & 0.0 & 0.0 & 0.0 & 0.0 & 0.0 & 0.0 & 0.0 & 0.0 \\ 0.0 & 0.0 & 0.0 & 0.0 & 0.0 & 0.0 & 0.0 & 0.0 & 0.0 & 0.0 \\ 0.0 & 0.0 & 0.0 & 0.0 & 0.0 & 0.0 & 0.0 & 0.1 & -0.2 & 0.0 \\ 0.0 & 0.0 & 0.0 & 0.0 & 0.0 & 0.0 & 0.1 & 0.4 & -0.6 & 0.3 \\ 0.0 & 0.0 & 0.0 & 0.0 & 0.0 & 0.0 & -0.2 & -0.6 & 1.3 & -0.3 \\ 0.0 & 0.0 & 0.0 & 0.0 & 0.0 & 0.0 & 0.0 & 0.3 & -0.3 & 0.4 \end{bmatrix}.$$

C Rotor Identification Plots

C.1 Bare Rotor

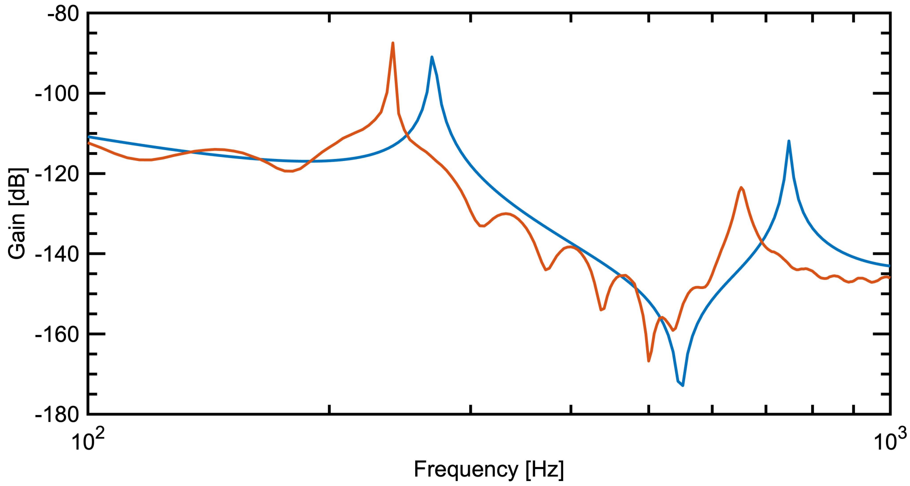

Figure 61: Input A to Output C: Experimental Data (Red) vs. Model (Blue)

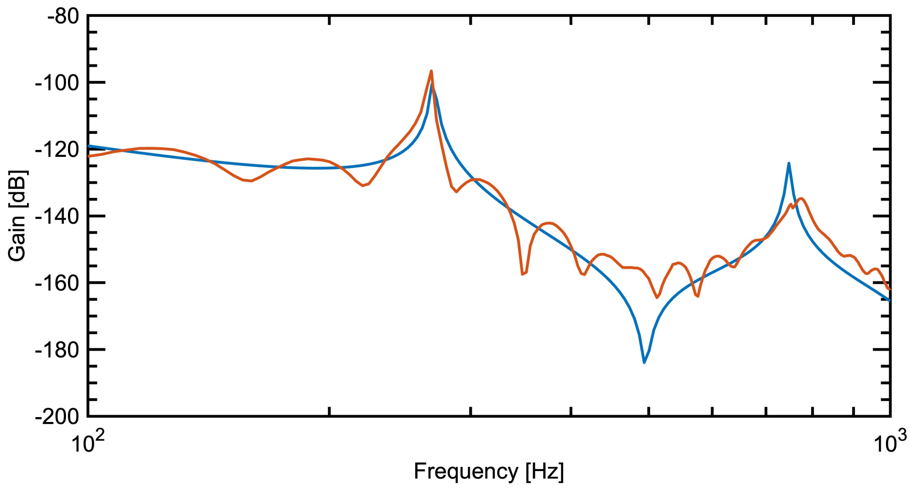

Figure 62: Input A to Output B: Experimental Data (Red) vs. Model (Blue)

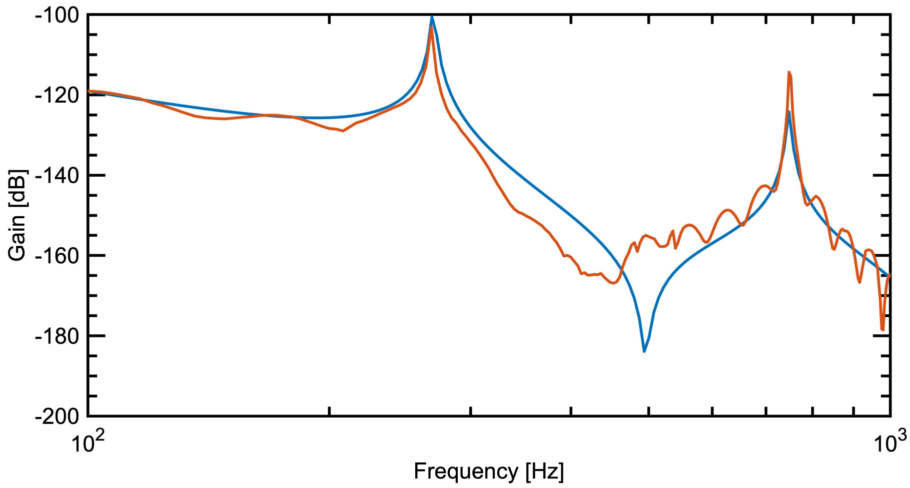

Figure 63: Input B to Output A: Experimental Data (Red) vs. Model (Blue)

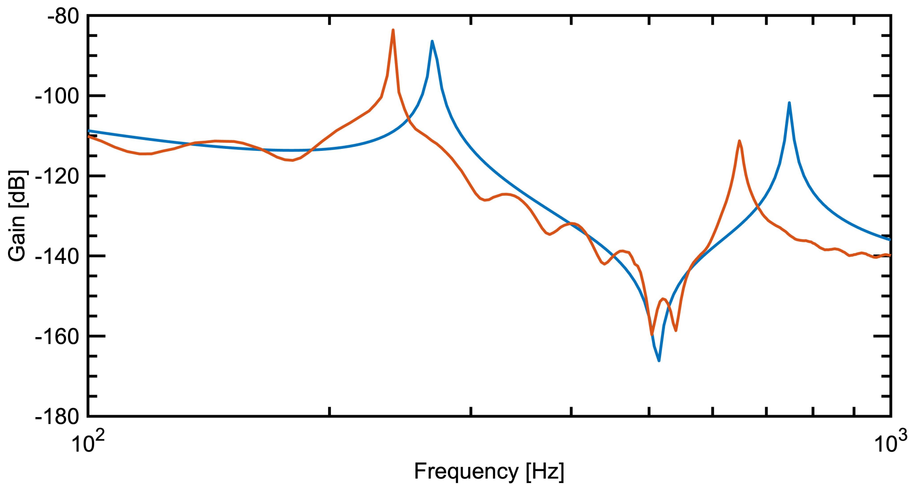

Figure 64: Input B to Output C: Experimental Data (Red) vs. Model (Blue)

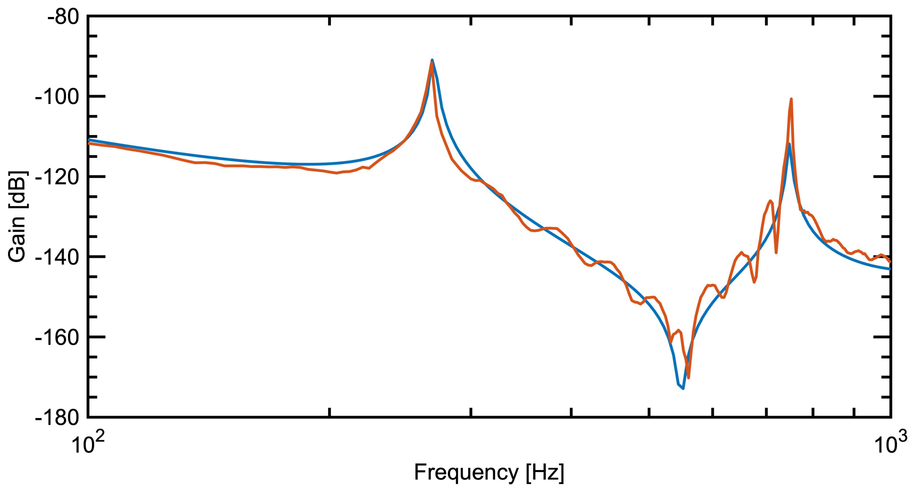

Figure 65: Input C to Output A: Experimental Data (Red) vs. Model (Blue)

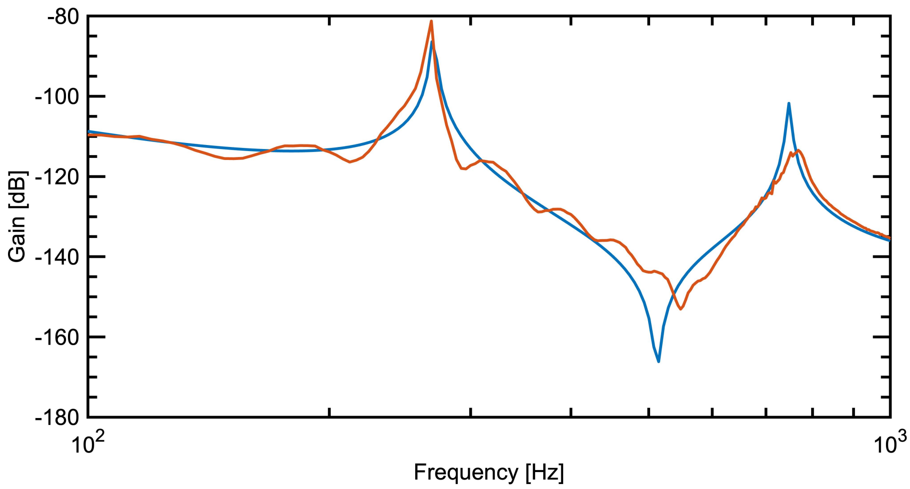

Figure 66: Input C to Output B: Experimental Data (Red) vs. Model (Blue)

C.2 Full Rotor - Soft Tip Impact Hammer

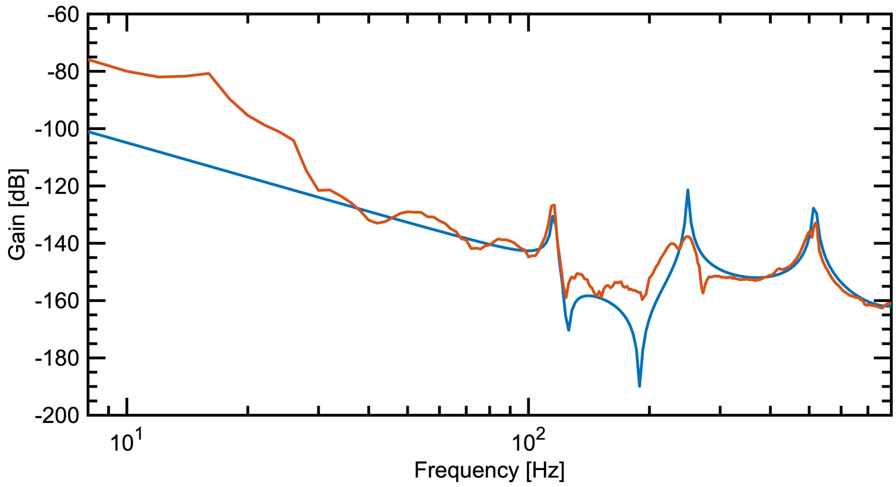

Figure 67: Input A to Output C: Experimental Data (Red) vs. Model (Blue)

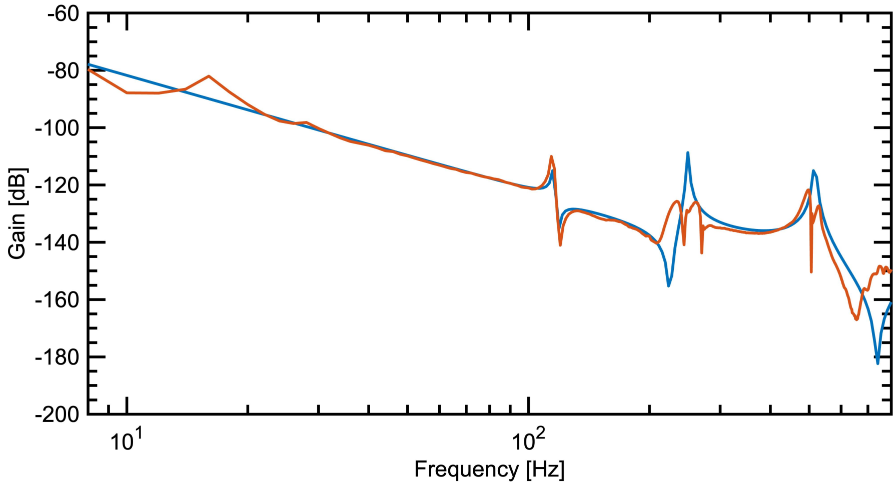

Figure 68: Input A to Output B: Experimental Data (Red) vs. Model (Blue)

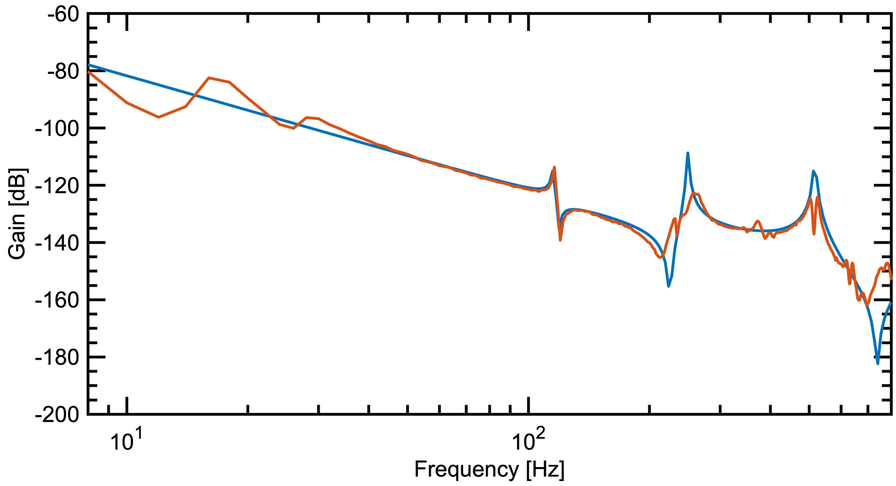

Figure 69: Input B to Output A: Experimental Data (Red) vs. Model (Blue)

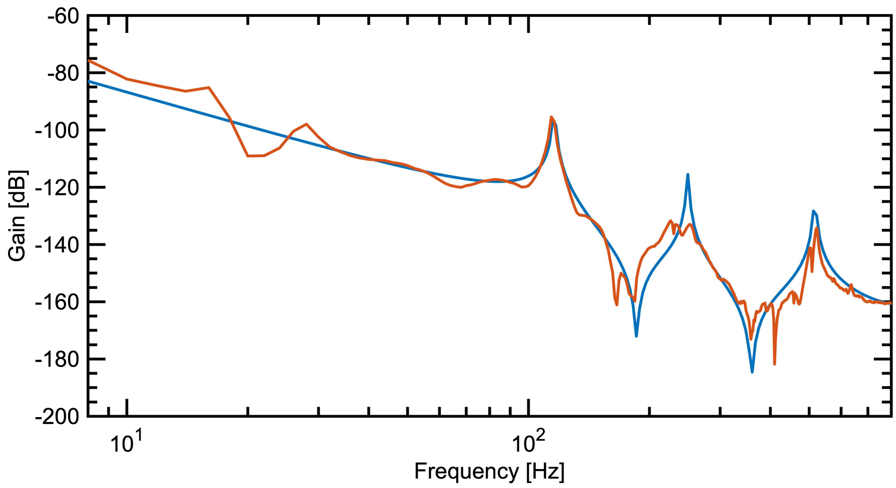

Figure 70: Input B to Output C: Experimental Data (Red) vs. Model (Blue)

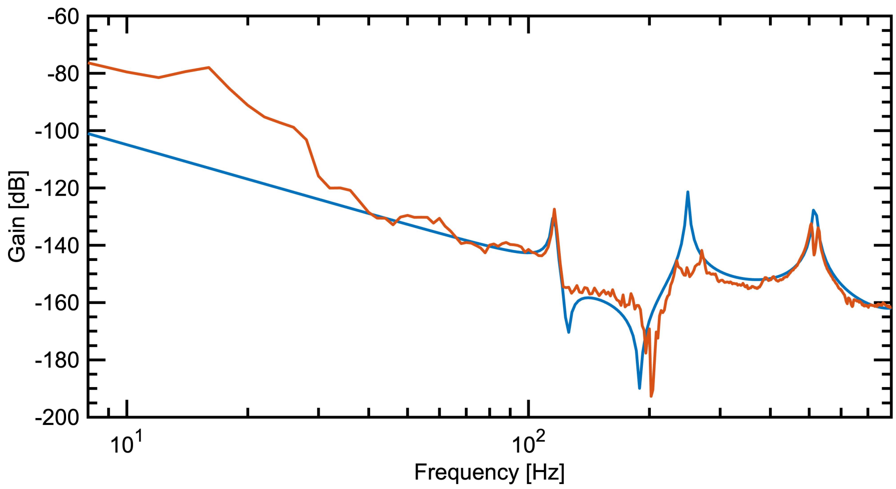

Figure 71: Input C to Output A: Experimental Data (Red) vs. Model (Blue)

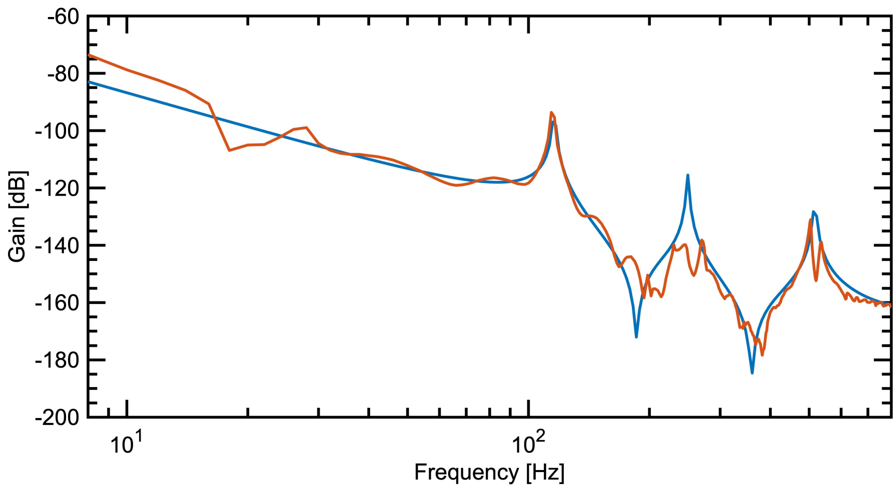

Figure 72: Input C to Output B: Experimental Data (Red) vs. Model (Blue)

D Simulink Models

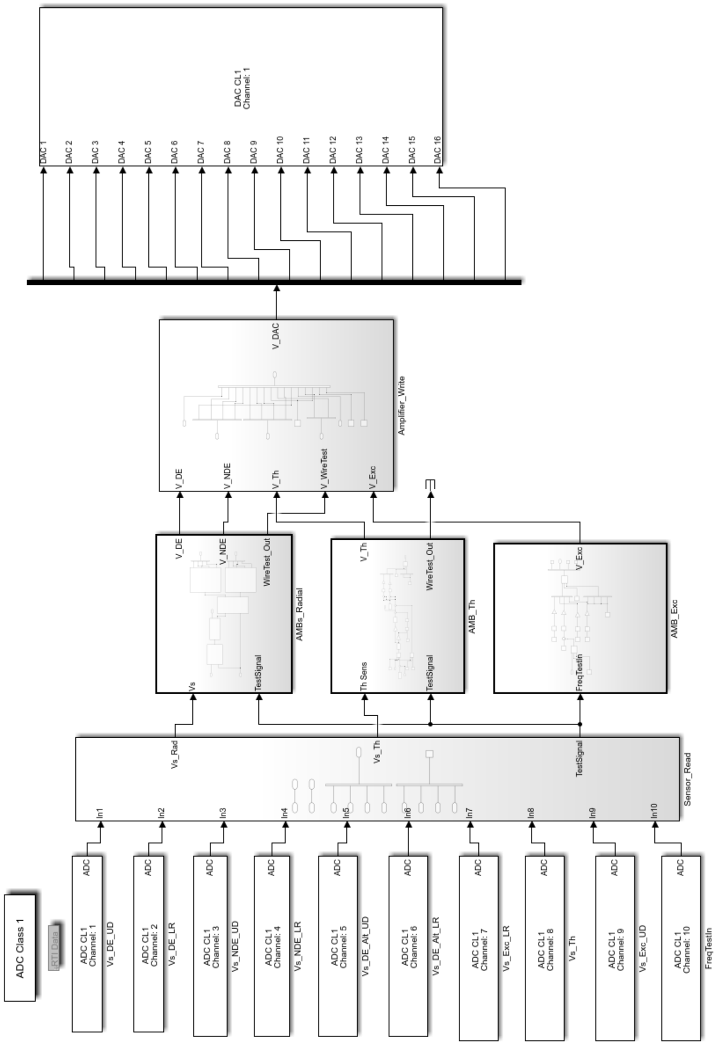

Figure 73: Top-Level Model

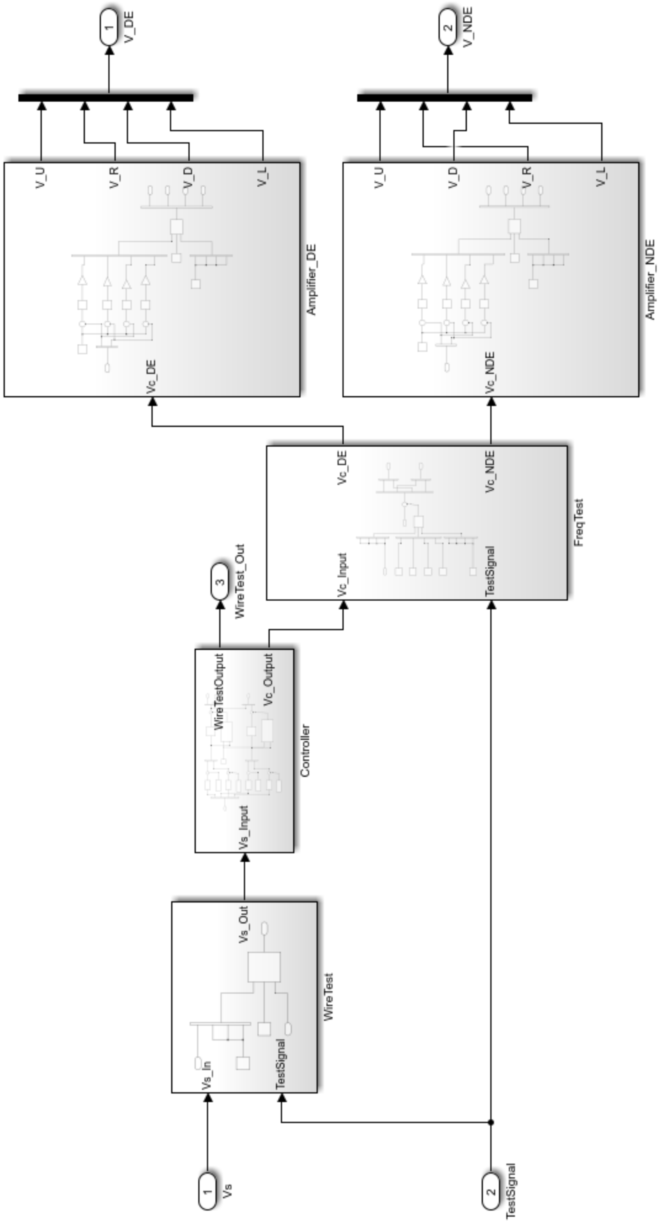

Figure 74: Radial Subsystem

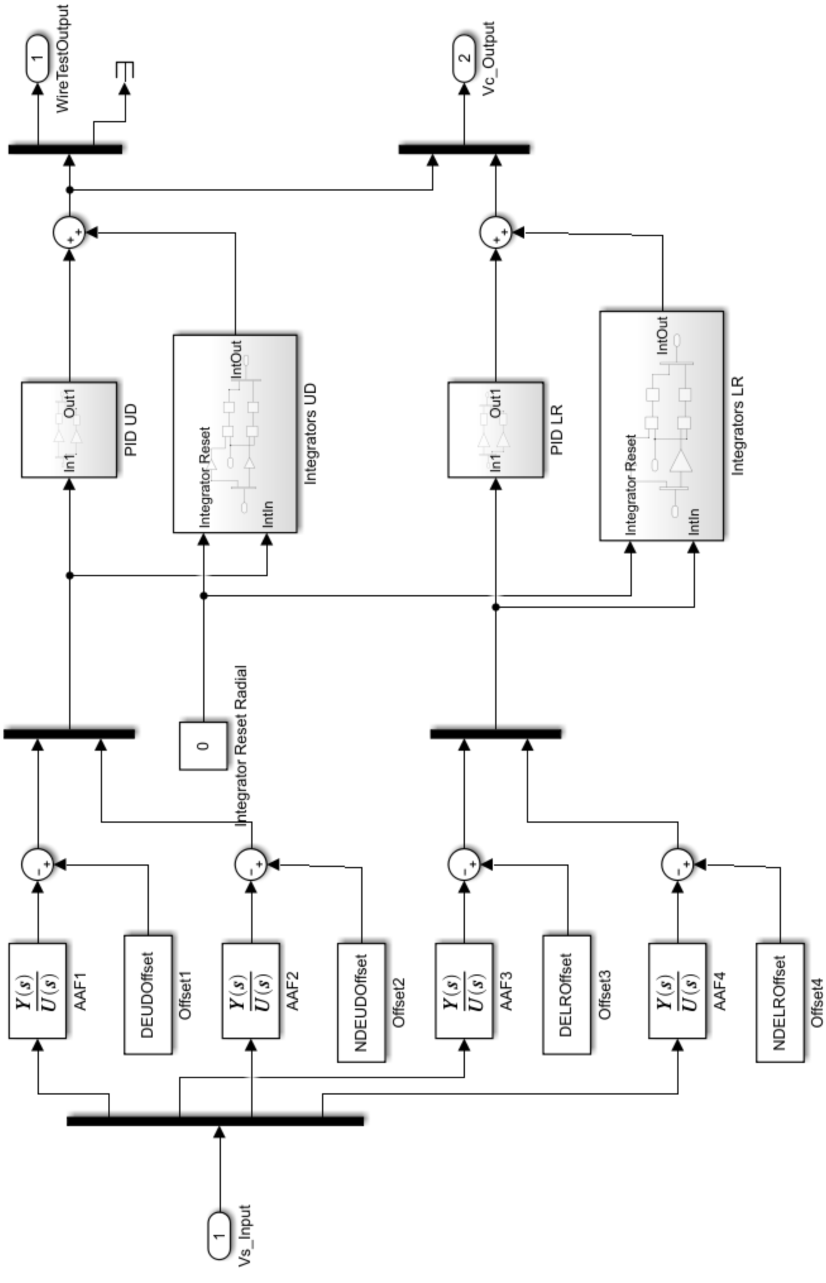

Figure 75: Controller Subsystem

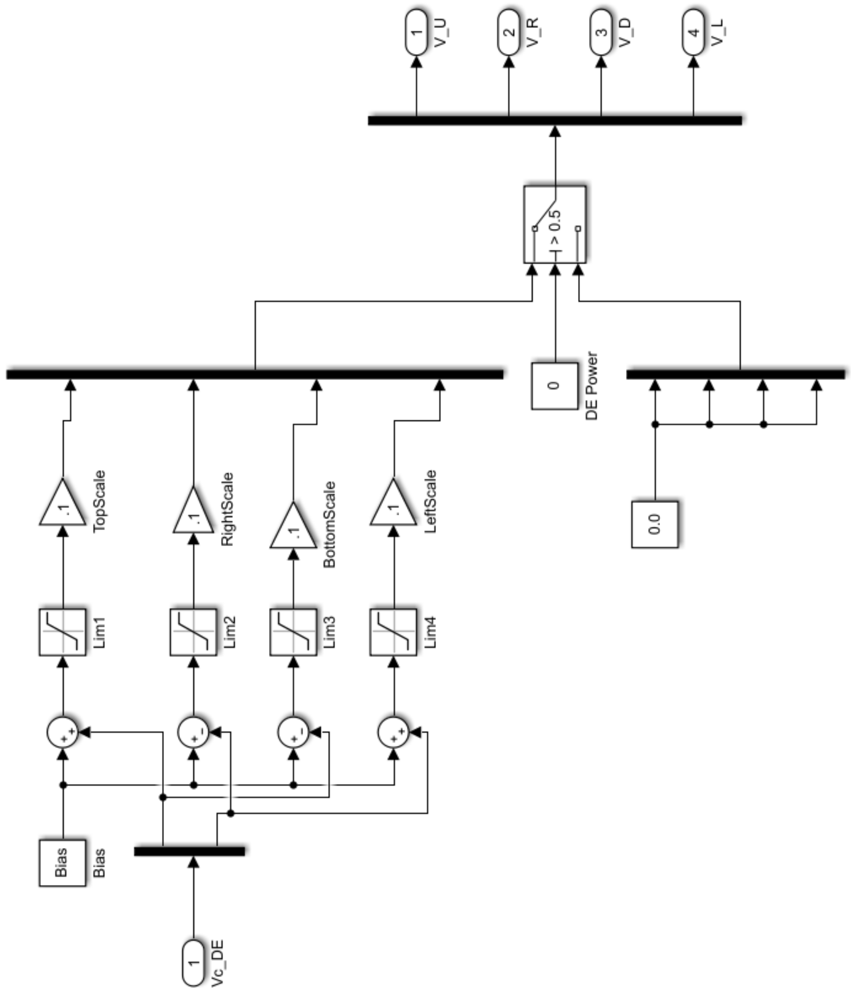

Figure 76: Amplifier Subsystem

E Hardware Datasheets

SIZE CONSTANTS ****			
PARAMETERS	SYMBOL	UNIT	VALUE
MAXIMUM RATED TORQUE *TEMPERATURE RISE 105°	Tr	IN-OZ N_M	177 1.25
MAXIMUM CONTINUOUS STALL TORQUE *TEMPERATURE RISE 105°	Tc	IN-OZ N_M	48 0.34
MAXIMUM CONTINUOUS OUTPUT POWER * TEMPERATURE RISE 105°	Pout Smpa	WATTS RPM	384 16,180
MOTOR CONSTANT	KM	IN-OZ/$\sqrt{W}$ N_M/ $\sqrt{W}$	8.78 0.06
ELECTRICAL TIME CONSTANT	Te	msec	3.36
MECHANICAL TIME CONSTANT	Tm	msec	14.72
THERMAL TIME CONSTANT	Tth	minutes	17
THERMAL RESISTANCE *	TPR	°C/WATTS	2.18
MAXIMUM COGGING TORQUE	Tf	IN-OZ N_M	0.89 0.01
VISCOUS DAMPING (INFINITE SOURCE IMPEDANCE)	Fl	IN-OZ/RPM N_M/RPM	8.0E-05 5.6E-07
HISTERESIS DRAG TORQUE	Th	IN-OZ N_M	0.47 0.003
ROTOR INERTIA FRAMELESS	Jm	IN-OZ-SEC^2 Kg.m^2	7.1E-03 5.0E-05
MOTOR WEIGHT FRAMELESS	Wt	OZ Kg	24 .69
ROTOR INERTIA HOUSED	Jm	IN-OZ-SEC^2 Kg.m^2	7.2E-03 5.1E-05
MOTOR WEIGHT HOUSED (ESTIMATED)	Wt	OZ Kg	38 1.09
NO. OF POLES		P	4
* TPR ASSUMES MOTOR MOUNTED TO ALUMINUM HEAT SINK 203.2 X 203.2 X 6.35 mm (STILL AIR) ** AMBIENT TEMPERATURE 20°C			
WINDING CONSTANTS *			
PARAMETERS	SYMBOL	UNIT	VALUE
DESIGN VOLTAGE	Vp	VOLT	24
PEAK TORQUE ±25%	Tp	IN-OZ Nm	177 1.25
PEAK CURRENT ±25%	Ip	AMPS LIMIT	92
TORQUE SENSITIVITY, ±10%	Kt	IN-OZ/AMP Nm/AMP	1.94 0.014
NO LOAD SPEED ±15%	Snl	RPM RAD/SEC	16,707 1,750
VOLTAGE CONSTANT, ±10%	Kb	V/KRPM V/RAD/SEC	1.43 0.014
TERMINAL RESISTANCE, ±12%	Rm	OHMS	0.054
TERMINAL INDUCTANCE, ±30%	Lm	mH	0.18
* PERFORMANCE * 20°C			

Figure 77: Motor: MOOG BN34HS, Derived Parameters

BN34HS SPECIFICATIONS -

Continuous Stall Torque 48 - 99 oz-in (0.3390 - 0.6991 Nm)
Peak Torque 177 - 363 oz-in (1.2499 - 2.5633 Nm)

Part Number*		BN34HS-25AF-□□ T F O			BN34HS-35AF-□□ T F O		
Winding Code**		01	02	03	01	02	03
L = Length	inches	2.50			3.50		
	millimeters	63.5			88.9		
Terminal Voltage	volts DC	24.0	50.0	100.0	24.0	50.0	100.0
Peak Torque	oz-in	177.0	177.0	177.0	363.0	363.0	363.0
	Nm	1.2499	1.2499	1.2499	2.5633	2.5633	2.5633
Continuous Stall Torque	oz-in	48.0	49.0	48.0	91.0	98.0	99.0
	Nm	0.3390	0.3460	0.3390	0.6426	0.6920	0.6991
Rated Speed	RPM	14011.0	13900.0	14640.0	7100.0	9340.0	9400.0
	rad/sec	1467	1456	1533	744	978	984
Rated Torque	oz-in	34.0	34.0	34.0	78.0	78.0	78.0
	Nm	0.2401	0.2401	0.2401	0.5508	0.5508	0.5508
Rated Current	Amps	18.60	8.60	4.50	22.40	13.00	6.50
Rated Power	watts	396.0	381.0	397.0	478.0	591.0	591.0
Torque Sensitivity	oz-in/amp	1.94	4.20	8.08	3.59	6.21	12.42
	Nm/amp	0.0137	0.0297	0.0571	0.0254	0.0439	0.0877
Back EMF	volts/KRPM	1.43	3.10	5.97	2.66	4.59	9.18
	volts/rad/sec	0.0137	0.0297	0.0571	0.0254	0.0439	0.0877
Terminal Resistance	ohms	0.054	0.242	0.920	0.063	0.163	0.638
Terminal Inductance	mH	0.18	0.85	3.14	0.33	0.99	3.95
Motor Constant	oz-in/sq.rt.watts	8.35	8.54	8.42	14.30	15.38	15.55
	Nm/sq.rt.watts	0.05895	0.06029	0.05949	0.10100	0.10862	0.10980
Rotor Inertia	oz-in-sec^2x10^{-3}	7.30	7.30	7.30	14.00	14.00	14.00
	g-cm^2	515.2	515.2	515.2	988.0	988.0	988.0
Weight	oz	38.0	38.0	38.0	65.0	66.0	66.0
	g	1079.2	1079.2	1079.2	1846.0	1874.4	1874.4
# of Poles		4.0	4.0	4.0	4.0	4.0	4.0
Timing		120°	120°	120°	120°	120°	120°
Mech. Time Constant	ms	14.8	14.2	14.6	9.7	8.4	8.2
Electrical Time Constant	ms	3.33	3.51	3.41	5.24	6.07	6.19
Thermal Resistivity	deg. C/watt	1.1	1.3	1.3	0.8	0.9	1.0
Speed/Torque Gradient	rpm/oz-in	58.5	55.8	57.3	19.8	17.1	16.8

Notes:
1. Motor mounted to a 4 x 4 x 1/4 inches aluminum plate, still air.
2. Maximum winding temperature of 155°C.
3. Typical electrical specifications at 25°C.
4. Motor Terminal Voltages are representative only; motors may be operated at voltages other than those listed in the table. For assistance please contact an applications engineer.
5. For MS (military style) connector, please specify connector housing and terminal.
6. Data for informational purposes only. Should not be considered a binding performance agreement. For specific applications, please contact the factory.

*Many other custom mechanical options are available – consult factory.
**Many other winding options are available – consult factory.

Select your options below and place their code in its corresponding block as shown on page 49.

T TERMINATION
L – Leads (std)
C – Connector
M – MS Connector

F FEEDBACK OPTIONS
H – Hall Effect (std)
R – Resolver
S – Sensorless

O OTHER OPTIONS
D – Drive
E – Encoder
G – Gearhead

Figure 78: Motor: Moog BN34HS, Physical Parameters

GENERAL SPECIFICATIONS

Test conditions: Load = 1mH in series with 1 Ω. Ambient temperature = 25 °C. +HV = HV_{max}

MODEL	JSP-090-10	JSP-090-20	JSP-180-10	JSP-180-20	JSP-180-30	
OUTPUT POWER						
Peak Current	10	20	10	20	30	Adc
Peak time	1	1	1	1	1	s
Continuous current	5	10	5	10	15	Adc
Peak Output Power	0.85	1.64	1.73	3.41	5.12	kW
Continuous Output Power	0.43	0.85	0.87	1.73	2.56	kW
INPUT POWER						
HVmin to HVmax	+20 to +90	+20 to +90	+20 to +180	+20 to +180	+20 to +180	Vdc, transformer-isolated
Peak current	10	20	10	20	30	Adc (1 sec)
Continuous current	4.53	9.07	4.53	9.07	13.6	Adc

PWM OUTPUTS		
Type	MOSFET H-bridge , 20 kHz center-weighted PWM carrier	
PWM ripple frequency	40 kHz	
BANDWIDTH		
Current loop, small signal	3 kHz typical, bandwidth will vary with tuning & load inductance	
HV Compensation	HV_{min} to HV_{max}, changes in HV do not affect bandwidth	
Current loop update rate (period)	20 kHz (50 µs)	
Velocity loop update rate (period)	4 kHz (250 µs)	
REFERENCE INPUTS		
Analog torque & velocity reference	±10 Vdc, 12 bit resolution	Differential
Input impedance	66 kΩ	Between Ref(+), Ref(-)
Digital torque & velocity reference (Note 1)	PWM [IN5], Polarity [IN4]	PWM = 0% to 100%, Polarity = 1/0 or PWM = 50% ±50%, no polarity signal required
	PWM frequency range	1 kHz minimum, 100 kHz maximum
	PWM minimum pulse width	220 ns
DIGITAL INPUTS (NOTE 1)		
All inputs	74HCT14 Schmitt trigger operating from +5.0 Vdc with RC filter on input RC filter time-constants assume active drive on inputs and do not include 10 kΩ pull-up (pull-down)	
RC filters	GP inputs: 330 µs, HS inputs: 100 ns	
Pull-up/pull-down	Group-programmable: [IN1,2,3] have pull-ups to +5 Vdc or pull-downs to signal ground Non-programmable: [IN4] and [IN5] have pull-ups to +5 Vdc	
Logic levels	Vin-LO < 0.5 V, Vin-HI >1.9 V, Maximum input voltage = +10 VDC	
Input Polarity	Active level is programmable via CME 2™ software	
Amp Enable [IN1]	1 GP input dedicated to amplifier enable function, active level and reset functions programmable	
GP [IN2,3]	2 GP inputs with programmable functions and active level select	
HS [IN4,5]	2 HS Inputs inputs programmable functions, and active level select	
SERIAL DATA INPUT		
RS-232	RxD, TxD, Gnd in 6-position, 4-contact RJ-11 type modular connector, and on J2 Full-duplex, serial communication port for amplifier setup and control, 9600 to 115200 baud Protocol: binary	
MOTOR CONNECTIONS		
Mot(+), Mot(-)	Amplifier outputs to DC brush motor or voice-coil motor with ungrounded winding	
STATUS INDICATOR		
Amp Status	Bicolor LED. Amplifier status indicated by color and blinking or non-blinking condition	
DIGITAL OUTPUT (NOTE 1)		
Type	Current-sinking MOSFET open-drain output with 1 kΩ pullup to +5 Vdc through diode, 1 Adc sink max, 40Vdc max.	
Functions	Programmable	
Active Level	Programmable to either HI (off, pull-up to +5 Vdc) or LO (on, current-sinking) when output is active	
PROTECTIONS		
HV Overvoltage	+HV > HV_{max}	Amplifier outputs turn off until +HV < HV_{max} (See Input Power for HV_{max})
HV Undervoltage	+HV < +20 Vdc	Amplifier outputs turn off until +HV > +20 Vdc
Amplifier over temperature	PC Board > 70 °C	Amplifier latches OFF until Enable input (Note 1) cycled, power off-on, or Reset
Short circuits		Output to output, output to ground, internal PWM bridge faults
I^2T Current limiting		Programmable: continuous current, peak current, peak time
MECHANICAL & ENVIRONMENTAL		
Size	5.10 in (129,5 mm) X 3.22 in (81,79 mm) X 1.17 in (29,72 mm)	
Weight	0.66 lb (0.30 kg) for amplifier without heatsink	
Ambient temperature	0 to +45 °C operating, -40 to +85 °C storage	
Humidity	0% to 95%, non-condensing	
Contaminants	Pollution degree 2	
Environment	IEC68-2: 1990	
Cooling	Heat sink and/or forced air cooling may be required for continuous power output (see pp. 8 & 9)	

NOTES

1. Functions of [IN2,3,4,5] and [OUT1] are programmable

Figure 79: Amplifier: Copley Controls JSP-090-10

Technical Details

Parameter		Specification		
MicroLabBox		**Front Panel Variant**	**Top Panel Variant with BNC Connectors**	**Top Panel Variant with Spring-Cage Terminal Blocks**
Processor	Real-time processor	■ NXP (Freescale) QorIQ P5020, dual-core, 2 GHz ■ 32 KB L1 data cache per core, 32 KB L1 instruction cache per core, 512 KB L2 cache per core, 2 MB L3 cache total		
	Host communication co-processor	■ NXP (Freescale) QorIQ P1011 800 MHz for communication with host PC		
Memory		■ 1 GB DRAM ■ 128 MB flash memory		
Boot time		■ Autonomous booting of applications from flash (depending on application size), ~5 s for a 5 MB application		
Interfaces	Host interface	■ Integrated Gigabit Ethernet host interface		
	Ethernet real-time I/O interface	■ Integrated low-latency Gigabit Ethernet I/O interface		
	USB interface	■ USB 2.0 interface for data logging ("flight recorder") and booting applications via USB mass storage device (max. 32 GB supported)		
	CAN interface	■ 2 CAN channels (partial networking supported)		
	Serial interface	■ 2 x UART (RS232/422/485) interface		
	LVDS interface	■ 1 x LVDS interface to connect with the Programmable Generic Interface PGI1		
Programmable FPGA[1]		■ Xilinx® Kintex®-7 XC7K325T FPGA		
Analog input	Resolution and type	■ 8 14-bit channels, 10 Msps, differential; functionality: free running mode ■ 24 16-bit channels, 1 Msps, differential; functionality: single conversion and burst conversion mode with different trigger and interrupt options		
	Input voltage range	■ -10 ... 10 V		
Analog output	Resolution and type	■ 16 16-bit channels, 1 Msps, settling time: 1 µs		
	Output voltage range	■ -10 ... 10 V		
	Output current	■ ± 8 mA		
Digital I/O		■ 48 bidirectional channels, 2.5/3.3/5 V (single-ended); functionality: bit I/O, PWM generation and measurement (10 ns resolution), pulse generation and measurement (10 ns resolution), 4 x SPI Master ■ 12 bidirectional channels (RS422/485 type) to connect sensors with differential interfaces		
Electric motor control I/O functionality	Separate interfaces	■ 2 x Resolver interface		
	Functionality on digital I/O channels	■ 6 x Encoder sensor input ■ 2 x Hall sensor input ■ 2 x EnDat interface ■ 2 x SSI interface ■ Synchronous multi-channel PWM ■ Block commutational PWM		
Sensor supply		■ 1 x 12 V, max. 3 W/250 mA (fixed) ■ 1 x 2 ... 20 V, max. 1 W/200 mA (variable)		
Feedback elements		■ Programmable buzzer ■ Programmable status LEDs		
Theft protection		■ Kensington® lock		
Cooling		■ Active cooling (temperature-controlled fan)		
Physical connections		■ 4 x Sub-D 50 I/O connectors ■ 4 x Sub-D 9 I/O connectors	■ 2 x Sub-D 50 I/O connectors ■ 48 x BNC I/O connectors ■ 4 x Sub-D 9 I/O connectors	■ 2 x Sub-D 9 I/O connectors ■ 27 x spring-cage terminal block connectors with 8 pins each
		■ 3 x RJ45 for Ethernet (host and I/O) ■ USB Type A (for data logging) ■ 2 x 2 banana connectors for sensor supply ■ Power supply		

[1] *User-programmable via RTI FPGA Programming Blockset. Using the RTI FPGA Programming Blockset requires additional software.*

Figure 80: Controller: dSpace MicroLabBox

SPECIFICATION AND NUMBERING SYSTEM

Part Numbering System Guide

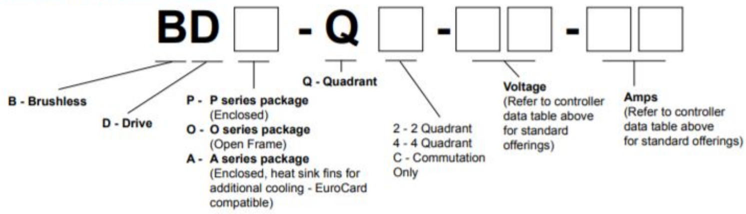

Electrical Data	BDO-Q2-20-18	BDO-Q2-50-18	BDO-Q2-50-40
Operating voltage -+input and Gnd Residual voltage < 5 %	12-28 VDC **Obseleted**	20-50 VDC	20-50 VDC
Maximum constant current (adjustable)	18 A	18 A	40 A
Mechanical Data	**BDO-Q2-20-18**	**BDO-Q2-50-18**	**BDO-Q2-50-40**
Weight	12.91 oz / 366 gm	12.91 oz / 366 gm	13.76 oz / 390 gm
Dimensions - (L x W x H) - 6.69 x 3.54 x 1.73 in (170 x 90 x 44 mm)			
Mounting - 4 x M4 with a distance between holes of 6.30 x 2.52 in (160 x 64 mm)			
Diameter - 4.5 mm - (4) places - M4 screw			

Inputs
- Direction of rotation – (REV) open collector / TTL / CMOS / switch
- Disable output stage – (DIS) open collector / TTL / CMOS / switch

Moisture Range
20 to 80% non-condensed

Temperature Range
Storage -40 to +85°C
Operation -10 to +45°C

Termination Table

Signal			Power		
Terminal #	*Nomenclature*	*Description*	*Terminal #*	*Nomenclature*	*Description*
1	S1	Hall Switch #1	1	Positive Input	Positive Supply Voltage
2	S2	Hall Switch #2	2	Phase B	Motor Phase B
3	S3	Hall Switch #3	3	Phase C	Motor Phase C
4	VCC	Supply for Hall Switches	4	Phase A	Motor Phase A
5	Gnd	Gnd for Hall Switches	5	Gnd	Gnd for Supply Voltage
6	DIS	Control Input - Disable			
7	REV	Control Input - Reverse			
8	GND	Gnd for Dis and Rev			
9	SPD	Set value input for speed			

Drive Electronics

Figure 81: Motor Controller: MOOG Silencer Series

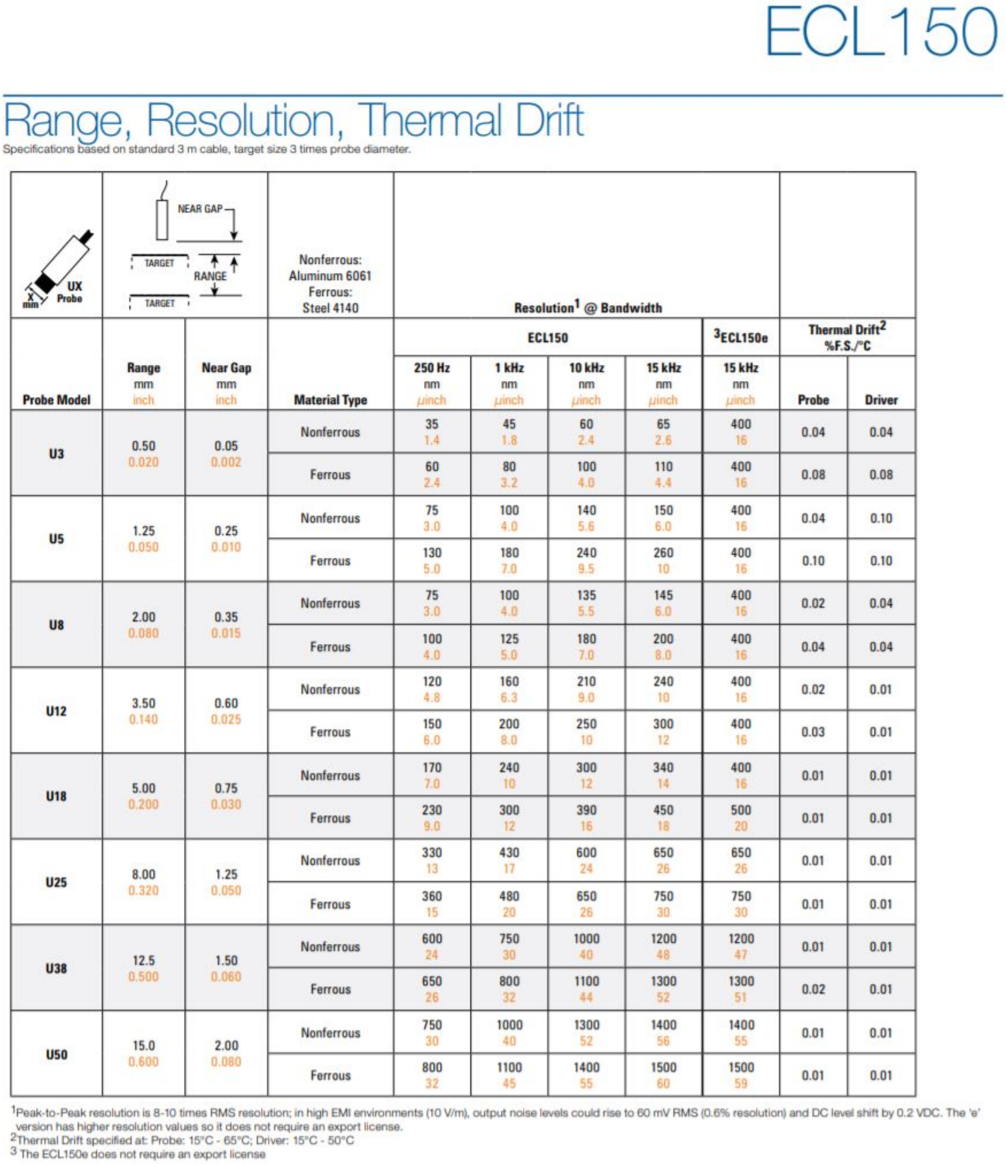

ECL150

Range, Resolution, Thermal Drift

Specifications based on standard 3 m cable, target size 3 times probe diameter.

Nonferrous: Aluminum 6061
Ferrous: Steel 4140

				Resolution[1] @ Bandwidth						
				ECL150				[3]ECL150e	Thermal Drift[2] %F.S./°C	
Probe Model	Range mm inch	Near Gap mm inch	Material Type	250 Hz nm µinch	1 kHz nm µinch	10 kHz nm µinch	15 kHz nm µinch	15 kHz nm µinch	Probe	Driver
U3	0.50 0.020	0.05 0.002	Nonferrous	35 1.4	45 1.8	60 2.4	65 2.6	400 16	0.04	0.04
			Ferrous	60 2.4	80 3.2	100 4.0	110 4.4	400 16	0.08	0.08
U5	1.25 0.050	0.25 0.010	Nonferrous	75 3.0	100 4.0	140 5.6	150 6.0	400 16	0.04	0.10
			Ferrous	130 5.0	180 7.0	240 9.5	260 10	400 16	0.10	0.10
U8	2.00 0.080	0.35 0.015	Nonferrous	75 3.0	100 4.0	135 5.5	145 6.0	400 16	0.02	0.04
			Ferrous	100 4.0	125 5.0	180 7.0	200 8.0	400 16	0.04	0.04
U12	3.50 0.140	0.60 0.025	Nonferrous	120 4.8	160 6.3	210 9.0	240 10	400 16	0.02	0.01
			Ferrous	150 6.0	200 8.0	250 10	300 12	400 16	0.03	0.01
U18	5.00 0.200	0.75 0.030	Nonferrous	170 7.0	240 10	300 12	340 14	400 16	0.01	0.01
			Ferrous	230 9.0	300 12	390 16	450 18	500 20	0.01	0.01
U25	8.00 0.320	1.25 0.050	Nonferrous	330 13	430 17	600 24	650 26	650 26	0.01	0.01
			Ferrous	360 15	480 20	650 26	750 30	750 30	0.01	0.01
U38	12.5 0.500	1.50 0.060	Nonferrous	600 24	750 30	1000 40	1200 48	1200 47	0.01	0.01
			Ferrous	650 26	800 32	1100 44	1300 52	1300 51	0.02	0.01
U50	15.0 0.600	2.00 0.080	Nonferrous	750 30	1000 40	1300 52	1400 56	1400 55	0.01	0.01
			Ferrous	800 32	1100 45	1400 55	1500 60	1500 59	0.01	0.01

[1]Peak-to-Peak resolution is 8-10 times RMS resolution; in high EMI environments (10 V/m), output noise levels could rise to 60 mV RMS (0.6% resolution) and DC level shift by 0.2 VDC. The 'e' version has higher resolution values so it does not require an export license.
[2]Thermal Drift specified at: Probe: 15°C - 65°C; Driver: 15°C - 50°C
[3] The ECL150e does not require an export license

Figure 82: Displacement Sensor: Lion Precision U5

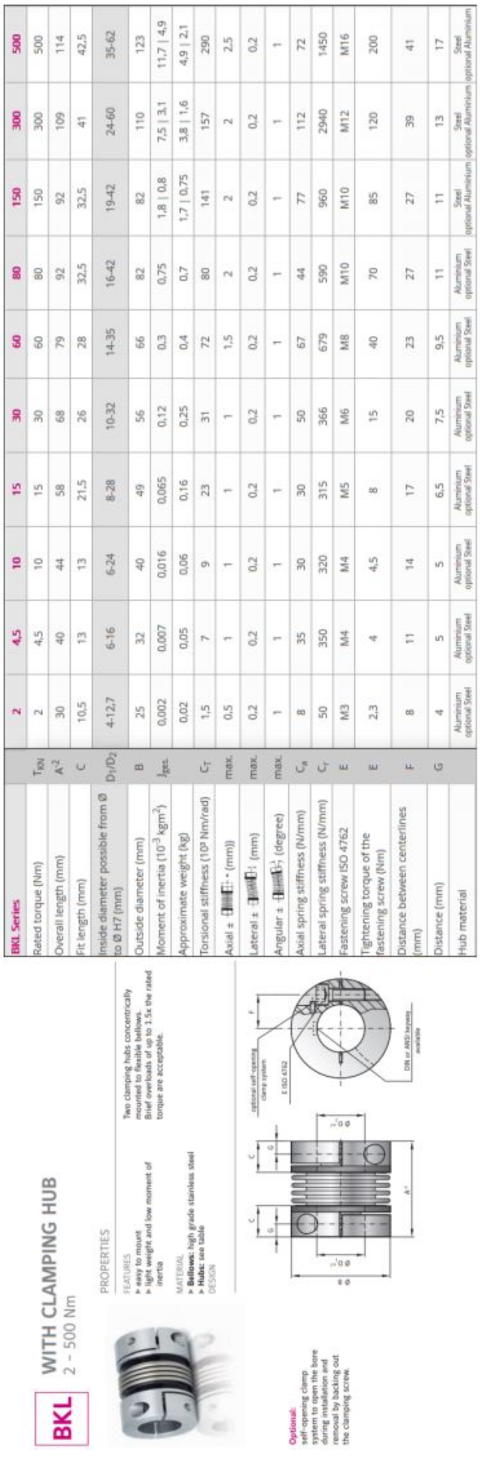

BKL WITH CLAMPING HUB
2 - 500 Nm

PROPERTIES

FEATURES
> easy to mount
> light weight and low moment of inertia

MATERIAL
> Bellows: high grade stainless steel
> Hubs: see table

DESIGN
Two clamping hubs concentrically mounted to flexible bellows. Brief overloads of up to 1.5x the rated torque are acceptable.

Optional: self-opening clamp system to open the bore during installation and removal by backing out the clamping screw.

BKL Series		2	4,5	10	15	30	60	80	150	300	500
Rated torque (Nm)	T_{KN}	2	4,5	10	15	30	60	80	150	300	500
Overall length (mm)	A^{-2}	30	40	44	58	68	79	92	92	109	114
Fit length (mm)	C	10,5	13	13	21,5	26	28	32,5	32,5	41	42,5
Inside diameter possible from Ø to Ø H7 (mm)	D_1/D_2	4-12,7	6-16	6-24	8-28	10-32	14-35	16-42	19-42	24-60	35-62
Outside diameter (mm)	B	25	32	40	49	56	66	82	82	110	123
Moment of inertia (10^{-3} kgm^2)	$J_{ges.}$	0,002	0,007	0,016	0,065	0,12	0,3	0,75	1,8 | 0,8	7,5 | 3,1	11,7 | 4,9
Approximate weight (kg)		0,02	0,05	0,06	0,16	0,25	0,4	0,7	1,7 | 0,75	3,8 | 1,6	4,9 | 2,1
Torsional stiffness (10^3 Nm/rad)	C_T	1,5	7	9	23	31	72	80	141	157	290
Axial ± (mm)	max.	0,5	1	1	1	1	1,5	2	2	2	2,5
Lateral ± (mm)	max.	0,2	0,2	0,2	0,2	0,2	0,2	0,2	0,2	0,2	0,2
Angular ± (degree)	max.	1	1	1	1	1	1	1	1	1	1
Axial spring stiffness (N/mm)	C_a	8	35	30	30	50	67	44	77	112	72
Lateral spring stiffness (N/mm)	C_r	50	350	320	315	366	679	590	960	2940	1450
Fastening screw ISO 4762	E	M3	M4	M4	M5	M6	M8	M10	M10	M12	M16
Tightening torque of the fastening screw (Nm)	E	2,3	4	4,5	8	15	40	70	85	120	200
Distance between centerlines (mm)	F	8	11	14	17	20	23	27	27	39	41
Distance (mm)	G	4	5	5	6,5	7,5	9,5	11	11	13	17
Hub material		Aluminium optional Steel	Aluminium optional Steel	Aluminium optional Steel	Aluminium optional Steel	Aluminium optional Steel	Aluminium optional Steel	Aluminium optional Steel	Steel optional Aluminium	Steel optional Aluminium	Steel optional Aluminium

Figure 83: Coupling, R+W BKL-10

F Mechanical Assembly Details

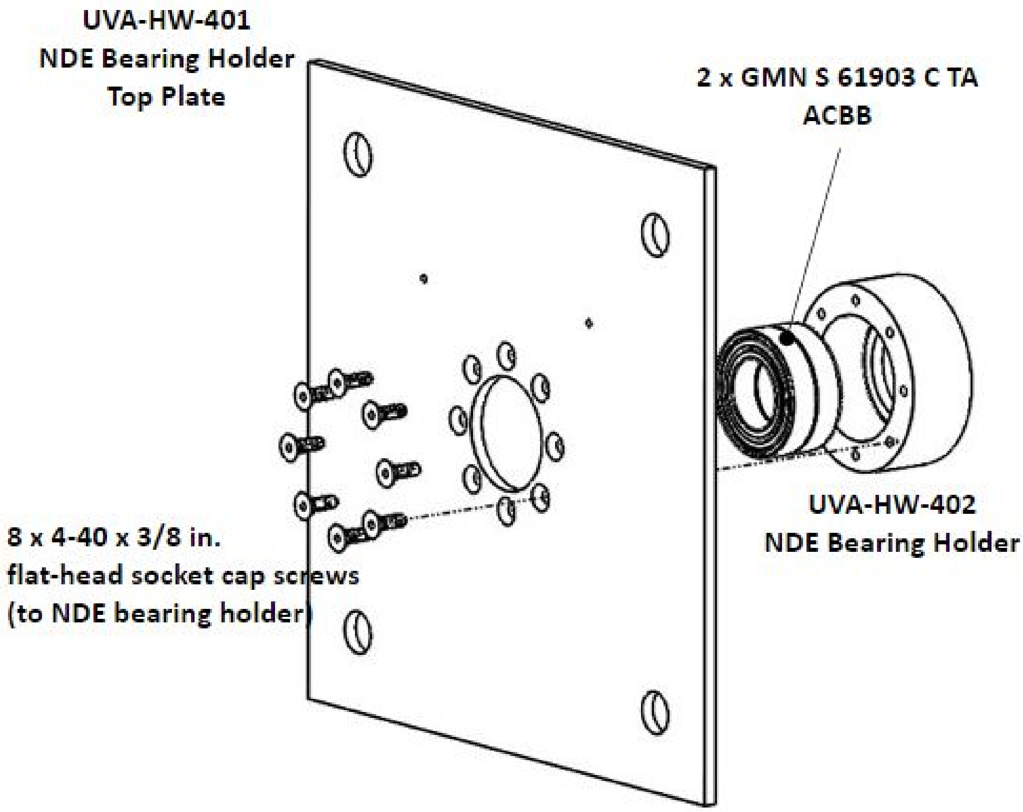

Figure 84: NDE Backup Bearing Assembly

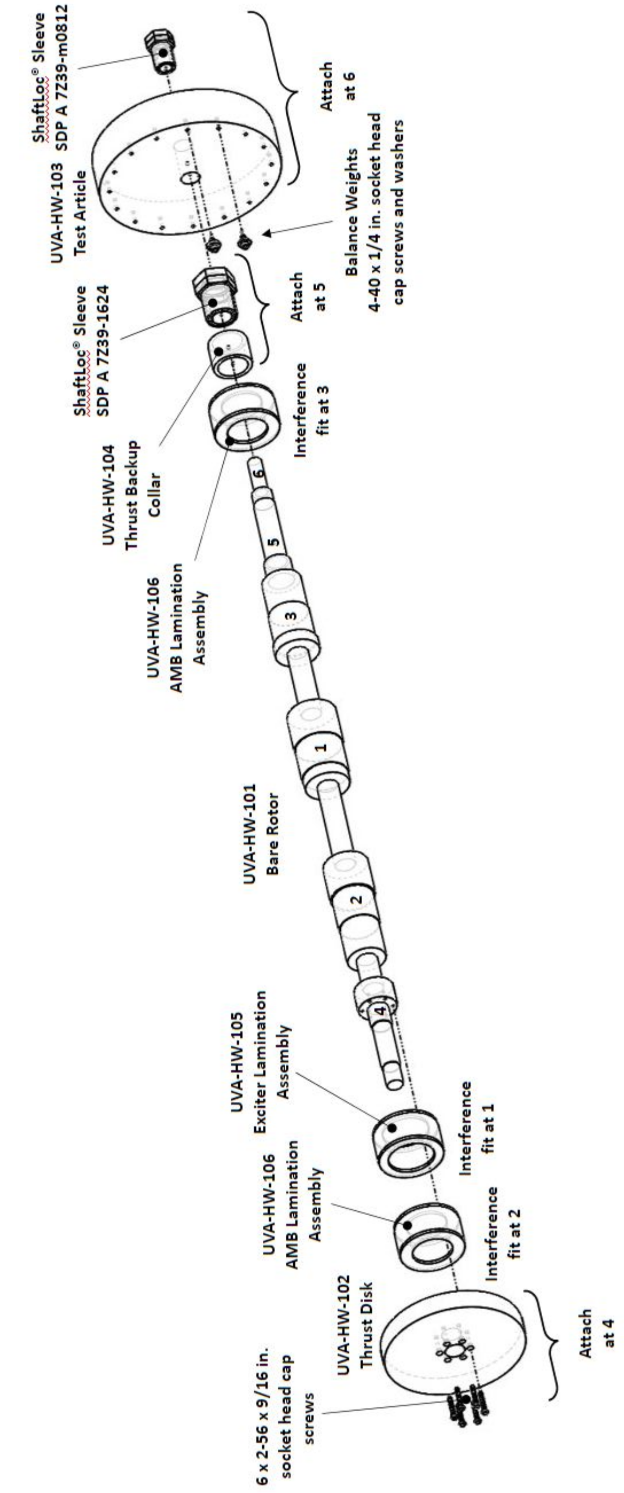

Figure 85: Assembly Drawing, Rotor

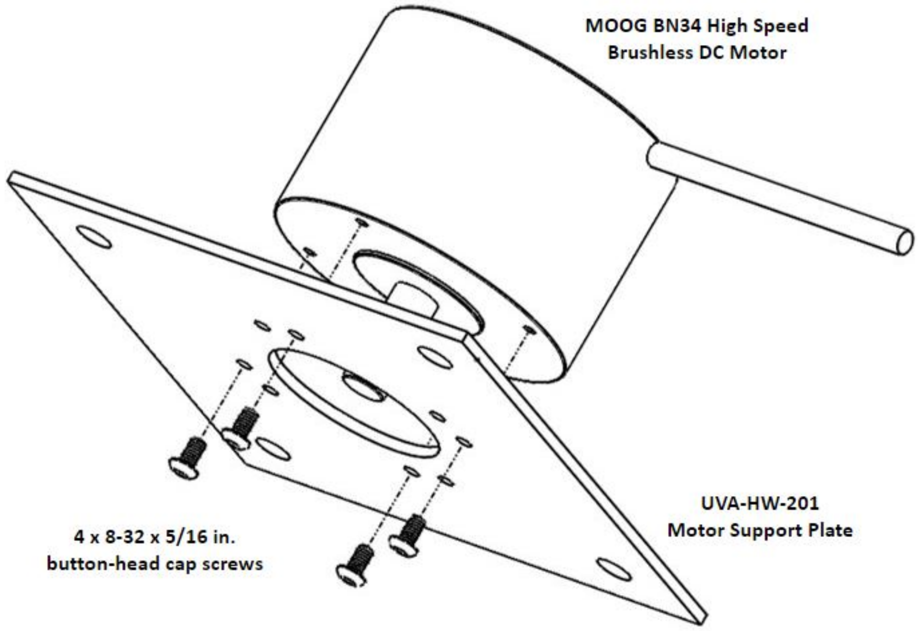

Figure 86: Assembly Drawing, Motor

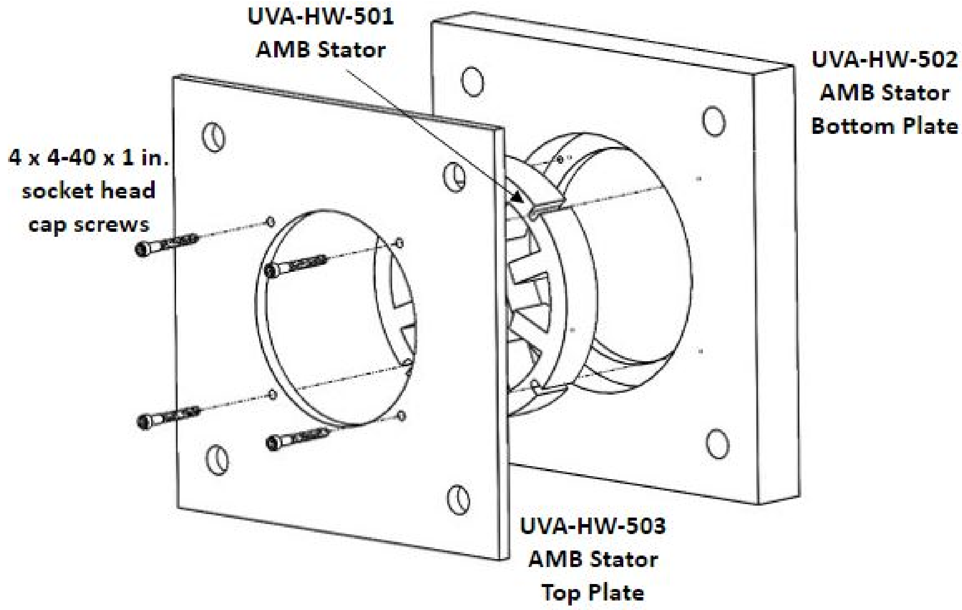

Figure 87: Radial AMB / Exciter Assembly

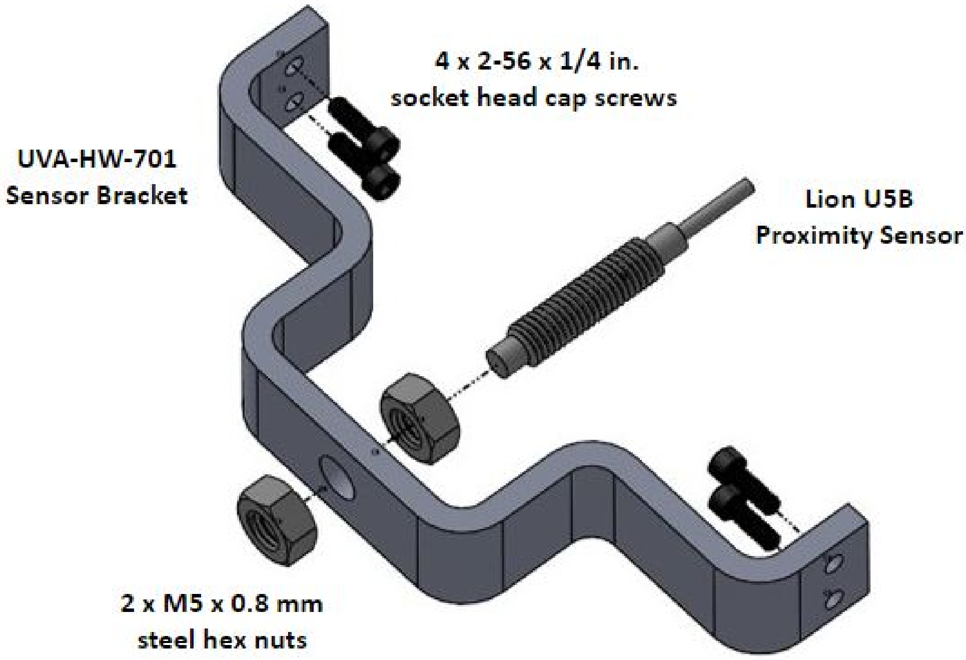

Figure 88: Sensor Assembly

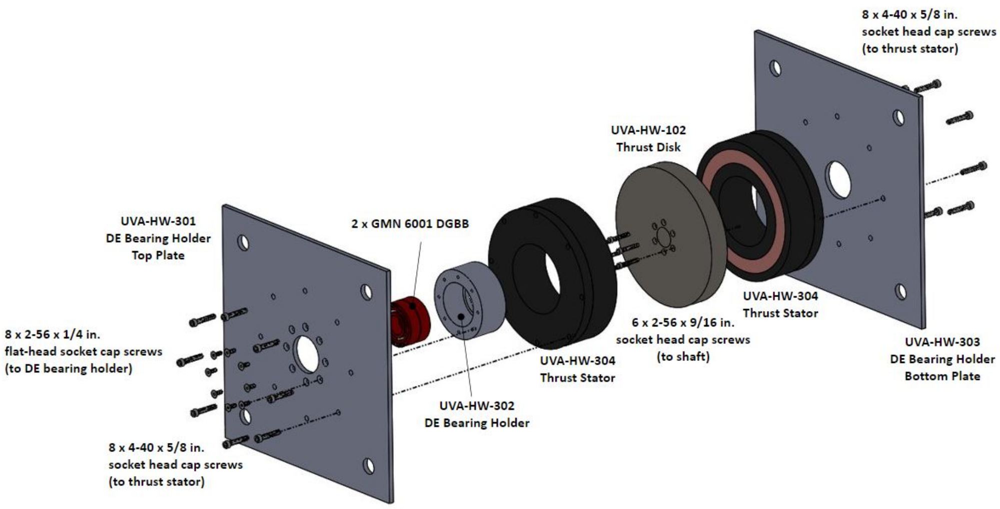

Figure 89: Thrust AMB / DE Backup Bearing Assembly

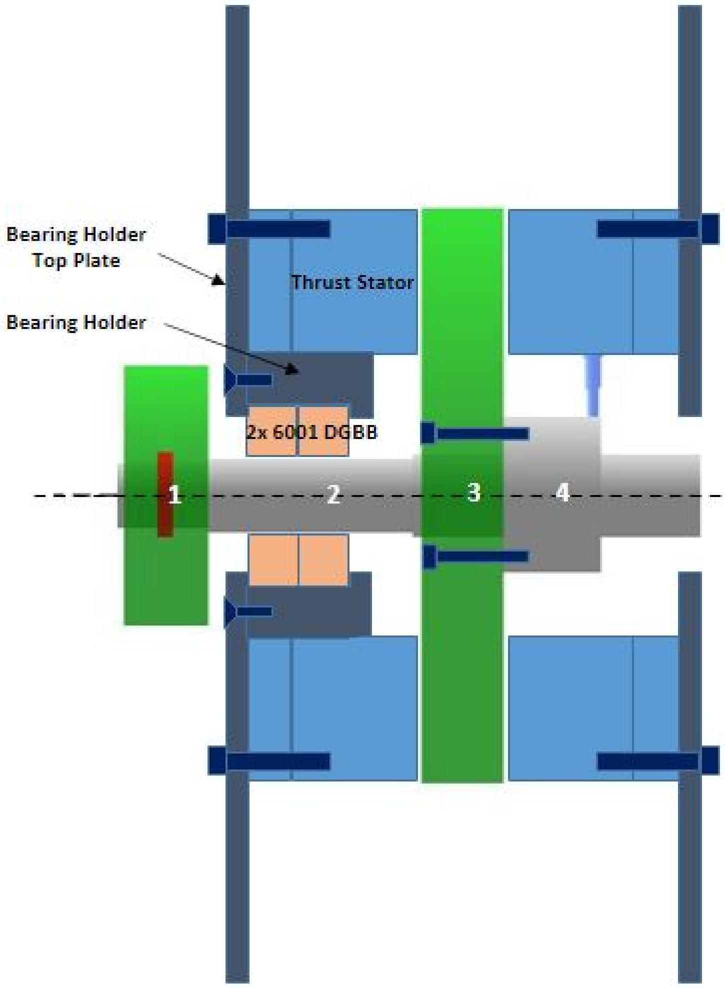

Figure 90: DE Backup Bearings: Double Row Deep Groove Ball Bearings (2x 6001)

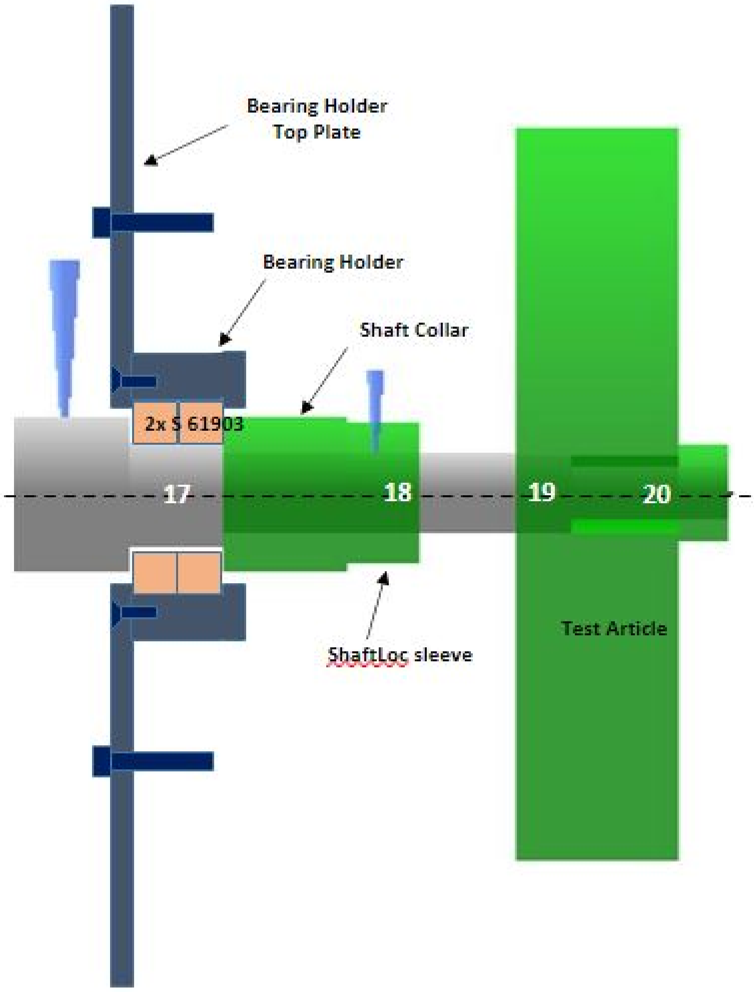

Figure 91: NDE Backup Bearings: Double Row Angular Contact Ball Bearings, Face-to-Face Arrangement, (2 x S 61903 C TA)